國 立 交 通 大 學

電機與控制工程研究所

碩士論文

靜電式微功率轉換器之最佳化設計與改良

Optimal Design and Improvement of an Electrostatic Micropower Converter

研究生 ：陳弘諳

指導教授：邱一 博士

中華民國九十七年十二月

靜電式微功率轉換器之最佳化設計與改良

Optimal Design and Improvement of an Electrostatic Micropower Converter

研　究　生:陳弘諳　　　　Student：Hung An Chen

指導教授:邱一　　　　Advisor：Yi Chiu

國立交通大學 電機學院

電機與控制工程研究所

碩士論文

A Thesis
Submitted to Department of Electrical and Control Engineering
College of Electrical Engineering
National Chiao Tung University
In Partial Fulfillment of the Requirement
For the Degree of
Master of Science
In

Electrical and Control Engineering

December 2008

Hsinchu, Taiwan, R.O.C.

中華民國九十七年十二月

中文摘要

近年來微機電系統科技已成為世界各國於半導體產業之後相繼追求的新興整合型科技產業。目前各種微機電系統的發展均以和 IC 整合為最終目標。在此技術層面應用上，每一個節點的模組也都可能有獨立電源的需求。拜先進的低功率超大型積體電路與 CMOS 技術，元件的電能需求已降至數十 μW 的等級。因此，利用微機電技術將環境中的能源轉換成電能已成為一種可行的方式。

本論文將有別於前幾代的元件結構，針對無外加質量球的元件來做最佳化功率的設計，利用理論模型及分析找出最佳的參數來得到元件可輸出的最大功率。在 1 cm^2 元件面積及 120 Hz 操作頻率的限制下，元件輸出功率為 0.51 μW (功率密度為 12 $\mu W/cm^3$)，輸出電壓約 5V，元件質量約 36.5 mg。在製程方面，元件製作將針對上一代的漏電電阻問題進行改善，利用 SOI 晶圓並搭配深蝕刻的製程，定義出梳指狀電極以形成電容，再經由外加振動源驅動來產生可變電容的改變，以達到電能轉換的功效。透過低壓化學絕緣層的沉積以及精確的遮罩定義金屬電極，使結構有良好的絕緣性以達到隔絕短路的效果。元件的共振頻率經由微機電動態干涉儀及激振器的測試皆符合設計值。經由電容放電時間常數的量測也顯示寄生電阻的改善。元件在 3.33 MΩ負載及 182 Hz 振動頻率下，量到的交流輸出功率為 17.5 nW，功率輸出的頻率問題已完成討論。此外，元件上機械式開關經由靜態和動態的量測也已完成測試。

Abstract

In recent years, Micro-Electro-Mechanical System (MEMS) technology has become an emerging and integrated industry which every company in the world have been following after the IC industry. The goal of MEMS is the integration with circuits. Each node of module may have an independent power demand. Advances in low power VLSI and CMOS technology have reduced the power consumption of electronic devices to a few tens of microwatts. Therefore, it is feasible to scavenge and transform energy in the environment into electric energy.

The optimal power design without external mass attachment which differs from the previous device was presented in this thesis. The optimal parameter was obtained by using theoretical model and analysis in order to get maximum output power. With a device area constraint of $1cm^2$ and operation frequency of 120 Hz, the output power was 0.51 μW (power density of 12 $\mu W/cm^3$), output voltage was 5 V, and the mass of device was about 36.5 mg. The leakage resistance of the previous device was improved. The device was fabricated in SOI wafer by deep silicon etching technology. The comb finger structure was defined to form a capacitance. The capacitance variation was caused by the external vibration source in order to convert the electrical energy. By depositing LPCVD isolation layer and defining electrical pad with an accurate shadow mask, the device has better isolation and the leakage problem removal. The resonant frequencies measured by MMA and shaker agreed with the design value. Parasitic resistance improvement was verified by the discharge time constant measurement. The measured AC output power was 17.5 nW with a load of 3.33 MΩ and frequencies of 182 Hz. The issue of the frequency of AC power was discussed. Finally, the mechanical switch on the device was tested.

致謝

歲月不饒人, 兩年多的碩士生涯即將邁入尾聲, 也代表學生時代即將結束。首先，我要感謝我的指導教授邱一老師, 老師的專業程度讓我這初生之犢開了眼界，也在這兩年當中學到不少東西，尤其是研究的邏輯和態度。老師除了研究給予指導和意見外，也會隨時關心學生的狀況，而最後的英文論文寫作更是我最大的罩門，儘管老師身邊有很多自己的事情要忙，卻不厭其煩的看著我那破爛的英文文法做出校正和修改，也充分了解到英文寫作的重要性，很感謝老師的付出和關心。

感謝我的口試委員:盧向成教授、洪浩喬教授及黃聖傑教授，老師們在繁忙之餘也對我的論文提供寶貴的建議和支援，謝謝你們。

感謝我的學長曾繁果，若沒有你的經驗傳承，我也無法順利繼續研究。還有博士班學長黃信瑀和洪振均，你們在微機電的製程上也提供了很多經驗和方法，也感謝你們不厭其煩的解說。還有這兩年來實驗室的夥伴子麟，在最後關頭能一起互相打拼，給了我精神上的支柱，還有其他夥伴昌修和昇儒，這兩年來有你們一路相隨也讓我在研究路上不會覺得孤單，也祝你們鵬程萬里，心想事成。還有邱俊誠實驗室的夥伴，我也要感謝你們，讓我研究生涯中多了精彩。實驗室碩二的學弟經富和健安，祝你們在往後一年的時間研究一帆風順，順利畢業。還有讓實驗室充滿朝氣的可愛碩一學弟妹，姿穎、鴻智、俊鴻、政安、哲明，看到你們之間的感情深厚我很欣慰，也祝福你們往後研究之路更順利。

最後要感謝的還是我的父母，你們總是這麼信任我支持我，在我研究繁忙之餘提供我學費和生活費，讓我無後顧之憂，我才能順利完成碩士學業。你們的養育之恩，我實在無從報答，未來的我必不會讓你們失望的。最後謝謝培育我的交通大學，珍重再見。

Table of Content

中文摘要..........i
Abstract..........ii
致謝..........iii
Table of Content..........iv
List of Figures..........vi
List of Tables..........ix
Chapter 1 Introduction..........1
1.1 Literature review..........2
1.1.1 Light exposure..........2
1.1.2 Thermoelectric effect..........3
1.1.3 Human body movement..........4
1.1.4 Acoustic noise..........6
1.1.5 Wind..........6
1.1.6 Ambient Vibration..........7
1.1.7 Summary of power sources..........7
1.2 Ambient vibration energy conversion..........8
1.2.1 Piezoelectric energy conversion..........8
1.2.2 Electromagnetic energy conversion..........9
1.2.3 Electrostatic energy conversion..........11
1.2.4 Comparison of energy conversion technologies..........13
1.2.5 Our previous work..........13
1.3 Thesis objectives and organization..........13
Chapter 2 Principle and Design..........15
2.1 Characteristics of vibration sources..........15
2.2 Operational principle..........17
2.3 Device design..........20
2.3.1 Auxiliary power supply..........21
2.3.2 Static analysis..........21
2.3.3 Dynamic analysis..........22
2.3.4 Variable capacitor design..........26
2.3.5 Spring design..........32
2.3.6 Mechanical switch control analysis..........36
2.4 Layout design..........39
2.5 Previous design and improvement..........41
2.6 Summary..........44

Chapter 3 Fabrication Process 45
3.1 Fabrication process flow 45
3.2 Processing issues and solution 56
3.2.1 Non ideal effects of the ICP process 56
3.2.2 Silicon nitride deposition 61
3.2.3 Metal deposition issues 63
3.3 Fabricated device 64
3.4 Summary 67
Chapter 4 Measurement and Results 68
4.1 Mechanical measurement..68
4.1.1 MEMS Motion Analyzer measurement 68
4.1.2 Vibration measurement by our shaker 71
4.2 Static electrical measurement..73
4.2.1 Measurement for PECVD nitride deposition..74
4.2.2 Measurement for LPCVD nitride deposition..78
4.3 Dynamic electrical measurement..80
4.3.1 AC mode power measurement..80
4.3.2 DC mode power measurement..84
4.4 Summary 87
Chapter 5 Summary and Future work 88
5.1 Summary 88
5.2 Future work..89
References..91

List of Figures

Fig. 1.1 Photovoltaic energy conversion..3
Fig. 1.2 Thermoelectric energy converter...4
Fig. 1.3 Shoe generation system 5
Fig. 1.4 (a) Photo of the windmill, (b) close-up of the simple generator.......................7
Fig. 1.5 A two-layer cantilever beam piezoelectric energy converter............................9
Fig. 1.6 Electromagnetic energy converter 10
Fig. 1.7 Schematic of an electromagnetic generator system..11
Fig. 1.8 (a) Gap-closing and (b) overlap in-plane variable capacitors.........................11
Fig. 2.1 Vibration spectra by Roundy 16
Fig. 2.2 Measurement of dehumidifier vibration 16
Fig. 2.3 Vibration spectrum of a dehumidifier...17
Fig. 2.4 Operation circuit of the electrostatic energy converter...................................17
Fig. 2.5 Variable capacitor schematic 18
Fig. 2.6 Capacitor charging and capacitance change by vibration...............................18
Fig. 2.7 Charge transfer and discharge process 19
Fig. 2.8 Schematic of the conversion dynamic model 22
Fig. 2.9 Electrostatic spring constant in the steady state 24
Fig. 2.10 k/be_max versus the desired maximum displacement 26
Fig. 2.11(a) Top view of the in-plane gap closing variable capacitor, (b) fingers with silicon nitride coating, (c) equivalent capacitance model between fingers .26
Fig. 2.12 A general model of the movable plate 28
Fig. 2.13 b_{e_max} constraint for (a) three-dimension (b) two-dimension diagram..........30
Fig. 2.14 Output power versus desired maximum displacement and finger overlap length...31
Fig. 2.15 A single element of spring structure 33
Fig. 2.16 (a) A single spring element (b) single spring constant simulated by CoventorWare 35
Fig. 2.17 (a) Device solid model (b) CoventorWare modal analysis...........................36
Fig. 2.18 SW2 closes (a) on time (b) early (c) late 38
Fig. 2.19 Output power loss versus timing error 39
Fig. 2.20 Layout view of the variable capacitor and switches.....................................40
Fig. 2.21 Layout view of the previous device..41
Fig. 2.22 (a) Front side SW1 layout view in our previous design (b) modified design 43
Fig. 2.23 (a) Overlap region between fingers and substrate (b) overlap region removal

....43
Fig. 3.1 Fabrication process flow of the SOI device...53
Fig. 3.2 Notching effect 57
Fig. 3.3 (a) Notching occurred on the fingers bottom side, (b) improvement result ...58
Fig. 3.4 SEM photo with different C_4F_8 flow time (a) SF_6: C_4F_8 = 11s:10s (b) SF_6: C_4F_8 = 11s:7s 59
Fig. 3.5 (a) Polymer produced in the ICP etching (b) polymer removal by NH3 solution...60
Fig. 3.6 Experiment results in the plasma permeate on the front side 61
Fig. 3.7 Schematic of poor step coverage...62
Fig. 3.8 Aluminum deposition by shadow mask...63
Fig. 3.9 Center hole of the fabricated device 64
Fig. 3.10 (a) Corner of device with aluminum deposition (b) Close up view of the serpentine spring 65
Fig. 3.11 Close-up view of finger (a) width (b) perpendicularity...............................65
Fig. 3.12 Device with silicon nitride coating..66
Fig. 3.13 Device with the external mass on the PCB board 66
Fig. 4.1 (a) MMA system (b) Close view of the device on the mini-shaker (c) vibration amplitude of mini-shaker...69
Fig. 4.2 MMA experiment results with metal ball (a) amplitude response (b) phase response...70
Fig. 4.3 (a) Measurement schematic (b) our mechanical measurement setup 72
Fig. 4.4 (a) Static device (b) device operates at resonant frequency of 116 Hz (c) resonance acceleration waveform. 73
Fig. 4.5 Leakage resistance measurement circuit 74
Fig. 4.6 Variable capacitor measurement circuit...75
Fig. 4.7 RC discharge time constant measurement for PECVD deposition (a) Zero displacement, time constant τ=95 μs (b) maximum displacement of 25 μm, time constant τ=287 μs...76
Fig. 4.8 Measured variable capacitor versus displacement...76
Fig. 4.9 Cross-section of non-parallel capacitor 77
Fig. 4.10 C_{actual}/C_{ideal} versus oblique angle 78
Fig. 4.11 SEM photo (a) Close up of non-parallel capacitance (b) unflat surface of finger sidewall...78
Fig. 4.12 RC discharge time constant measurement for LPCVD deposition (a) zero displacement, time constant τ = 1.13 ms (b) maximum displacement of 25 μm, time constant τ = 4.36 ms 79
Fig. 4.13 Discharge time constant for PECVD and LPCVD nitride deposition..........80

Fig. 4.14 AC mode power measurement circuit 81
Fig. 4.15 AC power measurement with mass attached for various load resistances (a) 2.5 MΩ (b) 3.33 MΩ (c) 10 MΩ 82
Fig. 4.16 AC power measurement with various load resistance 83
Fig. 4.17 Simulation results for AC model circuit 84
Fig. 4.18 Schematic of parasitic variable capacitor C_b generation 84
Fig. 4.19 DC model with mechanical switches 85
Fig. 4.20 Mechanical switch SW1 is (a) turning off (b) turning on 85
Fig. 4.21 Charge Voltage 85
Fig. 4.22 Voltage on the variable capacitor 86
Fig. 4.23 Simulation results for the circuit from Fig. 4.19 87

List of Tables

Table 1.1 Comparison of power sources 8
Table 1.2 Three type of energy converter comparison 13
Table 2.1 Variable capacitor design parameters 32
Table 2.2 Spring design parameters 35
Table 2.3 Design parameter for previous device 42
Table 3.1 The thin film property of LPCVD and PECVD nitride 63

Chapter 1 Introduction

Micro-Electro-Mechanical System (MEMS) is a technology which combines optical, mechanical, electronic, control, physical, chemical, and biomedical subsystems on a common substrate through micro fabrication processes. Application of the technology can improve the quality, performance, and reliability of the system. It can also reduce the cost due to miniaturization. MEMS have made possible the realization of the concept of system on chip (SOC). Current microsystem technology has been applied in fields such as sensors and actuators, micro optical systems, biomedical systems, aerospace and defense systems, and even entertainment applications.

Due to the advance of microsystem technology and the needs from consumers, highly integrated portable devices have received increasing interests in recent years. However, power consumption is a major problem on the development due to the limited energy capacity of the small storage devices [1]. Traditionally, energy is stored in storage devices such as batteries [2], micro-batteries [3], micro-fuel cells [4], ultra capacitors [5], micro heat engine [6], and radioactive materials [7]. High efficiency and low power loss are necessary to lengthen the life of the portable devices. Researchers have attempted to increase the energy density in these storage devices, but the solutions still have finite lifetime and high maintenance cost.

Low power CMOS VLSI (Very Large Scale Integrated circuit) technology and low duty cycles have enabled the development of such applications as wireless sensor networks or personal health monitoring. These devices have reduced power requirements in the range of tens to hundreds of microwatts [8]. It becomes possible to power these sensor nodes by scavenging ambient energy from the environment.

One can design a self-sustainable or self-renewable energy device that can replenish part or all of the consumed energy by utilizing and scavenging the energy from the environment.

1.1 Literature review

Many state-of-art technologies can scavenge or harvest energy from the environment, such as light exposure, thermal gradients, human power, air flow, acoustic noise, and vibration [9]. Energy harvesting is to convert ambient energy into electrical energy. The environment has an inexhaustible energy supply compared with the common storage devices like batteries and fuel cells. Various approaches to extract energy from the environment to drive low power electronics are studied and compared in this chapter. As a result, the performance of the energy devices is characterized by their power density, instead of energy density used for traditional storage devices.

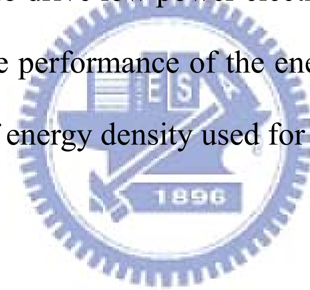

1.1.1 Light exposure

A popular and mature method to scavenge energy is light exposure. Solar cells or photovoltaic cells are the leading technology to convert solar radiation directly to electricity with high conversion efficiency. It can provide power at low operating cost, and is virtually free of pollution. Photovoltaic cells function by the photovoltaic effect [10], the generation of voltage when a device is exposed to light. The photons of the incident solar radiation excite the electrons in the semiconductor, thus allowing the electrons to move freely and the electric current to run through the load. The operation schematic is shown in Fig. 1.1. The device has efficiencies ranging from 12% to 25% for single crystal silicon. The thin film polysilicon and amorphous silicon cost less than single crystal silicon cells but have lower efficiency [11]. Overall, photovoltaic

energy conversion offers sufficient output power besides being a mature IC-compatible technology. Nevertheless, the output power of photovoltaic devices depends heavily on the environmental conditions. For instance, the photovoltaic cells offer adequate power density up to 15 mW/cm^2 if the device is outdoors and operated primarily during daytime. However, in normal indoor office lighting, the same photovoltaic cell will only produce about 10 μW/cm^2. Because of this characteristic, photovoltaic cells are restricted to specific applications.

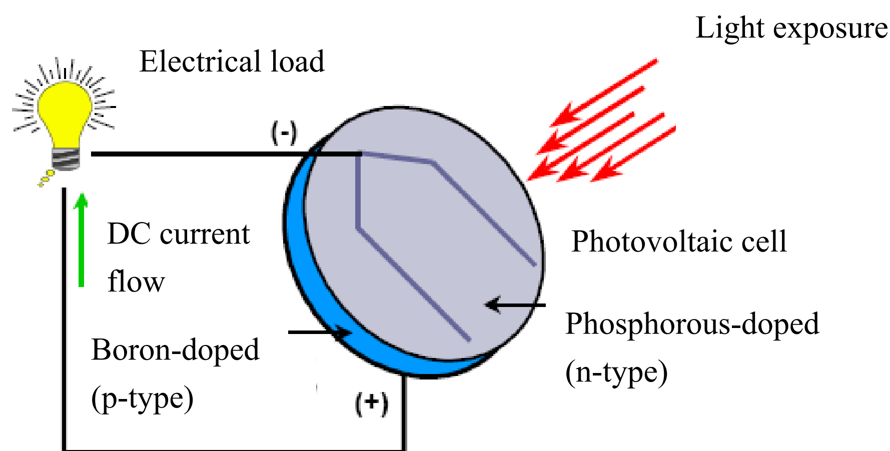

Fig. 1.1 Photovoltaic energy conversion [10]

1.1.2 Thermoelectric effect

Temperature variations can serve as a power source. This phenomenon is called the Seebeck effect, or the thermoelectric effect [12]. When two differential metals are connected in a closed loop, temperature variation in the loop causes the electron movement and a potential is built up between the two metals or semiconductors junctions.

The developed voltage is proportional to the temperature different between the hot and cold ends, and to the Seebeck coefficients of the two materials. Large Seebeck coefficients and high electrical conductivity can improve conversion efficiency and minimize power losses. Materials typically used for thermoelectric energy conversion

include such as Sb_2Te_3, Bi_2Te_3, Bi-Sb, PbTe, Si-Ge, polysilicon, BiSbTeSe compounds, and InSbTe, which are not completely compatible to the IC process. In [13], different annealing conditions have strong influence on the electrical resistivity of Bi-Sb and consequently the thermoelectric generator performances. An output power density of 140 μW/cm^3 for a 100 °C temperature gradient is obtained but the temperature difference of this level is not common in a micro system [14]. So the output power is limited without large thermal gradients. The thermocouple element is used to produce larger output voltage, as shown in Fig. 1.2. Thus, connecting several thermocouple elements in a series configuration can be beneficial. However, large series resistance increases ohmic power loss and thus reduce the overall power conversion efficiency.

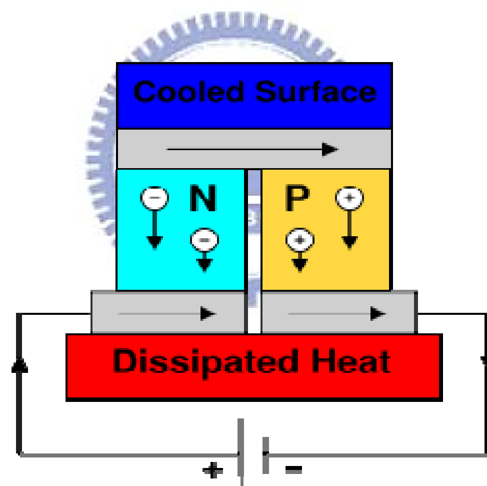

Fig. 1.2 Thermoelectric energy converter [12]

1.1.3 Human body movement

Electronic productions like PDAs or notebook are often limited by the battery capacity and necessity for recharging. Therefore, it is feasible to alleviate these problems by harvesting energy from the human movement. In recent years, needs of wearable electronic devices [15, 16] have grown significantly. Electric energy has been extracted by scavenging waste power from human activities, such as breathing,

body heat, arm motion, and walking. More attention is given to walking since this process seems a more practical source of power for the wearable electronic device. For example, a small women's shoe has a footprint of approximately 116 cm^2, as shown in Fig. 1.3. The shoe contains a piezoelectric shoe insert and the deformation of the piezoelectric pile generates power when walking. In addition, the motion of heels might be converted to electrical energy through traditional generator like spring. The energy stored in this compressed spring can be returned later in the gait to the user. Consequently, a maximum electrical power of 8.4 W could be generated by a 52 kg user at a brisk walking pace.

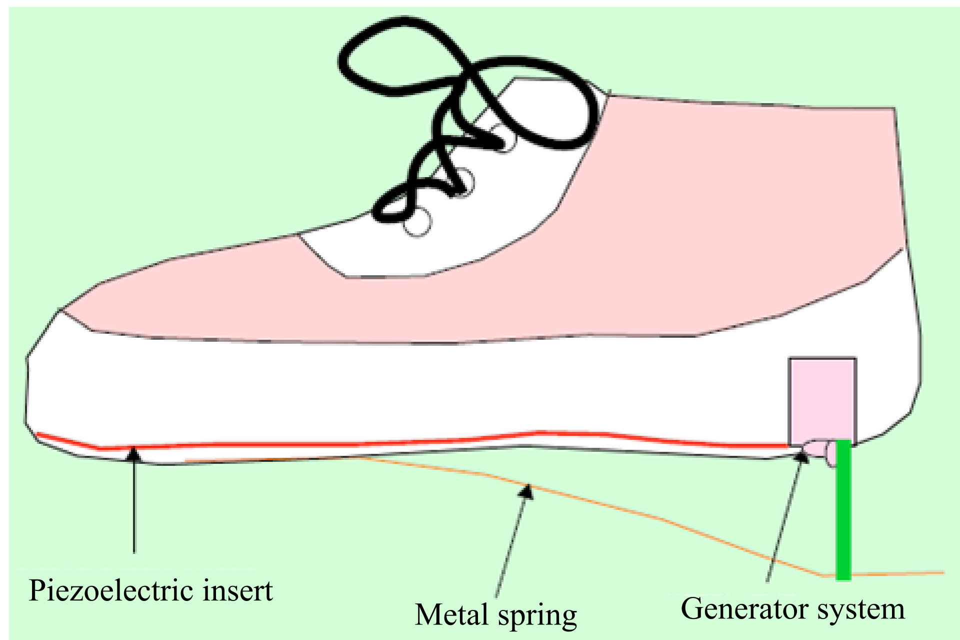

Fig. 1.3 Shoe generation system [15]

This energy could be used in a variety of low-power applications, such as pagers, health monitors, self-powered emergency receivers, and radio frequency identification tags. The application is limited by the piezoelectric and IC integration issues as well as power delivery issues. The piezoelectric shoe inserts offer a good solution for specific requirement such as RFID tags or other wireless devices worn on the foot.

1.1.4 Acoustic noise

Acoustic noise is usually considered as pollution but it can be seen as a power source. In [17], the power density of acoustic noise is 0.96 $\mu W/cm^3$ at 100 dB. The energy level was lower than the power source as mentioned above. Moreover, sound volume of 100 dB closes to the airplane engine, which exceeds the tolerance of human ears. Thus, the power source from the noise is not practical. Recently research and development of this method has extracted limited power from noise with extremely high noise level. Therefore, it is not a feasible power source for common application.

1.1.5 Wind

Wind power is a renewable energy, which is the conversion of wind energy into a useful form like electricity by wind turbines or windmill. A simple eight-blade windmill that could generate electrical power from wind was developed, as shown in Fig. 1.4(a) [18]. The windmill consists of a 750 cm^2 base and a 70 cm long upright, which are used to support the structure. On one end of the axial part there was a pulley which drives the generator, as shown in Fig. 1.4 (b). The generator was designed to working of electromagnetism. A piece of plastic pipe had plastic circles glued to it to form a bobbin for the coil wire. Two magnets were attached on the axial part of plastic pipe. Therefore, the magnets are held in place by their own attraction but it should be glued them in place to promise that they rotate without hitting the sides.

In this case, the power from wind is related to the air velocity. With slow wind at 3 m/s velocity, the average power is about 80 $\mu W/cm^3$. The maximum average power density of 1060 $\mu W/cm^3$ at 12 m/s air velocity was produced from a strong wind. This indicates more usable power can be generated from the large wind.

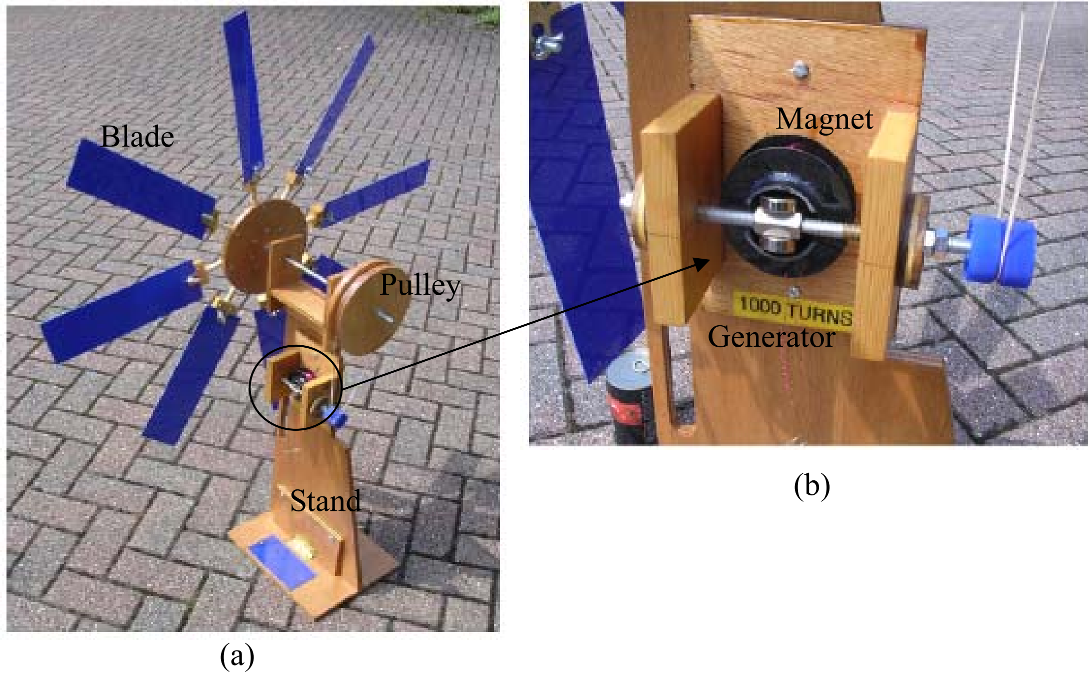

(a) (b)

Fig. 1.4 (a) Photo of the windmill, (b) close-up of the simple generator [18]

ES A 1896

1.1.6 Ambient Vibration

Ambient vibration was present in many environments. Most sources of vibrations in the environment are at low frequencies between 60 and 200 Hz [9]. Low level mechanical vibration occurs in exterior windows, aircraft, automobile, industrial environments, and small household appliances. The maximum power is extracted at resonant with ambient vibration. Theory and experiments show that more than 300 $\mu W/cm^3$ can be generated [19]. A more detailed discussion of this method is presented in Chapter 2.

1.1.7 Summary of power sources

Comparison of the power source and energy storage devices is shown in Table 1.1. The table presents power sources and the values are estimates taken from literature or analysis. Based on the above survey, vibration is chosen as the source of energy scavenging due to its ubiquity and sufficient power density.

Table 1.1 Comparison of power sources

Power sources	Power density	Commercially available?
Solar (outdoors) [10]	15, 000 μW/cm^2	Yes
Solar (indoors) [10]	10 μW/cm^2	Yes
Temperature gradient [13]	140 μW/cm^3 at 100˚C gradient	Soon
Human power [15, 16]	330 μW/cm^2	No
Acoustic noise [17]	0.96 μW/cm^3 at 100dB	No
Wind energy [18]	1060 μW/cm^3 at 12 m/s velocity	No
Vibration [19]	More than 300μW/cm^3	No

1.2 Ambient vibration energy conversion

According to the previous overview, ambient vibration can be used to convert energy into electrical power which is discussed in this section. Three methods are typically used to convert vibration energy to electrical power. There are respectively piezoelectric conversion, electromagnetic inductive conversion, and the electrostatic capacitive conversion.

1.2.1 Piezoelectric energy conversion

The piezoelectric energy conversion converts mechanical energy to electrical energy by the piezoelectric effect of a piezoelectric material. The piezoelectric energy converters are based on two-layer benders (or bimorphs) mounted as a cantilever beam with a mass attached, as shown in Fig. 1.5 [19]. The top and bottom layers of the devices are composed of piezoelectric materials. When the beam bent down, it produced a tension in the top layer and compresses the bottom layer. A voltage is built across each of the layer which we can condition and use to drive a load circuit.

Energy harvesting circuitry for piezoelectric were already reported in [20]. The objective of this paper is to develop an approach that maximizes the power transferred from a vibrating piezoelectric transducer to an electrochemical battery. Due to the AC signal produced by the piezoelectric element and the needs of DC voltage for the circuit, an AC-DC rectifier must be connected to the output of the piezoelectric device. In this circuit, the maximum output power was 18 mW with a power density of 1.86 mW/cm^3 for the vibration frequency of 53.8 Hz.

Other works on piezoelectric converters were also conducted [21], which utilized the piezoelectric film of PZT deposited on a steel cantilever by a low temperature process. But this material is not compatible with the IC process. Another drawback of piezoelectric converter is the requirement of the additional circuitry to rectify the AC current and convert the extracted power. The supplementary circuitry has power losses and decreases the efficiency of the conversion. Most researches so far utilize bulk materials, which is not suitable for integration with microsystem technology.

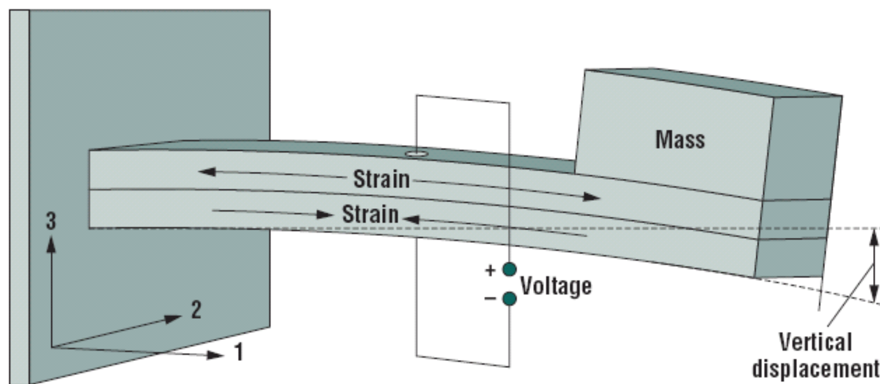

Fig. 1.5 A two-layer cantilever beam piezoelectric energy converter [19]

1.2.2 Electromagnetic energy conversion

In electromagnetic energy conversion, any magnetic flux linkage changes in a coil can induce a voltage or electromotive force (EMF) from Faraday’s law. A typical electromagnetic energy converter is shown in Fig. 1.6 [22]. Mechanical acceleration is

produced by vibrations that cause the mass to move and oscillate. A coil is attached to the mass and moves through a magnetic field built by a permanent magnet. The induced voltage was produced by the change of magnetic flux. Thus, the output power is proportional to the magnetic field and coil number.

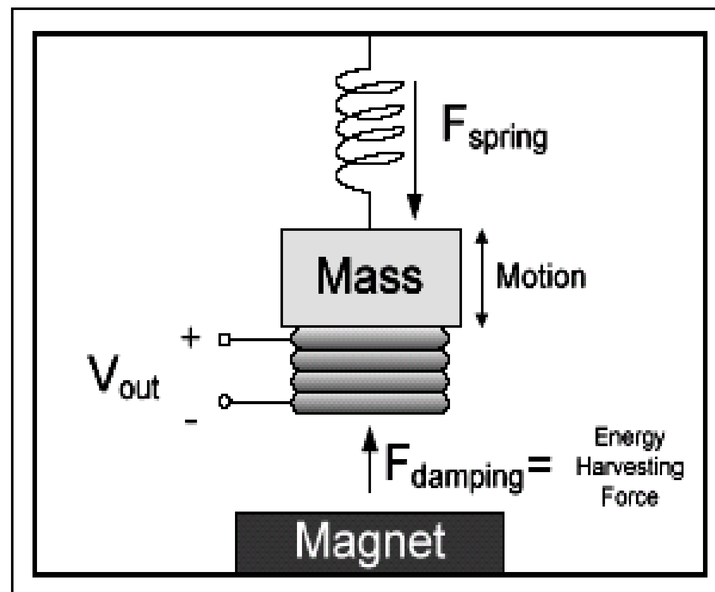

Fig. 1.6 Electromagnetic energy converter [22]

Cao [23] has presented a novel integrated electromagnetic generator system which has a maximum output power level of 35 mW for the vibration source with an amplitude of 3 mm and frequency of 40 Hz. The system consists of an electromagnetic power generator, an interface electronic circuit and an energy storage device, as shown in Fig. 1.7. The energy harvesting circuit was implemented on a 0.35-μm CMOS IC chip.

The most common issue for electromagnetic energy conversion is the relatively low induced voltage. Methods to increase induced voltage include increasing the number of turns of the coil or increasing the permanent magnetic field. However, it is difficult to fabricate large number of coils with planer thin film processes. Thus the power density of electromagnet converter is lower than other types of device.

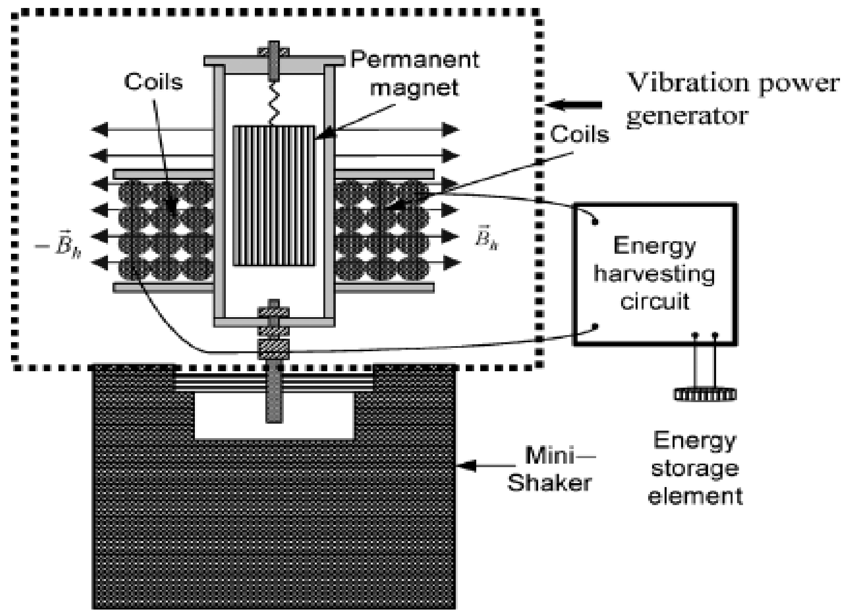

Fig. 1.7 Schematic of an electromagnetic generator system [23]

1.2.3 Electrostatic energy conversion

Electrostatic capacitive energy conversion depends primarily on the changing capacitance of a variable capacitor, as shown in Fig. 1.8.

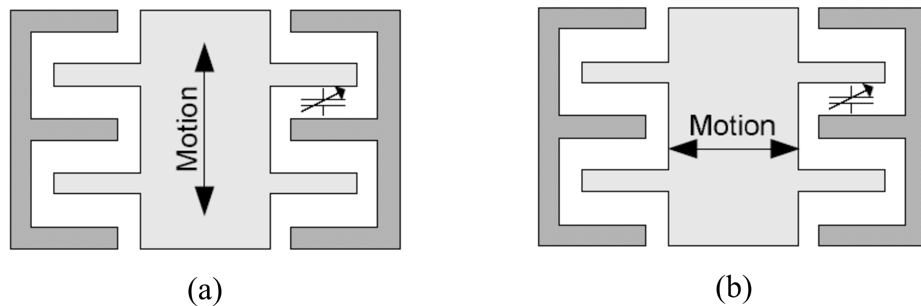

Fig. 1.8 (a) Gap-closing and (b) overlap in-plane variable capacitors [22]

The variable capacitor is pre-charged initially and subsequently disconnected from the source. In the constant charge Q process, the capacitance decreases due to vibration between the fingers. Now the voltage on the variable capacitor increases ($Q_{constant}$=CV) and thus converts the kinetic energy into electrical energy.

The feature of the electrostatic energy converter is its IC process compatibility. MEMS variable capacitor can be fabricated through mature silicon-based micromachining process such as deep reactive ion etching. Therefore, it is suitable for conventional IC process. The converter also provides high output voltage levels and adequate power density. However, the disadvantage of the converter is the need of an auxiliary voltage source V_{in} to initiate the conversion cycle. Therefore, the lifetime of the voltage source is limited. The issue can be solved by employing inductive flyback circuitry proposed by Bernard et al. [24], which constantly feedbacks the temporary storage energy to the external voltage supply for further usage. Besides, one can also employ a moving layer of permanently embedded charge, or electret, to carry out electric energy harvesting [25], although such systems currently have power densities inferior to those using variable capacitors.

A capacitive energy converter was implemented by Meninger et al. [26]. The comb finger structure was used in MEMS technology with silicon on insulator (SOI) wafers. The simulation showed an output power of 8.6 μW with a device size of 1.5 cm × 0.5 cm× 1 mm from the vibration source of 2.52 kHz. Another design was proposed by Roundy [9], which could achieve an output power density of 110 $\mu W/cm^3$ under vibration input 2.25 m/s^2 and frequency of 120 Hz.

In capacitive energy conversion, the switch timing control should be controlled accurately in order to optimize conversion efficiency. A prototype circuitry with the two ideal diodes was proposed by Roundy [9]. The experimental results showed excessive power reduction due to the far from ideal operation of the diodes. The power consumption by the electronics or parasitic capacitive and resistive coupling still existed in the designs. Therefore, improved switch design is critical for better energy conversion efficiency.

1.2.4 Comparison of energy conversion technologies

According to the above literature overview, the three types of energy converter are listed in Table 1.2 [22]. According to the characteristic comparison of these energy converters, electrostatic capacitive vibration-to-electric energy conversion is suitable for scavenging ambient energy because of ubiquity in the environment and sufficient output power density. The fabrication technologies for electrostatic converter are very mature in MEMS system. The materials and process are compatible with IC process.

Table 1.2 Three type of energy converter comparison [22]

Type	Estimated power (in 1 cm^2 or 1 cm^3)
Piezoelectric	~200 μW
Electromagnetic	< 1μW
Electrostatic	1-100μW

1.2.5 Our previous work

Our past design of capacitive energy conversion with integrated mechanical switch has been conducted [27]. The achievement of the previous device includes the realization of integrated mechanical switches. Besides, the improvement of fabrication process and electrical power measurement was conducted. However, the leakage resistance was existed in the variable capacitance.

1.3 Thesis objectives and organization

Our previous design [27] shows the mechanical switches can be integrated successfully in the electrostatic generator in order to acquire the precise timing control. Besides, the parasitic effect causes power dissipation due to fabrication errors. More

detail will be presented in Chapter 3. Therefore, the goals of this thesis are as the following:

(a) Design and analyze of the optimal power for the electrostatic converter with no external mass attached,

(b) Propose novel theory for describing the dynamic model of energy converter,

(c) Improve the performance and eliminate unwanted parasitic effects,

(d) Continue the AC mode circuit measurement with external mass and DC mode circuit test on the devices.

The organization of this thesis is as the following. The principle and design of the energy converter are presented in Chapter 2. The fabrication process and results are described in Chapter 3. The measurement results and discussion are shown in Chapter 4. Finally, conclusion and future work are discussion in Chapter 5.

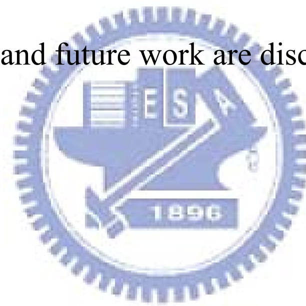

Chapter 2 Principle and Design

Micro electrostatic capacitive energy converter relies on the change of capacitance of a variable capacitor caused by vibration. Thus, the kinetic energy is converted into the electrical energy during this process. The variable capacitor is initially charged by an external power supply such as a battery. The charge-discharge cycles are controlled by switches. The optimum design and analysis will be presented in this chapter. Theoretical model was established to describe the device characteristics and also compared with simulation model of our previous design.

2.1 Characteristics of vibration sources

As mentioned above, vibration sources are generally more ubiquitous. The output power of a vibration driven converter depends on the nature of the vibration source, which should be known in order to estimate the generated power. There are various kinds of vibration sources in the environment. Measurement of different vibration sources was conducted by Roundy [9], as shown in Fig. 2.1. From the low level vibration sources, two results can be observed. First, fundamental peaks occur at a common low frequency. Second, the high frequency vibration modes are lower in acceleration magnitude than the low frequency fundamental modes. Low level vibration in typical households, offices, and manufacturing environments is considered also as a possible power source for wireless sensor nodes.

Our measurement of the vibration spectrum of a dehumidifier is shown in Fig. 2.2. A piezoelectric accelerometer was put on the dehumidifier and the data was collected by an oscilloscope. The fundamental vibration mode is at about 120 Hz, as observed by Roundy. The peak acceleration of the dehumidifier is about 2.2m/s^2 at

about 120 Hz, as shown in Fig. 2.3. These results will be used as our targeted input vibration source due to its common existence.

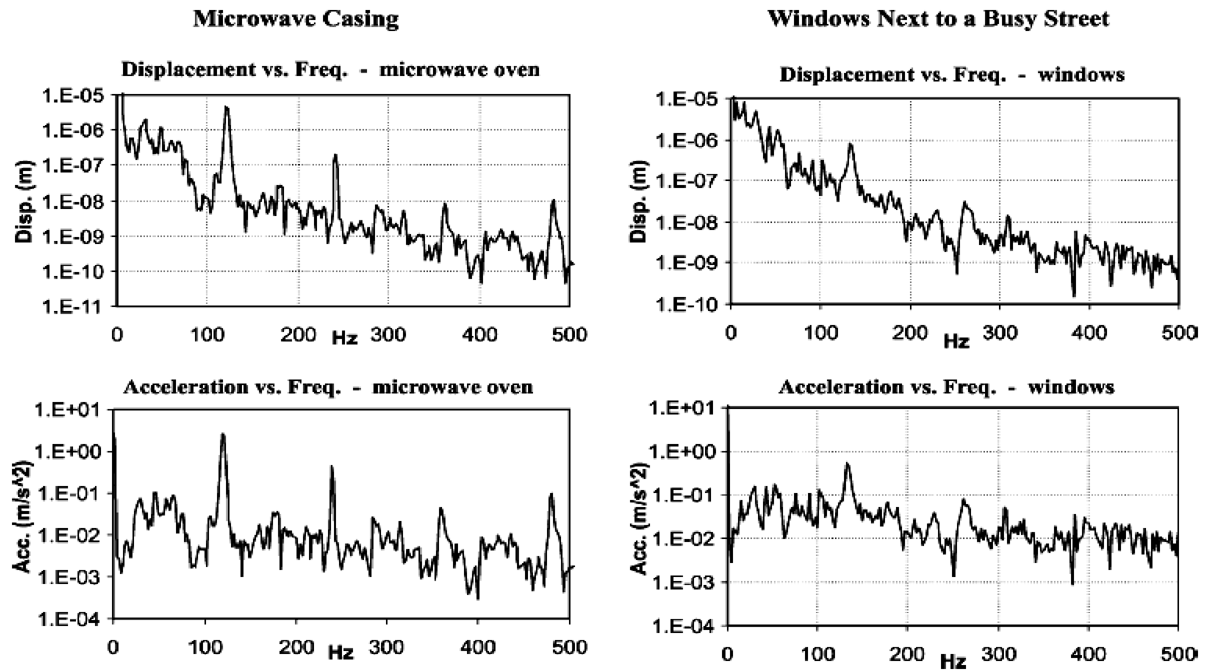

Fig. 2.1 Vibration spectra by Roundy [9]

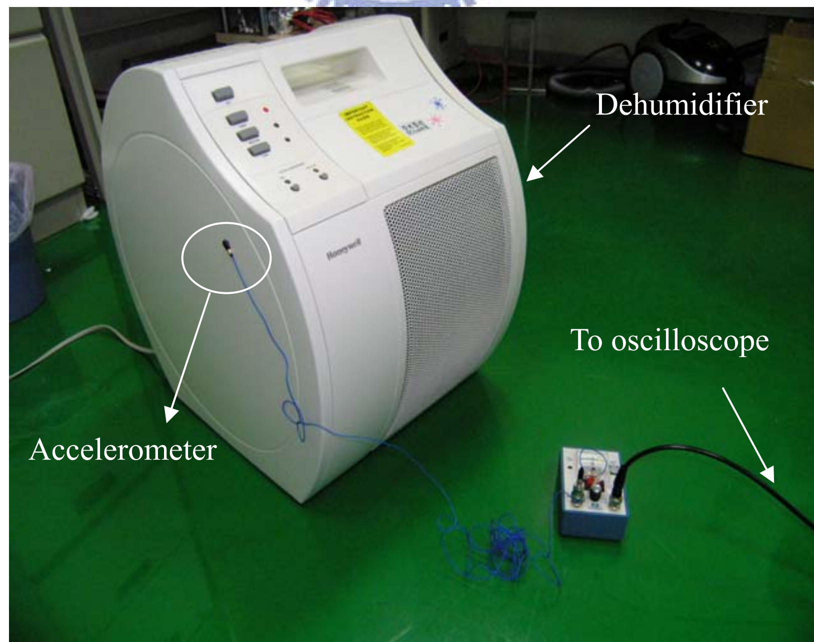

Fig. 2.2 Measurement of dehumidifier vibration

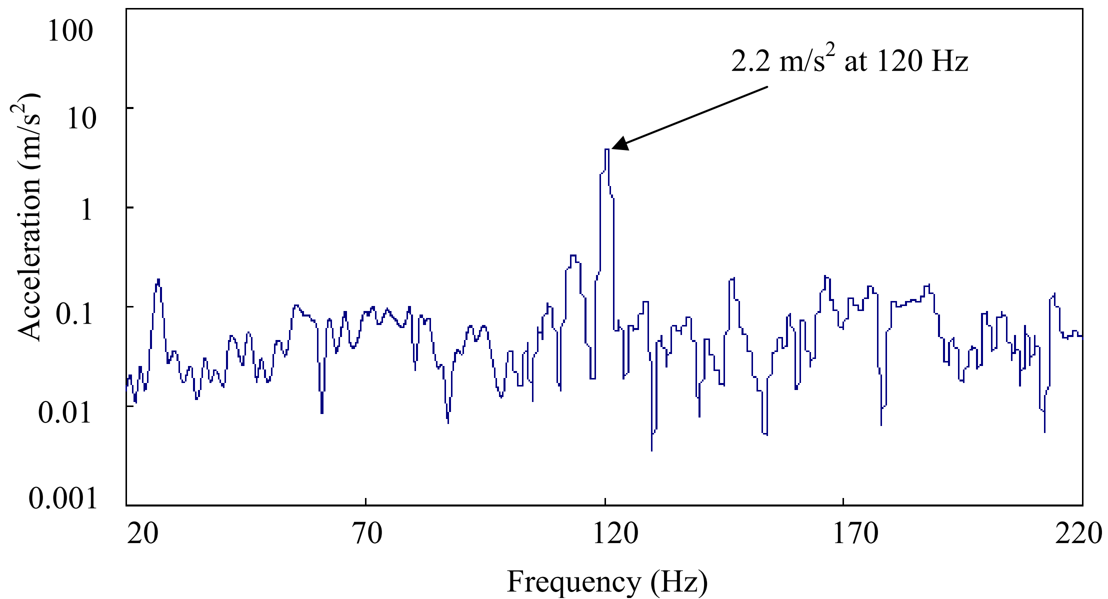

Fig. 2.3 Vibration spectrum of a dehumidifier

2.2 Operational principle

The main component of the electrostatic energy converter is a variable capacitor C_v [28]. A schematic circuit of the energy converter is shown in Fig. 2.4. It is composed of an auxiliary battery supply V_{in}, a vibration driven variable capacitor C_v and an output storage capacitor C_{stor}, which is connected to the load R_L. Two switches, SW1 and SW2, are used to connect these components and control the charge-discharge conversion timing [27].

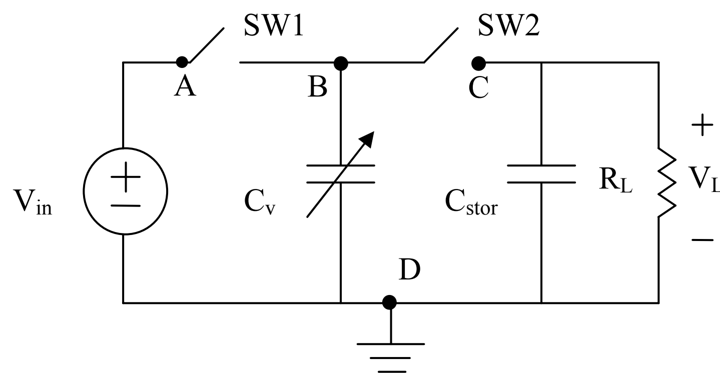

Fig. 2.4 Operation circuit of the electrostatic energy converter

A more detailed schematic of the energy converter is shown in Fig. 2.5. The change of the capacitance is driven by the external vibration source. SW1 is implemented by a contact mechanism between nodes A and B. SW2 is actuated the electrostatic pull-in force between nodes B and D. When the node B reaches the pull-in voltage, it will be attracted by the node D and touch node C.

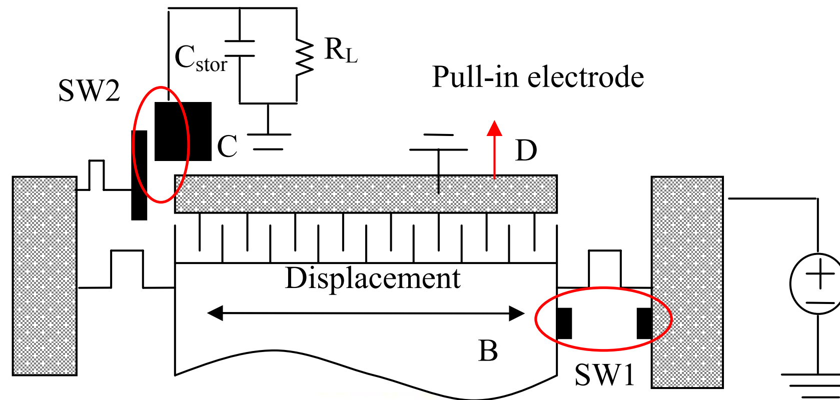

Fig. 2.5 Variable capacitor schematic

In the beginning, the variable capacitor C_v is charged by the auxiliary voltage supply V_{in} through the switch SW1 when C_v is at its maximum C_{max}, as shown in Fig. 2.6. After C_v is charged to V_{in}, SW1 is opened and the capacitance changes from C_{max} to C_{min} due to the electrode displacement by vibration. In the process, the charge Q on the capacitor remains constant (SW1 and SW2 both open). Therefore, the terminal voltage across the capacitor C_v is increased and the mechanical energy is converted to the electrical energy stored in the capacitor.

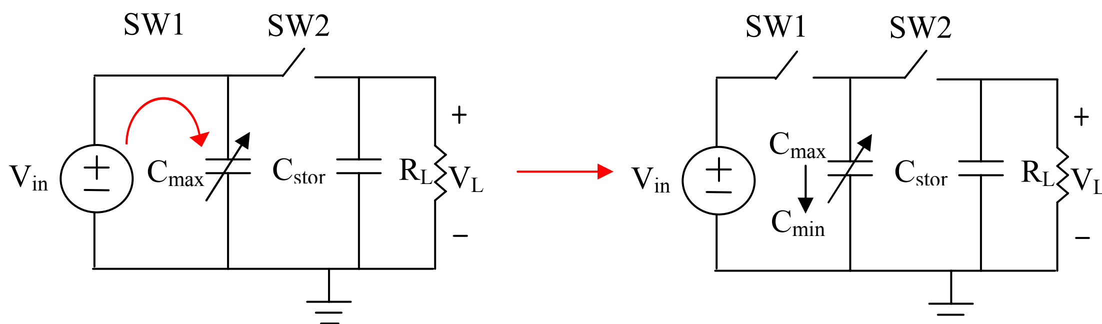

Fig. 2.6 Capacitor charging and capacitance change by vibration

When the capacitance reaches C_{min} and terminal voltage reaches V_{max}, SW2 is closed and the charge redistributes between C_v and C_{stor}, as shown in Fig. 2.7 [29]. The energy stored in the variable capacitor C_v is transferred to the the storage capacitor C_{stor}. SW2 is then opened and C_v varies back to C_{max}, preparing for the next conversion cycle. The charge on C_{stor} is dissapated through the load resistance R_L with a time constant $\tau = R_L C_{stor}$ before it is charged again by C_v. The output voltage V_L will eventually reach the steady state when the initial and final voltages of the charge-discharge process become equal.

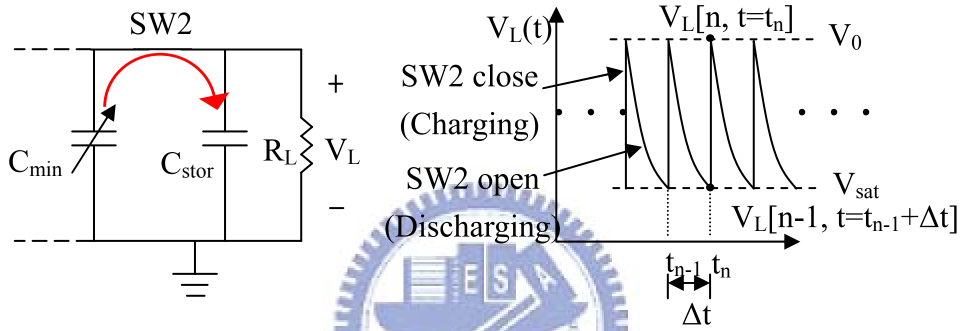

Fig. 2.7 Charge transfer and discharge process [29]

Let the conversion cycle time be Δt, the output voltage of the n-th cycle before and after the charge transfer can be expressed as [29]

$$V_{\mathrm{L}}[\mathrm{n},\, t=t_{\mathrm{n}}]=\frac{V_{\mathrm{L}}[\mathrm{n}\text{-}1, t=t_{\mathrm{n}\text{-}1}+\Delta t]C_{\mathrm{stor}}+V_{\max}C_{\min}}{C_{\mathrm{stor}}+C_{\min}}, \tag{2.1}$$

where V_{max} is equal to $V_{in}C_{max}/C_{min}$, V_L [n-1, t = t_{n-1}+Δt] is the voltage before the charge transfer, and V_L [n, t = t_n] is the voltage after the charge transfer. After SW2 is opened, the output voltage in this charge dissiaption period can be expressed as

$$V_{\mathrm{L}}[\mathrm{n},\, t=t_{\mathrm{n}}+\Delta t]=\frac{V_{\mathrm{L}}[\mathrm{n}\text{-}1,\, t=\mathrm{t}_{\mathrm{n}}+\Delta t]C_{\mathrm{stor}}+V_{\max}C_{\min}}{C_{\mathrm{stor}}+C_{\min}}\times\exp(\text{-}\Delta t/R_{\mathrm{L}}C_{\mathrm{stor}}), \tag{2.2}$$

If the charge transferred to C_{stor} is more than that discharged through the output load, the net increment will result in the rises of V_L step by step. In the steady state, the net increment of charge transfer to C_{stor} becomes zero and the initial and final value of V_L

becomes the same. From the Eq. 2.2, the final saturation voltage of the output terminal can be derived as

$$V_{sat} = \frac{\frac{C_{max}}{C_{stor}} V_{in}}{(1+\frac{C_{min}}{C_{stor}}) \times \exp(\Delta t / R_L C_{stor}) - 1}, \tag{2.3}$$

where Δt = conversion cycle time = 1/2f and f is the vibration frequency. The average output power can be calculated as

$$P(t) = \frac{V_L^{\,2}(t)}{R_L} = \frac{(V_0 e^{-t/R_L C_{stor}})^2}{R_L}, \tag{2.4}$$

$$P_{out} = \frac{1}{\Delta t}\int_0^{\Delta t} P(t)dt = \frac{C_{stor} V_0^{\,2}}{2\Delta t}[1-\exp(\frac{-2\Delta t}{R_L C_{stor}})] \approx \frac{V_{sat}^{\,2}}{R_L}, \tag{2.5}$$

where $V_0 = V_{sat} \times e^{\Delta t / R_L C_{stor}}$, as shown in Fig. 2.7. The approximation takes place when $\Delta t << R_L C_{stor}$, which also results in a small output voltage ripple.

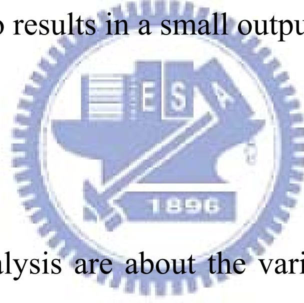

2.3 Device design

The main design and analysis are about the variable capacitor structure. In our previous designs [29], an external mass should be put on the center hole of the electrostatic converter to adjust the resonant frequency to 120 Hz as mentioned above. The mass of the microstructure below the external mass was ignored. Therefore, the focus of the design is on the optimum power analysis of the device with no external mass attachment. Due to the small mass of microstructures, a little vibration force is needed to drive the variable capacitor structure. Another advantage is to increase the power density because of decreased volume of the device. In the design without the external mass, the vertical force during the vibration is reduced so that the microstructure damage can be alleviated.

The optimum power analysis is based on Eq. 2.5. The power strongly depends on the maximum capacitance C_{max}. But the electrostatic force increases with the C_{max} ,

indicating that it influences the device vibration movement. Due to the constraint of 1 cm^2 device area and electrostatic force, the maximum capacitance was limited and thus influencing the subsequent variable capacitor design.

2.3.1 Auxiliary power supply

The auxiliary power supply is used to pre-charge the variable capacitor through SW1. The power supply can be a capacitor or rechargeable battery. But this power supply has lifetime and mass issues in some microstructure. In [24], the researcher provided a good method to store the converted energy to convert energy in storage elements in order to provide power and energy more smoothly. In the device without the external mass, the input voltage was chosen as 0.3 V of solar battery to reduce the electrostatic force and avoid the pull-in phenomenon in the charging process.

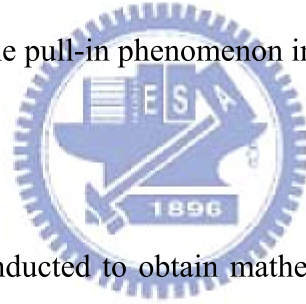

2.3.2 Static analysis

The static analysis is conducted to obtain mathematical guidelines for deciding overall parameters. With Eq. 2.3 the circuit components can be chosen such that $C_{stor} \gg C_{min}$ and $R_L C_{min} \ll \Delta t$. Therefore, Eq. 2.3 can be simplified as

$$V_{sat} \approx \frac{\frac{C_{max} V_{in}}{\Delta t}}{C_{min} \frac{\Delta t}{R_L C_{min}}} = \frac{C_{max} V_{in}}{\Delta t} R_L. \tag{2.6}$$

The output power becomes

$$P_{out} \approx \frac{{V_{sat}}^2}{R_L} \approx \left(\frac{C_{max} V_{in}}{\Delta t} \right)^2 R_L. \tag{2.7}$$

From the Eq. 2.5, it is possible to find the optimal power obtainable by first finding the optimal load resistance $R_{L,\,opt}$. This is given by the stationary point on

$$\frac{dP_{out}}{dR_L} = 0,$$

$$R_{L,opt} = \frac{1}{2fC_{stor}\ln\left(1+\frac{C_{max}}{C_{stor}}\right)} \tag{2.8}$$

The optimal load resistance depends on the storage capacitor C_{stor} and the maximum capacitance C_{max}. The constraint on C_{max} was discussed as mentioned above. With the Eq. 2.6, the output voltage is below 16 V for the further power management circuit. Thus, the minimum optimum load resistance is 50 MΩ. C_{stor} was chosen to be 5 nF for an output voltage ripple lower than 1 V, which has no effect on the output power from Eq. 2.7.

2.3.3 Dynamic analysis

The objective of dynamic analysis is to determine the relationship between the mechanical spring force and the electrostatic force to achieve the desired maximum displacement under the targeted input vibration. The electro-mechanical dynamics of the variable capacitor can be modeled as a spring-damper-mass system, as shown in Fig. 2.8

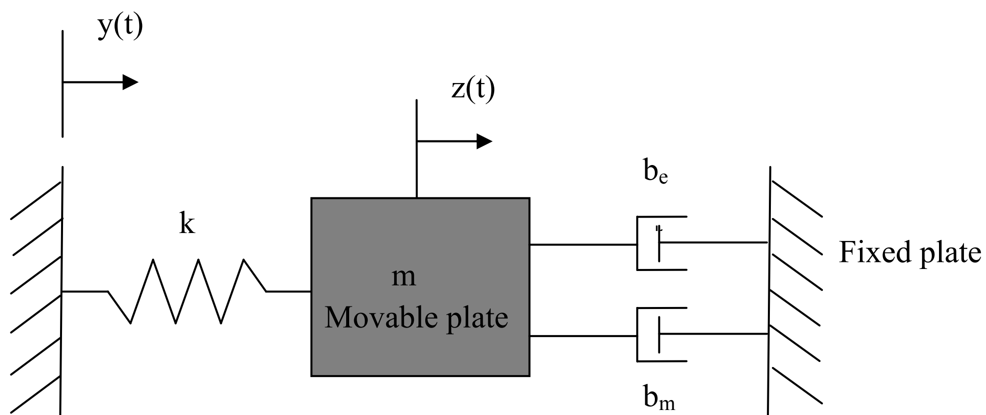

Fig. 2.8 Schematic of the conversion dynamic model

The dynamic equation is

$$m\ddot{z} + b_e z + b_m(z)\dot{z} + kz = -m\ddot{y}, \tag{2.9}$$

where y is the displacement of device frame caused by the vibration, z is the relative displacement between movable and fixed plate, k is spring coefficient, $b_m(z)\dot{z}$ is the mechanical damping force caused by the squeeze film effect, and $b_e z$ is the electrostatic force caused by the charge on the capacitor, which acts as a negative spring force with b_e as the electrostatic spring constant.

In Eq. 2.9, $b_m(z)$ is a function of z. Therefore the system is nonlinear. In order to simplify the analysis, we assume the system is operated in the low damping environment and squeeze film effect is ignored. Constant damping is used as an approximation. The vibration source is assumed to be sinusoidal with complex amplitude *Y* and frequency ω, and the relative displacement with complex amplitude *Z*, Fourier transform is applied to solve the equation

$$|Z| = \frac{m\omega^2}{\sqrt{(k+b_e-m\omega^2)^2+{b_m}^2\omega^2}}|Y|. \tag{2.10}$$

The equation shows the equivalent spring constant is $k' = k + b_e$. The electrostatic spring coefficient influences the spring coefficient. Thus, the resonant frequency of system is

$$\omega_n = \sqrt{\frac{k+b_e}{m}}$$
$$b_e = \frac{Q^2}{2N_g \varepsilon A d} \tag{2.11}$$

where Q is charge on the variable capacitor, N_g is number of comb cells, A is overlap area and d is initial gap between the fingers. These parameters are discussed in detail in the next section. In order to maintain steady resonance, the mechanical spring

constant k should be relatively larger than the maximum electrostatic spring constant (b_{e_max}). The relationship between the spring k and b_{e_max} was already discussed in [27], which presented the ratio of these two parameters r_d increased with the desired maximum displacement z_{max} by Simulink model. But the phenomenon described by Simulink model has no explicit theoretical foundation. Therefore, the detailed description is considered by using theoretical analysis. From the Eq. 2.11, the electrostatic spring coefficient b_e is determined from the charge Q and thus this is a square wave function, as shown in Fig. 2.9.

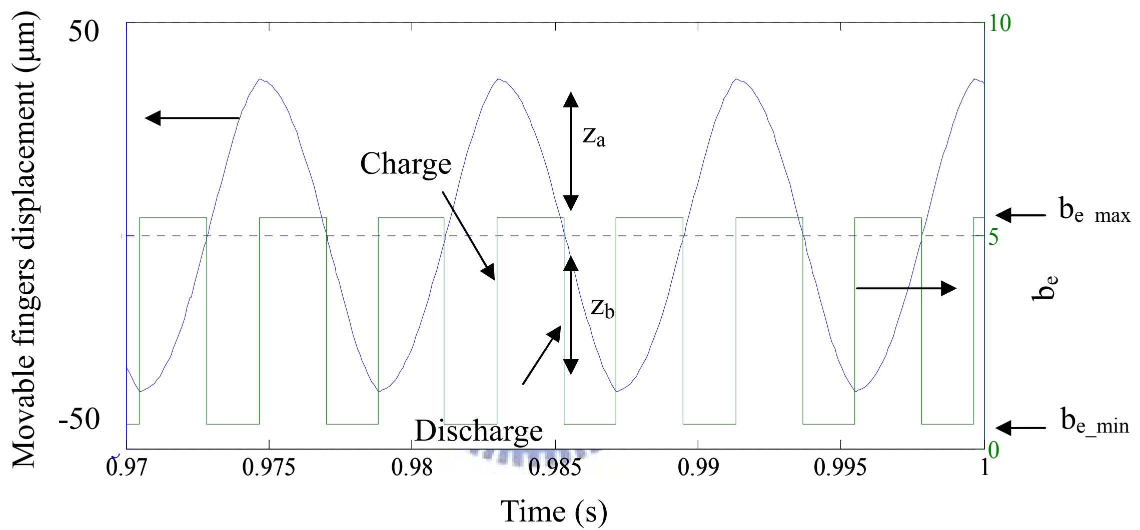

Fig. 2.9 Electrostatic spring constant in the steady state

From the Eq. 2.9 and Eq. 2.11, the vibration source is assume the sinusoidal wave ($y=Y_0\sin\omega t$). In order to solve the equation theoretically, the relative displacement can be described by the two government equations.

$$\begin{aligned} \ddot{z}_a + \frac{b_m}{m}\dot{z}_a + \frac{k_a}{m}z_a &= Y_0\omega_0^2\sin\omega_0 t,\ k_a = k + b_{e_max} \\ \ddot{z}_b + \frac{b_m}{m}\dot{z}_b + \frac{k_b}{m}z_b &= Y_0\omega_0^2\sin\omega_0 t,\ k_b = k + b_{e_min} \end{aligned} \tag{2.12}$$

where z_a is relative displacement between fingers before discharging, z_b is relative displacement after discharging, as shown in Fig. 2.9. The damping coefficient b_m was

assumed to be constant in the low damping environment. Thus, the equations are linear so that solutions are as follows

$$z_{\mathrm{a}} = e^{-\zeta_1 \omega_{\mathrm{a}} t}\left(C_1 \cos\omega_{\mathrm{da}} t + C_2 \sin\omega_{\mathrm{da}} t\right) + z_{\mathrm{pa}}(t) \tag{2.13a}$$

$$z_{\mathrm{b}} = e^{-\zeta_2 \omega_{\mathrm{b}} t}\left(C_3 \cos\omega_{\mathrm{db}} t + C_4 \sin\omega_{\mathrm{db}} t\right) + z_{\mathrm{pb}}(t) \tag{2.13b}$$

where

$$\zeta_{\mathrm{a}} = \frac{b_{\mathrm{m}}}{2m\omega_{\mathrm{a}}};\ \zeta_{\mathrm{b}} = \frac{b_{\mathrm{m}}}{2m\omega_{\mathrm{b}}} \omega_{\mathrm{a}} = \sqrt{\frac{k_{\mathrm{a}}}{m}}\ ,\ \omega_{\mathrm{da}} = \omega_{\mathrm{a}}\sqrt{1-\zeta_{\mathrm{a}}^2}, \omega_{\mathrm{b}} = \sqrt{\frac{k_{\mathrm{b}}}{m}}\ ,\ \omega_{\mathrm{db}} = \omega_{\mathrm{b}}\sqrt{1-\zeta_{\mathrm{b}}^2}.$$

z_{pa} and z_{pb} are the particular solutions of the equation. The two equations can be solved numerically to get a suitable solution. As mentioned above, b_{e_max} must be smaller than spring constant k. Therefore, the coefficient k_a (k_a=k+b_{e_max}) was considered. From the Eq. 2.13(a) and Eq. 2.13(b), the desired displacement (z=z_a+z_b) is relative to the electrostatic spring constant (b_{e_max} and b_{e_min}). The desired maximum displacement was decreased progressively with the maximum electrostatic spring constant b_{e_max} raising. We can utilize the relationship to determine the desired maximum displacement z_{max} by using various maximum electrostatic springs constant. The theoretical analysis results can be compared with the simulation from Simulink, as shown in Fig. 2.10. It shows that the maximum electrostatic spring constant b_{e_max} should be smaller than the mechanical spring constant k to maintain the steady resonance. Thus, the minimum ratio of k/b_{e_max} can be determined from the desired maximum displacement. From the Fig.2.10, the maximum displacement z_{max} was approximately proportional to the minimum ratio of k/b_{e_max} (r_d) for the theoretical value, which can be written as following equation:

$$r_{\mathrm{d}} \approx 0.0875 z_{\max} + 0.8 \tag{2.14}$$

It can be viewed as a linear function.

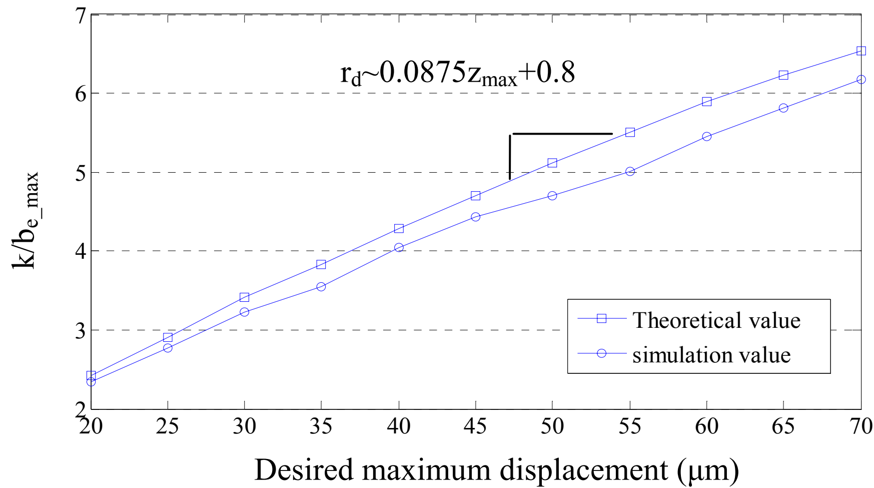

Fig. 2.10 k/be_max versus the desired maximum displacement

2.3.4 Variable capacitor design

From [29], the in-plane gap closing comb structure is used for the variable capacitor, as shown in Fig. 2.11. In Fig. 2.11(a), the dark areas are anchor regions and the light areas are movable regions. The spring of the in-plane gap closing variable capacitor makes it easier to move perpendicular to the finger gaps. Fig.2.11 (b) shows the comb fingers with silicon nitride deposited on the sidewalls for electrical insulation.

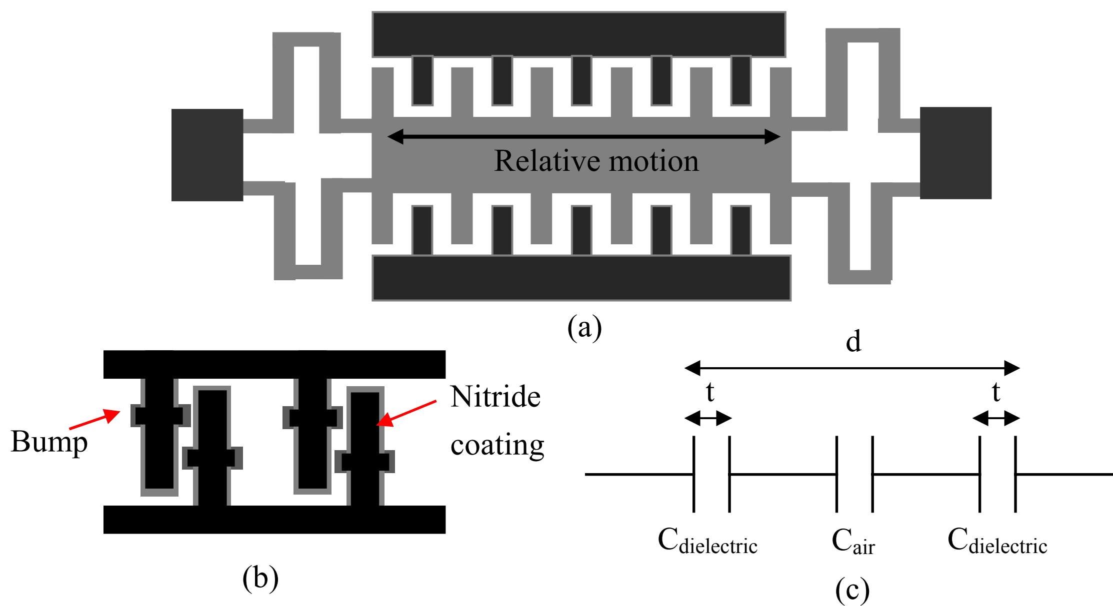

Fig. 2.11(a) Top view of the in-plane gap closing variable capacitor, (b) fingers with silicon nitride coating, (c) equivalent capacitance model between fingers

The symbols used in the following analysis are listed below

d : initial gap between comb fingers,

t : thickness of silicon nitride coated on the sidewalls of fingers,

L_f : overlap length of comb fingers,

W_f : comb finger width,

h : thickness of comb fingers,

N_g : number of variable capacitor cells,

z : relative displacement between the movable and fixed electrodes,

ε_0 : permittivity of free space,

ε_r : relative permittivity of silicon nitride (ε_r=7)

The thickness of silicon nitride t is 500 Å to avoid the electronic tunneling effect in the charging process. The bumps on the sidewalls of the fingers keep the minimum finger spacing at 0.5 μm. Fig. 2.11 (c) shows the equivalent air gap of the capacitor is $d_{eq} = d - 2t + \frac{2t}{\varepsilon_r}$ with dielectric thickness t and relatively permittivity ε_r. The total variable capacitance between the comb fingers is [29]

$$C_v(z)=N_g\varepsilon_o L_f h\left(\frac{2(\frac{2t}{\varepsilon_r}+d-2t)}{(\frac{2t}{\varepsilon_r}+d-2t)^2-z^2}\right). \quad (2.15)$$

From this equation, the variable capacitance strongly depends on the comb finger structure. A general model of the comb finger structure is shown in Fig. 2.12. The layout includes the movable plate and fingers. A number of free parameters can be adjusted to obtain the optimal output power. The guideline of the optimization of parameters was also presented in [30, 31].

As mentioned above, the output power of the device is produced by the variable capacitor, which is formed by the comb fingers. W_0 and L_0 are the width and length of

the layout. W_1 is the movable plate width on both side in the x-axis direction and W_2 is in the y-axis direction. These two parameters determine the mass of the movable plate. W_1 should be designed as large as possible because it determines the number of fingers, which is related to the output power. But the initial gap between fingers d also influences the number of fingers for a given chip area constraint. W_2 is determined by the overlap length of fingers L_f. In order to have much output power, the comb structure center width should be designed as small as possible to have much number of fingers. But the robustness should be considered during vibration. Without external mass attachment structure design, the comb fingers structure has the center width of 1000 μm to ensure the robust structure and power requirement.

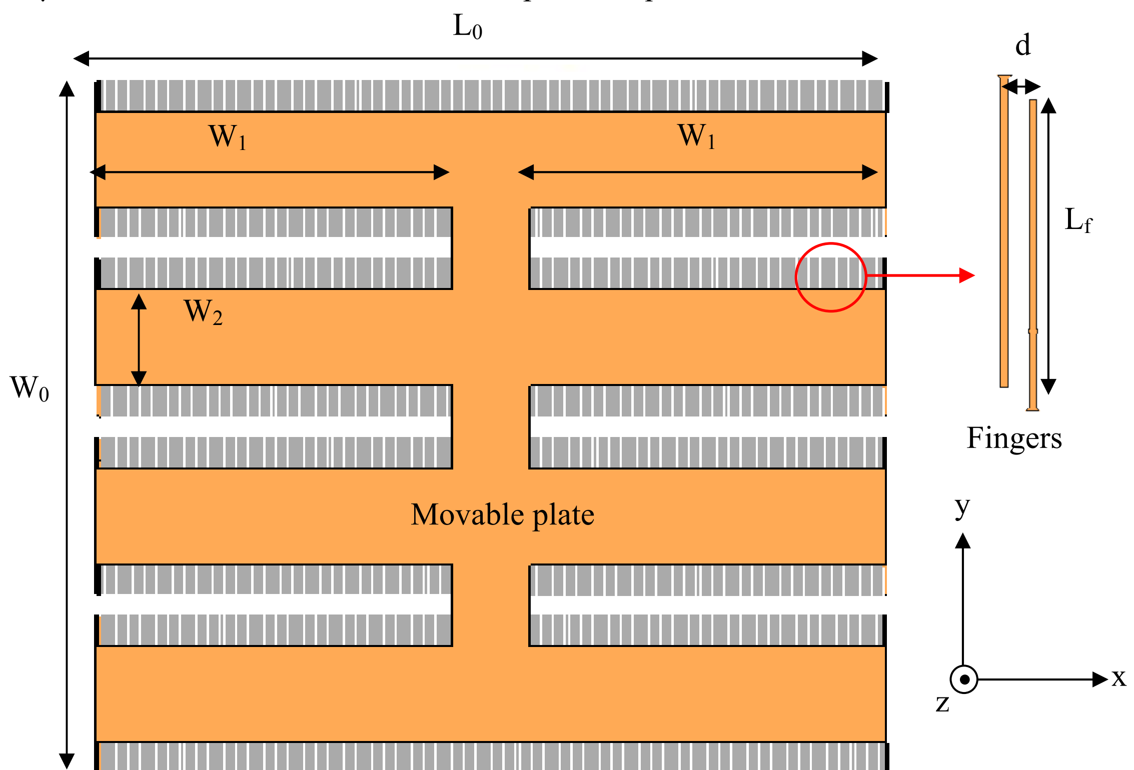

Fig. 2.12 A general model of the movable plate

The output power versus variable capacitor parameters is calculated according to Eq. 2.5 and Eq. 2.6. Device will be fabricated on the SOI wafer. The thickness h is choosing as 200 μm to have large capacitance. The finger width W_f of 10 μm is

restricted by the aspect ratio up of to 20:1 in the deep reactive ion etching process.

The mechanical damping force between fingers for large displacement is [32]

$$F_m = b_m(z)\dot{z} = \left(\alpha \frac{\mu N_g L_f h^3}{(d-2t)^3 \left[1-(\frac{z}{d-2t})^2 \right]^{1.5}} \right) \dot{z} \approx \left(\alpha \frac{\mu N_g L_f h^3}{(d-2t)^3} \right) \dot{z}, \tag{2.16}$$

with $b_m(z)$ as the equivalent mechanical damping constant. Device was operated in low damping environment that can improve the quality factor especially. The squeeze film damping effect can be ignored in the low damping environment. Thus, the mechanical damping constant is independent of the relative displacement z. Thus, the damping force is proportional to the velocity $\dot{z}$. The electrostatic force induced by the charge Q on C_v is [28]

$$F_e = b_e z = \left[\frac{-Q^2}{2N_g \varepsilon_o L_f h(\frac{2t}{\varepsilon_r} + d - 2t)} \right] z. \tag{2.17}$$

The force is proportional to the negative displacement of the movable plate. The b_e can be regarded as the electrostatic spring constant. The electrostatic spring constant is determined by the charge Q on the variable capacitor which varies in the charge-discharge process. The maximum electrostatic spring constant b_{e_max} will reduce the total spring constant and make the movement unsteady during the vibration. Therefore, the b_{e_max} should be limited as

$$b_{e_max} = \frac{Q_{max}^{\ 2}}{2N_g \varepsilon_o L_f h(\frac{2t}{\varepsilon_r} + d - 2t)} \le \frac{k}{r_d} = \frac{\omega_n^{\ 2} m}{r_d} = b_{e_max_lim}, \tag{2.18}$$

$$m = \rho h[2N_g W_f (L_f + d) + 8W_1 W_2 + (L_0 - 2W_1)W_0]. \tag{2.19}$$

The mass m of the movable plate is related to the density and thickness h of the device. According to Eq. 2.18 and Fig. 2.10, the limitation of the electrostatic spring constant $b_{e_max_lim}$ is related to the ratio r_d between the mechanical spring k and b_{e_max}

which increased with the desired maximum displacement (Eq. 2.14). With the above design parameters, the relationships of the b_{e_max} and $b_{e_max_lim}$ are the functions of the initial gap d and the finger overlap length L_f, as shown in Fig. 2.13(a). If the b_{e_max} layer is below the $b_{e_max_lim}$ layer, it indicated the electrostatic spring softening effect can be ignored for the steady resonance at mentioned above. Fig. 2.13(b) is the two-dimension diagram of Fig. 2.13(a), which shows the available region that indicated b_{e_max} layer was below $b_{e_max_lim}$ layer. Otherwise it is unavailable region. In Fig. 2.14, we can obtain the maximum power of 0.51 μW (power density of 12 μW /cm^3) with the maximum displacement 36.4 μm and finger overlap length 535 μm in the available region. In this analysis, the initial gap between the fingers is 37 μm and the variable capacitance changes from 40 pF to 2080 pF. The output voltage is 5 V and the mass of movable plate is 0.0365g. The spring constant was 21 N/m to fit in with the resonant frequency of 120 Hz. Design parameters of the variable capacitor are listed in Table 2.1.

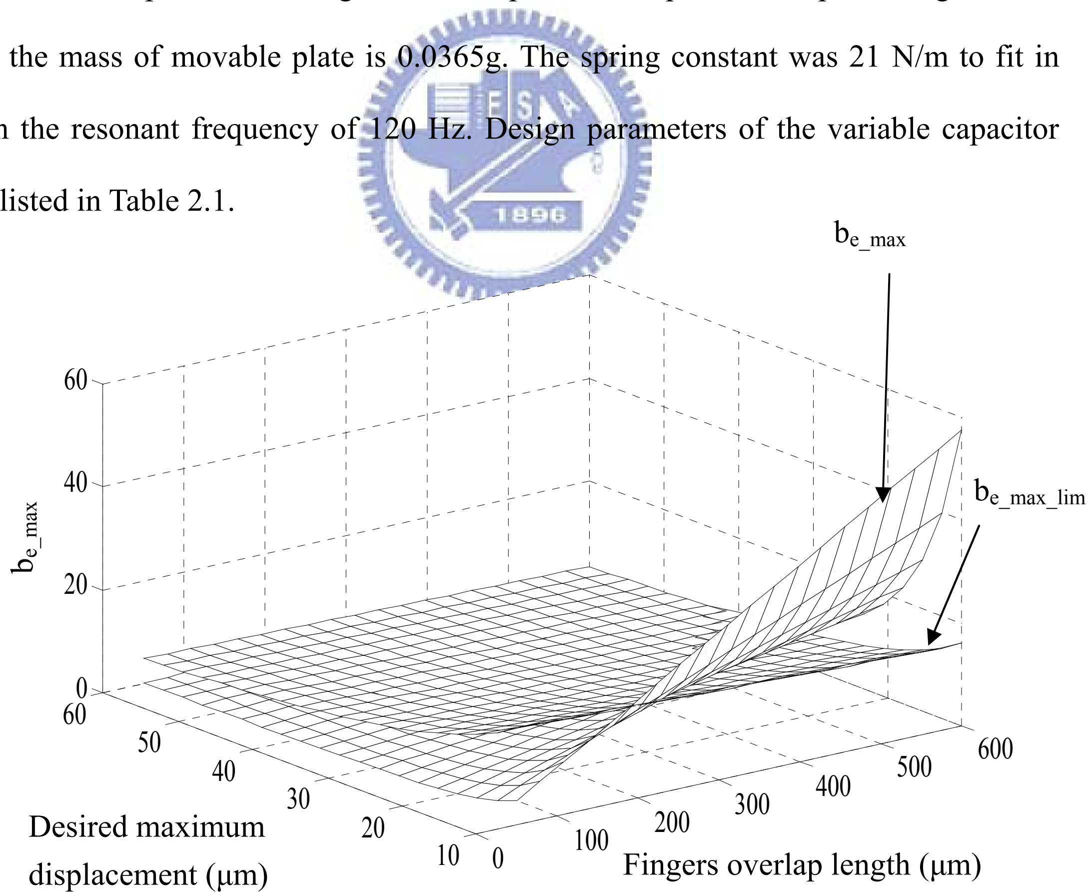

Fig. 2.13 b_{e_max} constraint for (a) three-dimension (b) two-dimension diagram

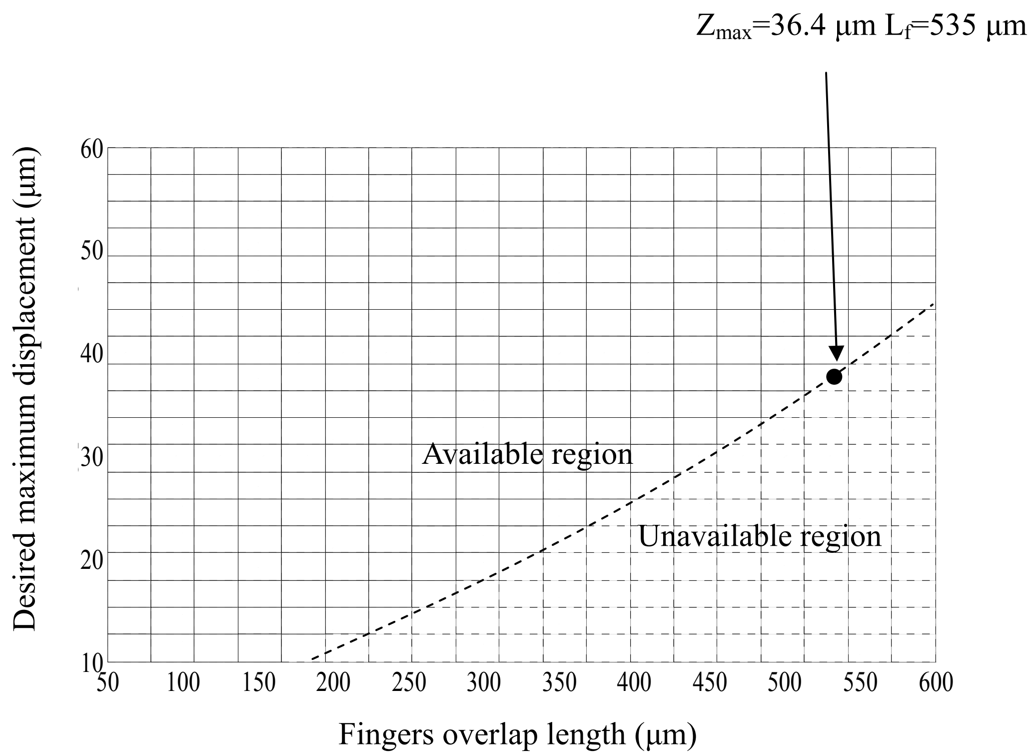

Fig. 2.13 b_{e_max} constraint for (a) three-dimension (b) two-dimension diagram (continued)

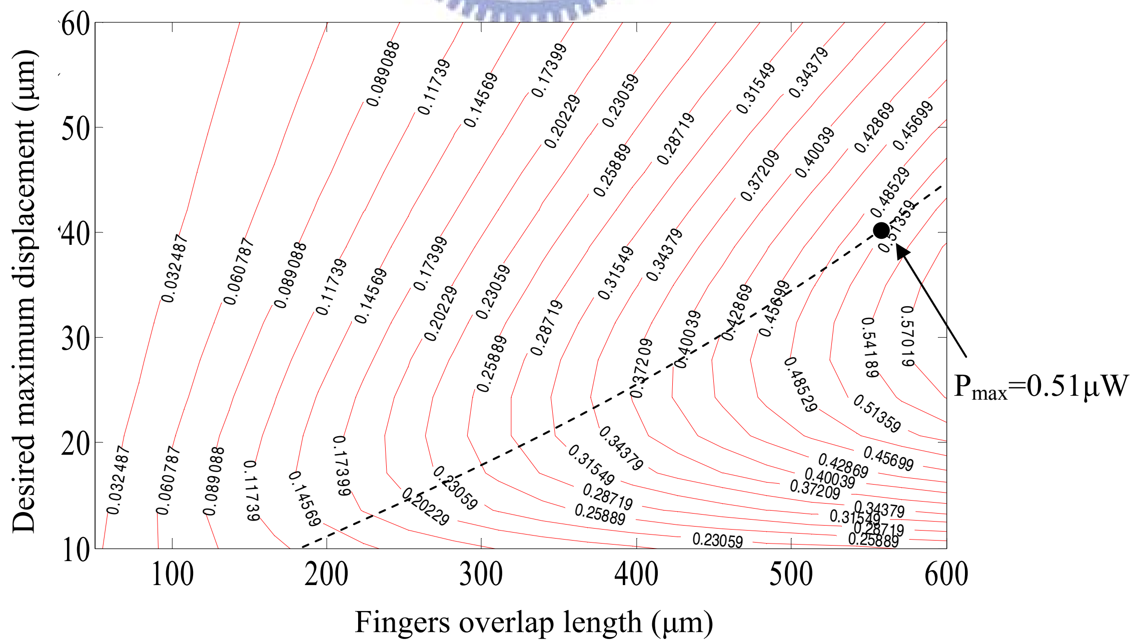

Fig. 2.14 Output power versus desired maximum displacement and finger overlap length

Table 2.1 Variable capacitor design parameters

Variable	Description of variables	Designed value
h	Device thickness	200 μm
N_g	Number of variable capacitor cells	788
W_f	Finger width	10 μm
L_f	Finger overlap length	535 μm
d	Finger initial gap	37 μm
Z_{max}	Maximum displacement	36.4 μm
t	Silicon nitride sidewall thickness	500 Å
C_{max}	Maximum value of capacitance	2080 pF
C_{min}	Minimum value of capacitance	40 pF
k	Mechanical spring const.	21 μN/μm
m	Mass of movable plate	36.5mg
R_L	Driven load resistance	50 MΩ
C_{stor}	Output temporary storage capacitor	5 nF
V_{out}	Output voltage (steady state)	5 V
P_{out}	Output power (steady state)	0.51 μW

2.3.5 Spring design

In the mechanical spring design, the device without external mass attached will need a soft spring to fit in with the resonant frequency due to the small mass of the movable plate. Thus, the serpentine spring structure was considered. The primary deformation is along the direction of relative displacement so that the spring constant in the x-direction is used for device design. The schematic of folded serpentine spring structures is shown in Fig. 2.15.

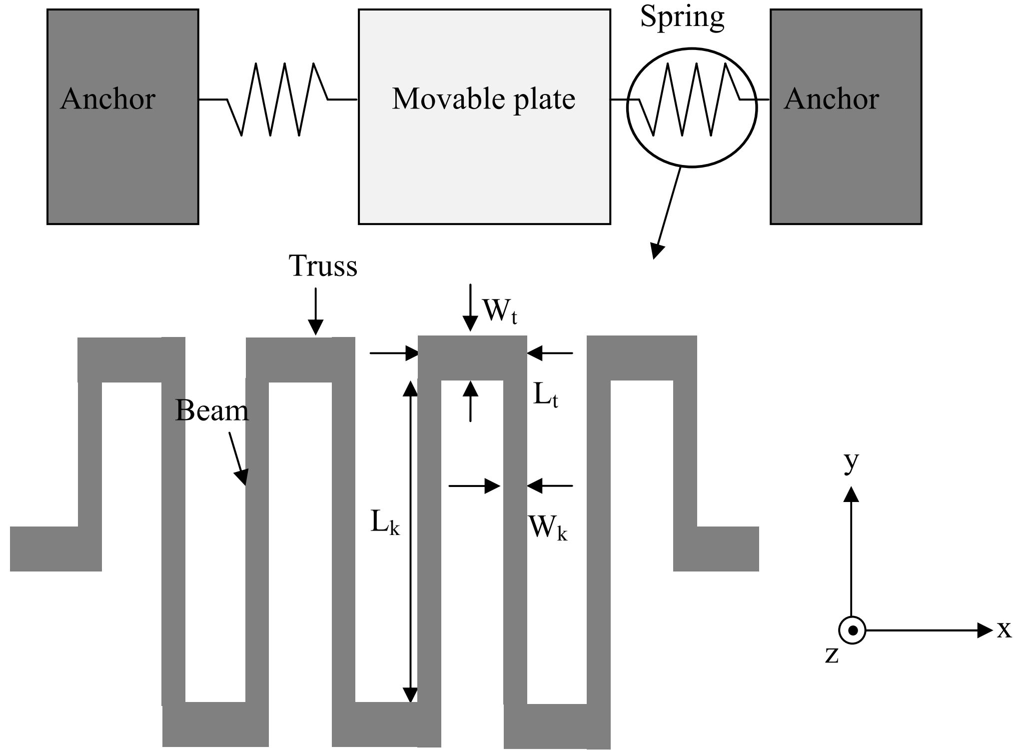

Fig. 2.15 A single element of spring structure

From the schematic of spring, two beams are connected by a truss between the serpentine springs. If the truss is assumed rigid, the spring constants analysis in different direction can be expressed as [33],

$$k_x = \frac{4NEW^3h}{25L^3} \tag{2.20}$$

$$k_y = \frac{NEWh}{7L} \tag{2.21}$$

$$k_z = \frac{4NEWh^3}{25L^3} \tag{2.22}$$

where N is the number of springs in the layout, h is the thickness of springs. E is the Young's modulus of single crystal silicon, L_k and W_k are the length and width of the beams, L_t and W_t are the length and width of the truss.

For a more extensive analysis of folded beam, including the effect of compliant trusses, the spring constant above must be multiplied by a coefficient λ [34]

$$\lambda = \frac{a^2+16as^3+44s^6}{4a^2+34as^3+44s^6}, \tag{2.23}$$

where a is the truss length to beam length ratio (L_t/L_k) and s is the truss width to beam width ratio (W_t/W_k). In our design, L_t=57μm, L_k=1272μm, W_t=40μm, W_k=11μm. The calculated λ is equal to 0.999, which implies that the effect of non-rigid trusses is small. Several issues should be considered. First, the z-axis stiffness k_z and y-axis k_y should be relatively larger than the lateral x-axis stiffness k_x to reduce the out-of-axis motion. The stress in the spring should be smaller than the yield stress of single crystal silicon (7GPa). A safety factor Sf defined as the yield stress divided by the maximum stress on each axis is used to check the spring robustness. The maximum stress due to the lateral maximum displacement x_{max} and static vertical weight loading are given

$$\sigma_x = \frac{12EW_k x_{max}}{25L_k^2}, \tag{2.24}$$

$$\sigma_z = \frac{12mgL_k}{NW_k h^2}, \tag{2.25}$$

As mentioned above, the mass of the movable plate was 36.5 mg, and eight serpentine springs are connected to the movable plate. The total spring constant in the x-direction k_x is 21 N/m, which is far below the other two spring constant (k_y=3.04×10^5 N/m, k_z=8408 N/m). CoventorWare finite element method simulation of a single spring element is shown in Fig. 2.16, which has a spring constant of 2.64 N/m. The results were identical to the design value. The maximum lateral stress is when the maximum displacement is 36.4 μm. The vertical stress is 1.55 MPa, which is so smaller due to the external mass removal on the movable plate. The final devices parameters of the springs are listed in Table 2.2.

1896

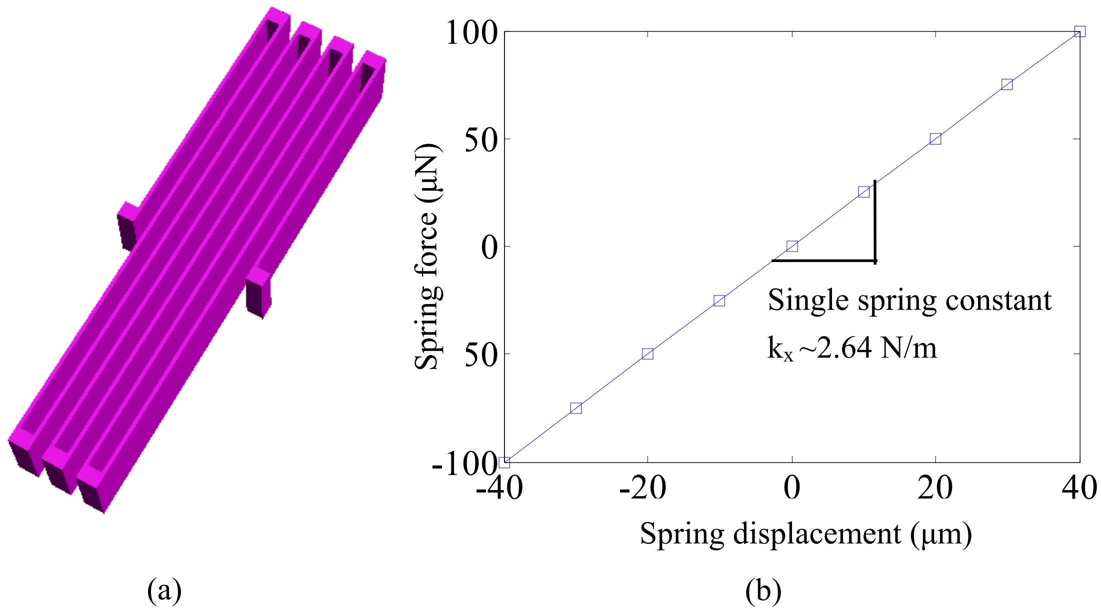

Fig. 2.16 (a) A single spring element (b) single spring constant simulated by CoventorWare

Table 2.2 Spring design parameters

Variable	**Description of variables**	**Designed value**
W_k	Spring Width	11 μm
L_k	Spring Length	1272 μm
k_z	Vertical spring constant	8408 μN/μm
k_x	X-axis spring constant	21 μN/μm
k_y	Y-axis spring constant	3.04×10^5 μN/μm
k_z / k_x	Vertical stiffness ratio	401
k_y / k_x	Lateral stiffness ratio	1.44×10^4
Sf_x	Lateral safety factor	348.69
Sf_z	Vertical safety factor	4512.8

CoventorWare modal simulation of the device is shown in Fig. 2.17. The first mode is the lateral mode in the x-direction (mode 1), which is the primary mode and the frequency of 122 Hz, which is resonant frequency of device. The simulation

results agree well with the design value. Other mode frequencies are the torsion mode (mode 2), lateral mode in y-direction (mode 3), and vertical mode (mode 4), which are at least 3.5 times higher than the primary mode. The separation is large enough to avoid stimulation of these unwanted modes by the input vibration.

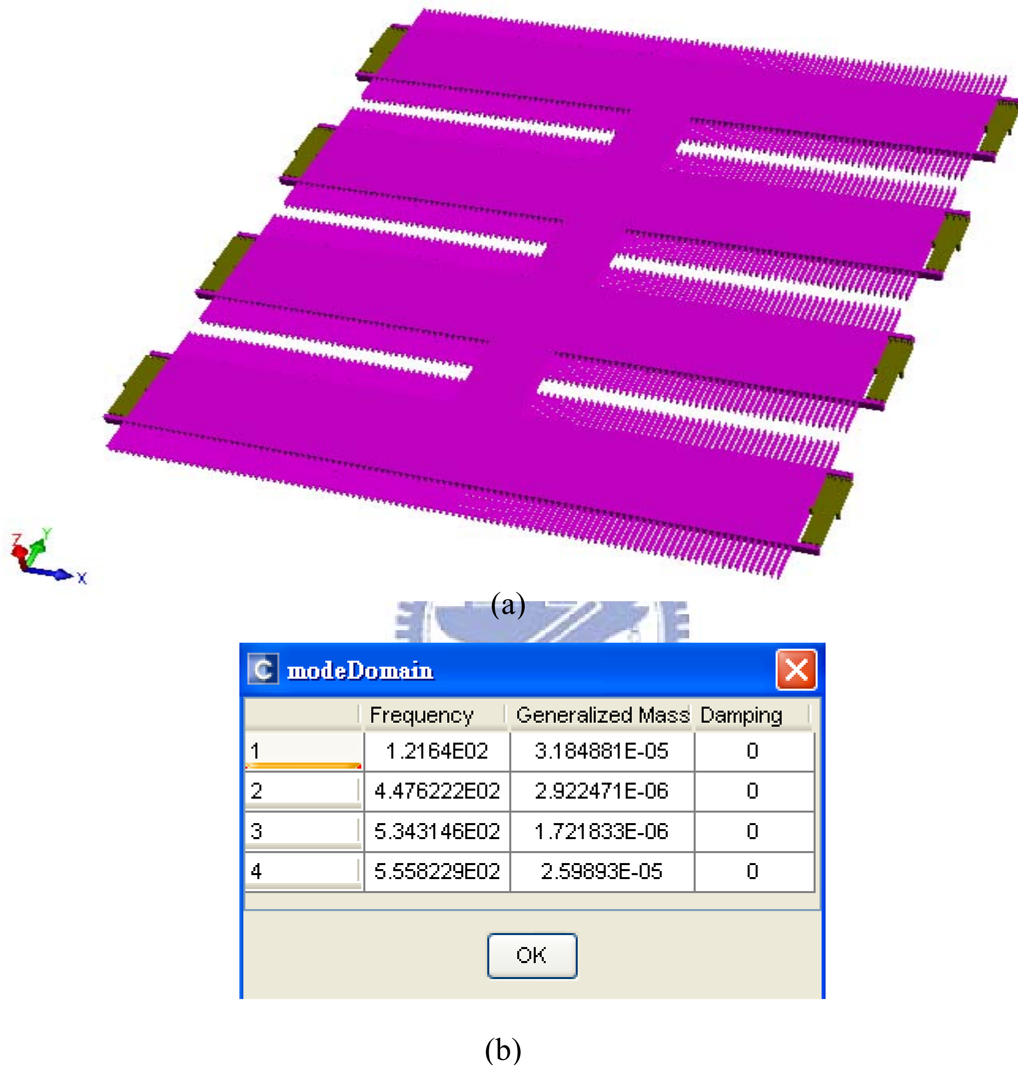

	Frequency	Generalized Mass	Damping
1	1.2164E02	3.184881E-05	0
2	4.476222E02	2.922471E-06	0
3	5.343146E02	1.721833E-06	0
4	5.558229E02	2.59893E-05	0

(a)

(b)

Fig. 2.17 (a) Device solid model (b) CoventorWare modal analysis

2.3.6 Mechanical switch control analysis

The mechanical switches SW1 and SW2 are shown in Fig. 2.3 and Fig.2.4. Traditionally, the switches utilize diodes or clocked active switches [35, 36]. But charge leakage and reverse current issues exists in this circuit. A reverse current should be lower than a few nA in order to prevent charge leakage. However, this is not

common in commercially available diodes and other switching circuitry. Mechanical switches are utilized due to the barely zero charge leakage and lower power consumption. Other advantages are the synchronous operation to the variable capacitor and the monolithic integration with the device structure.

The detail of mechanical switch design was already presented in [27]. This section will discuss the power loss issue during the mechanical switches control process. SW1 is a contact mechanism switch. The variable capacitor charging is realized by SW1 turning on when the comb fingers of the variable capacitor touch. Mechanical switch SW2 is controlled by the pull-in voltage. When the voltage on the capacitor reaches the pull-in voltage, the node B will move to touch node C by electrostatic force, as shown in Fig. 2.5. The pull-in voltage can be determined by the following equation

$$V_{PI} = \frac{2}{3}\sqrt{\frac{2}{3}\frac{k_{s2}d_0^{\,3}}{\varepsilon h L_{SW2}}}, \tag{2.26}$$

where k_{s2} is the SW2 spring constant, d_o is the initial gap between nodes B and D (Fig.2.5), and L is the total overlap length of nodes B and C. The thickness h is the same as the variable capacitor. A number of parameters influence the pull-in voltage. Shown in Fig. 2.18 (a) is the time response of voltage on the variable capacitor and movable fingers displacement. The figure shows the SW2 turn on precisely when the fingers move to the middle position. The output power will fit in with the theoretical value as mentioned above if the device has no leakage current issue. The maximum voltage V_{max} on the variable capacitor is 14 V, which is related to the ratio of maximum and minimum capacitance,

$$V_{max} = \frac{C_{max}}{C_{min}} V_{in}. \tag{2.27}$$

The pull-in effect occurs at one-third of initial gap between the node B and C. Fig.

2.18 (b) has the low pull-in voltage. It shows that the SW2 closes before the fingers moving to the middle position, which is caused by the soften spring constant of SW2. The voltage on the variable capacitor was lower extremely than V_{max} when SW2 closes. It indicates the incomplete energy conversion and means the output power loss. Shown in Fig. 2.18 (c), the voltage on the variable capacitor reaches V_{max} but the SW2 turn on lately. It indicates that the fingers are pulled by a larger restoring force of hard spring. From the simulation result, we can find the relationship between the timing error and power loss, as shown in Fig. 2.19.

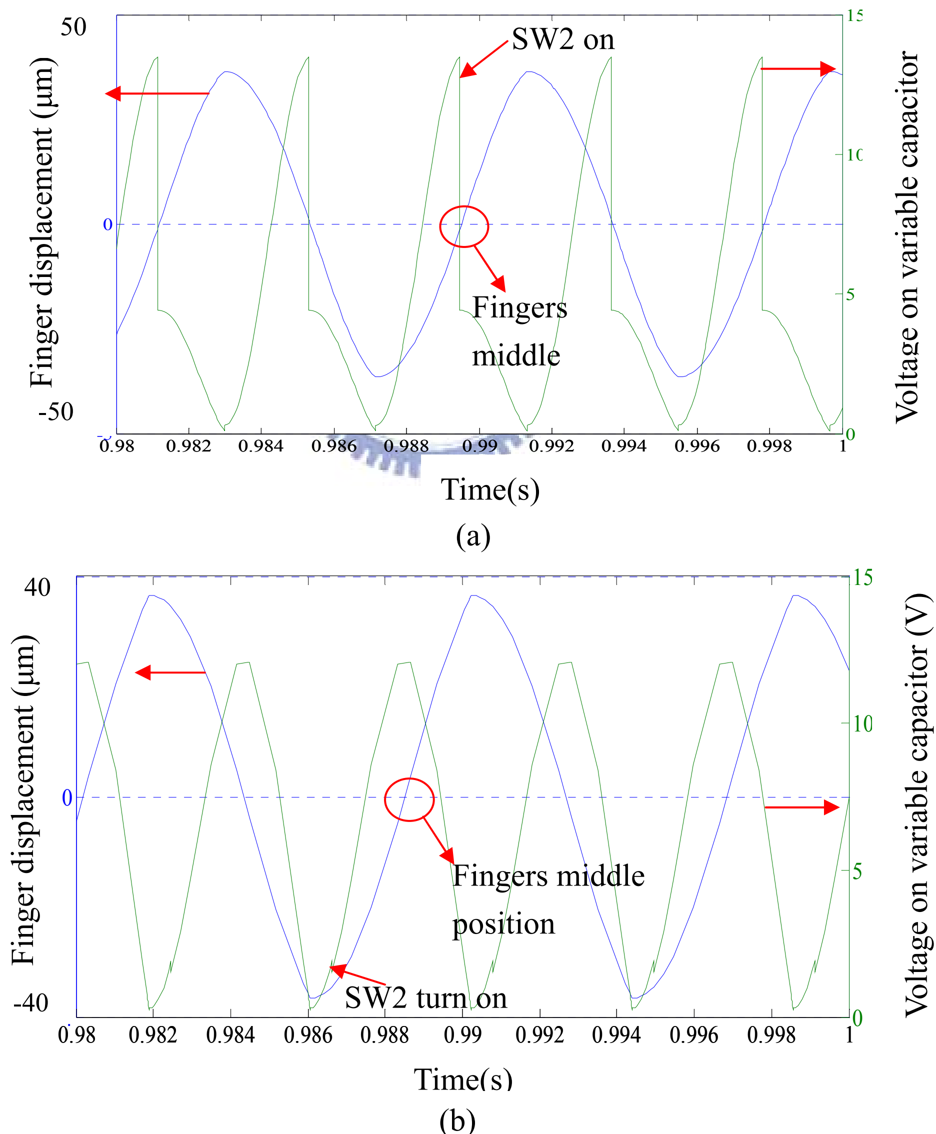

Fig. 2.18 SW2 closes (a) on time (b) early (c) late

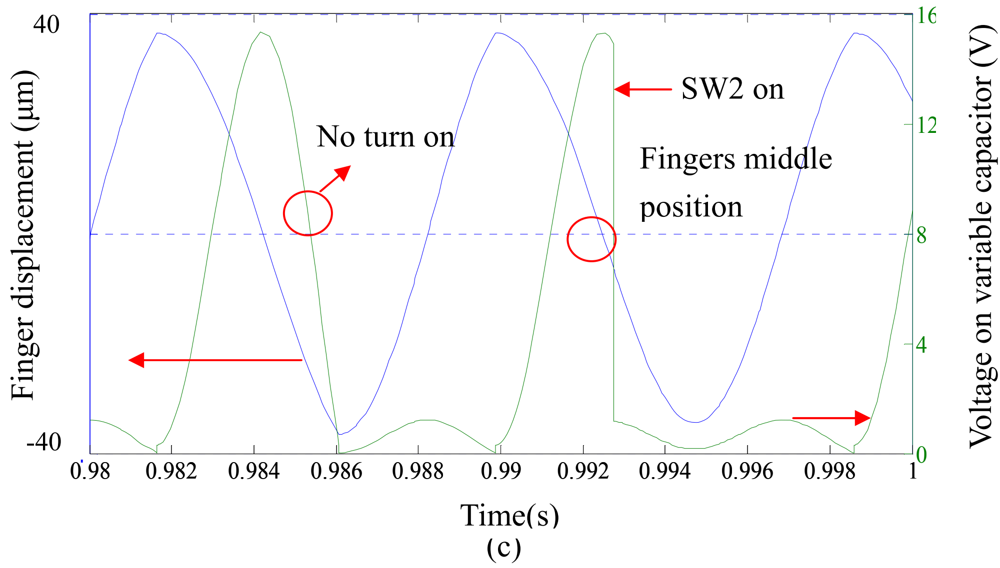

Fig. 2.18 SW2 close (a) on time (b) early (c) late (continued)

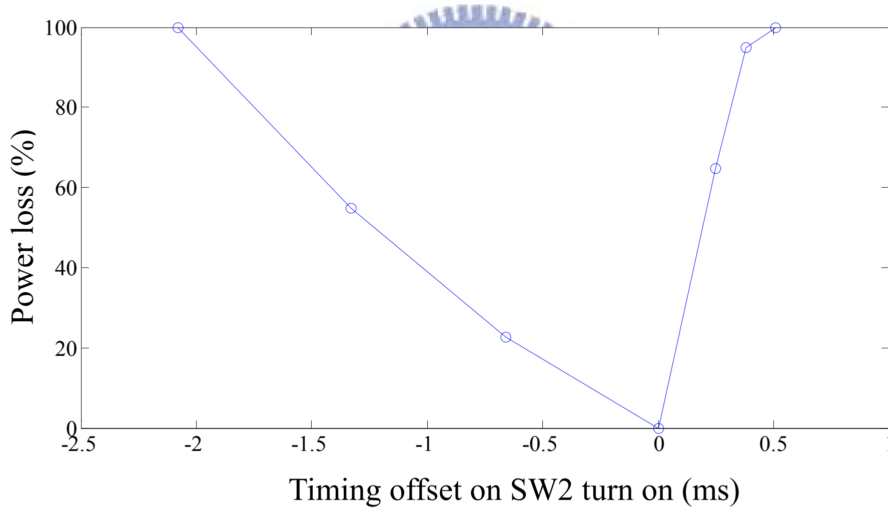

Fig. 2.19 Output power loss versus timing error

2.4 Layout design

The layout of the movable plate was discussed in the last section. This whole schematic was designed with a symmetric configuration to maintain the mass balance and ensure the stable movement in the x-direction during vibration. The minimum center width of movable plate should be larger than 1000 μm to maintain a high rigidness. With the external mass removed, more space in the center was to design the

finger cells to achieve the maximum output power. 8 mechanical springs are connected to the movable plate. The anchored areas of springs are minimized in order to reduce parasitic capacitance. The whole layout is shown in Fig. 2.20. The contact pads will be wire bonded to a printed circuit board for measurement.

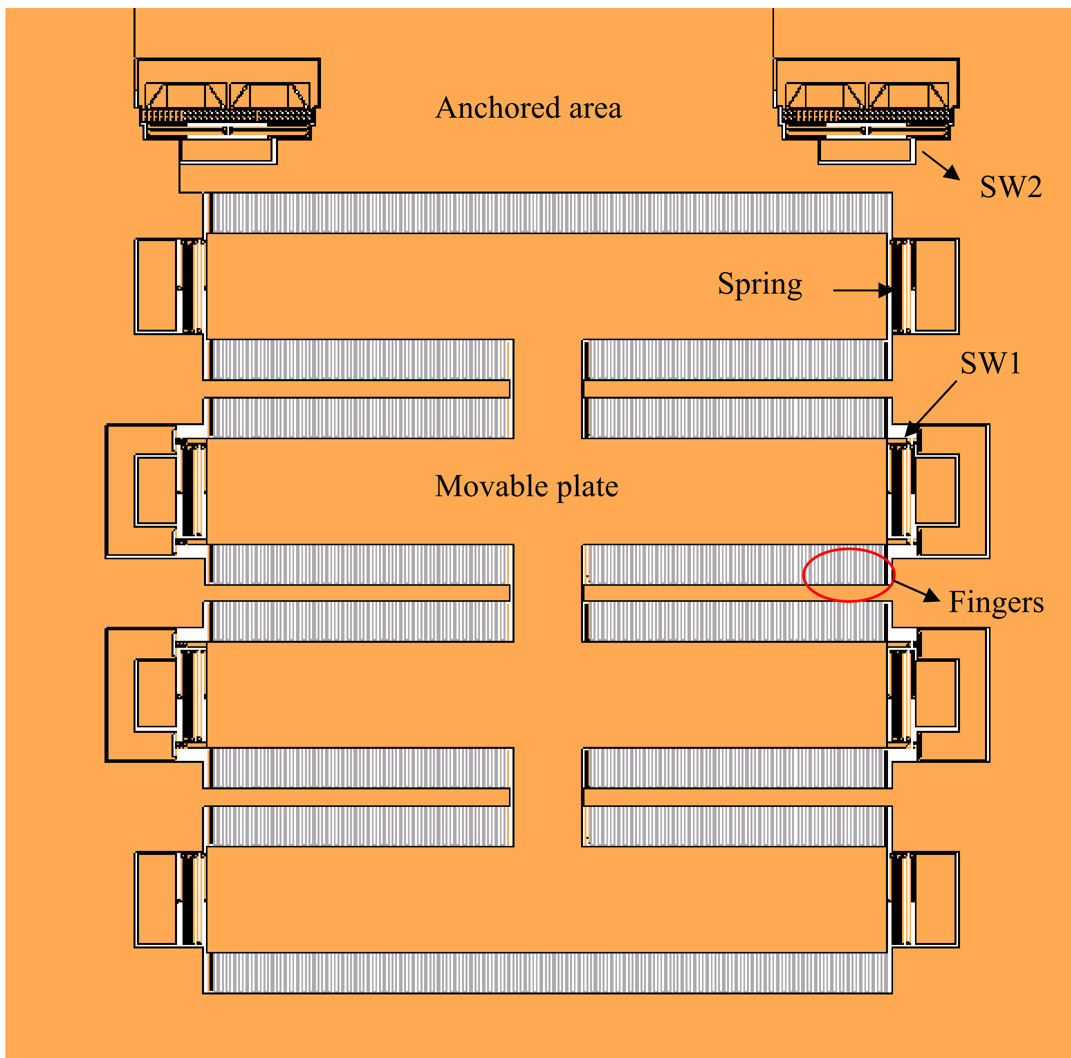

Fig. 2.20 Layout view of the variable capacitor and switches

2.5 Previous design and improvement

The layout of the previous design was shown in Fig. 2.21. The mechanical structure was designed to generate the output power of 31 μW. An external mass of 4 grams was put on the central hole in order to adjust the device resonance to match the input vibration. Two integrated mechanical switches, SW1 and SW2, were used to provide accurate charge-discharge energy conversion timing. Detailed parameter was listed in Table 2.3

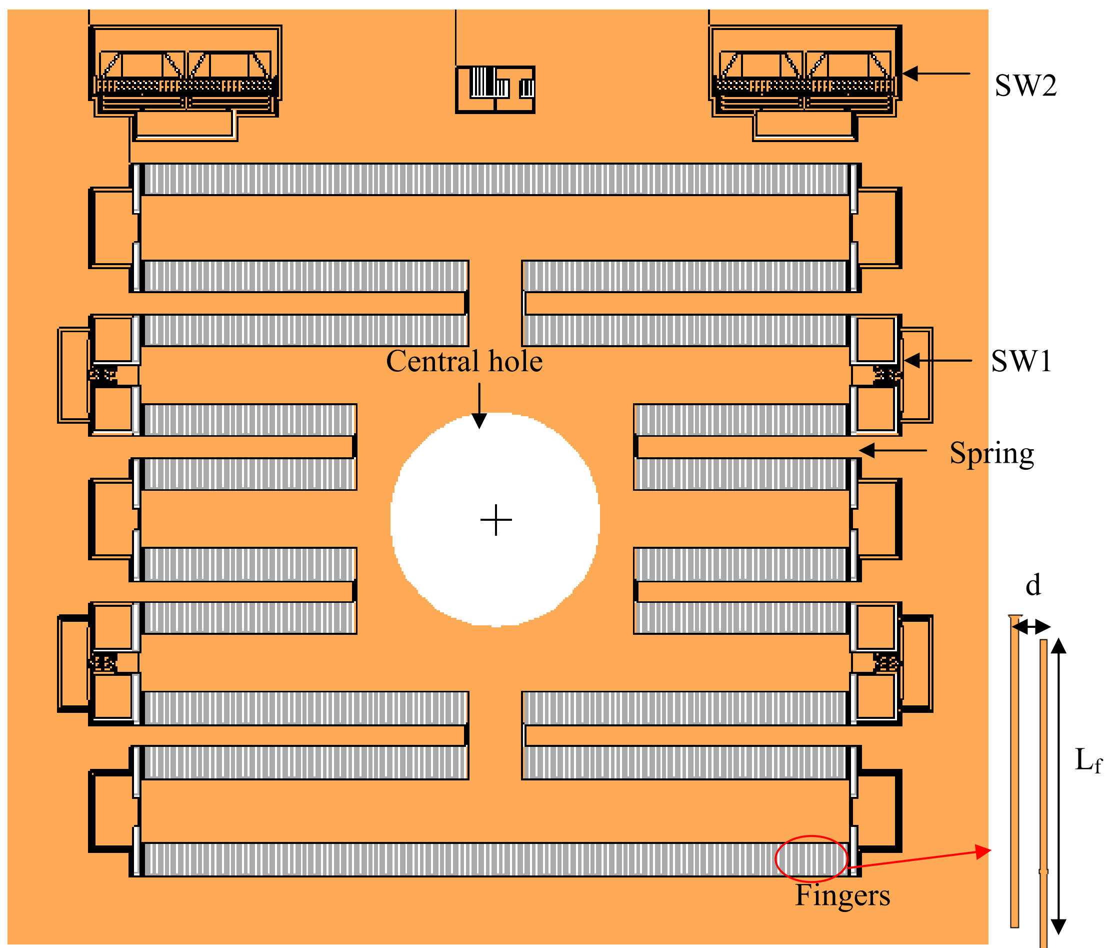

Fig. 2.21 Layout view of the previous device

Table 2.3 Design parameter for previous device

Variable	Description of variables	Designed value
h	Device thickness	200 μm
W_f	Finger width	10 μm
L_f	Finger overlap length	400 μm
d	Finger initial gap	26 μm
t	Silicon nitride sidewall thickness	500 Å
C_{max}	Maximum value of capacitance	1570 pF
C_{min}	Minimum value of capacitance	62 pF
k	Mechanical spring const.	2425 μN/μm
m	Mass of movable plate	4 g
R_L	Driven load resistance	50 MΩ
C_{stor}	Output temporary storage capacitor	5 nF
V_{out}	Output voltage (steady state)	40 V
P_{out}	Output power (steady state)	31 μW

However, the leakage issue was existed in the previous device. The front side of our previous SW1 layout is shown in Fig. 2.22 (a). Guarding walls was used to maintain the same trench width during the ICP etching process. They are removed after releasing process. But the guarding walls may stick on the anchor sidewall during the releasing and then cause leakage issues. Therefore, the guarding walls are replaced, as shown in Fig. 2.22(b). Furthermore, the width of gap was identical to maintain the same etch rate during deep reactive ion etching.

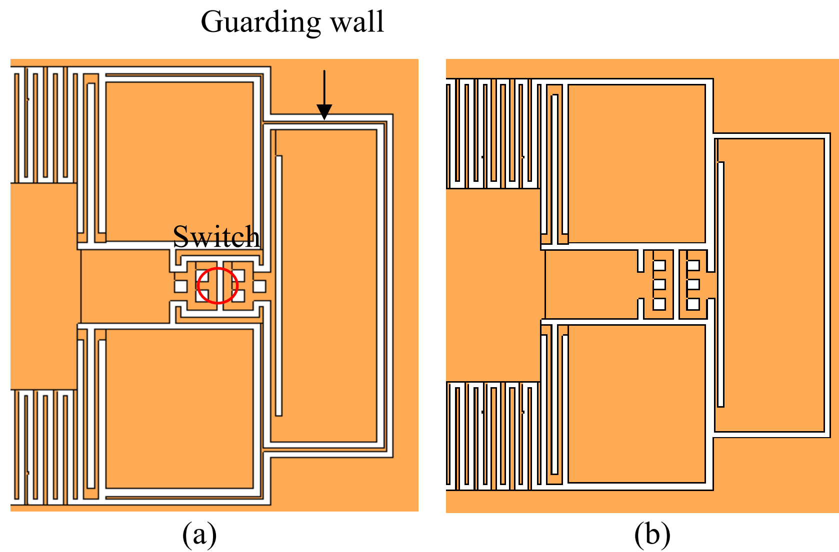

Fig. 2.22 (a) Front side SW1 layout view in our previous design (b) modified design

Second, the overlap region between the movable plate and substrate was considered, as shown in Fig. 2.23. The device was fabricated in SOI wafers with an insulation layer thickness of 2 μm. But parasitic capacitance and leakage resistance are produced during the spring movement in the overlap region. In order to avoid this issue, the substrate area under the movable plate, especially in the spring and switch regions should be reduced. The advantage of the method is to reduce the parasitic capacitance and alleviate the leakage resistance problem. Subsequently the modified device was fabricated in SOI wafer and was discussed in Chapter 3.

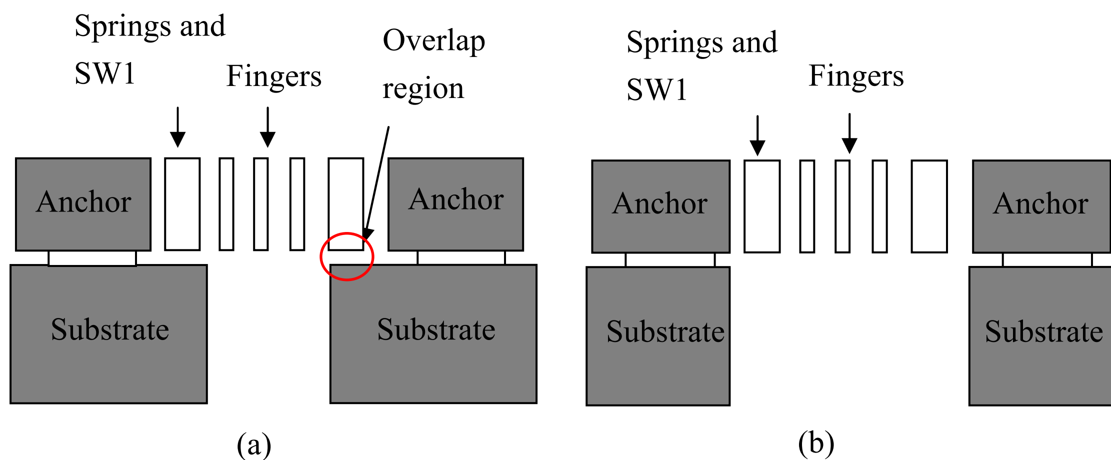

Fig. 2.23 (a) Overlap region between fingers and substrate (b) overlap region removal

2.6 Summary

The design and analysis of a vibration-to-electric energy converter with no external mass attached on the device is presented in this chapter. For the 0.3 V supply voltage and $1cm^2$ chip area constraints, this device can be designed to generate 0.51 μW for the input vibration with frequency of 120 Hz. Compared our previous design with metal ball attachment, the device has the better output power density and alleviate the structure damage caused by the ball during the vibration. Our previous design was modified to avoid the leakage resistance between the device layer and the substrate. Fabrication and measurement results will be discussed in the following chapters

Chapter 3 Fabrication Process

The detail of fabrication process flow and encountered process issues in the SOI (Silicon on Insulator) based device will be presented in this chapter. The first part of this chapter shows the process based on the SOI wafer. The process includes the steps such as wafer cleaning, photolithography, deep reactive ion etching, structure releasing, and metal deposition. The second part will discuss the process issues which were encountered in the experiment. The problems were solved and devices were successfully fabricated.

3.1 Fabrication process flow

As mentioned above, the high aspect ratio MEMS structures for the comb fingers are used as the variable capacitor to convert energy. The structure is fabricated by the deep reactive ion etching technology such as the Inductively Couple Plasma (ICP) etching. The comb fingers are the moving electrodes of the variable capacitor. The outer frame serves as the electrodes of the fixed fingers.

In order to acquire the best output power, the device thickness should be as large as possible. It is limited by the ICP fabrication capability to define the finger structure. The resistive loss was reduced by using a highly conductive device layer with the resistivity less than 0.02 Ω-cm. The buried oxide layer is 2 μm. The handle layer is 400 μm for a firm structural support.

Most of the fabrication was conducted in the Nano Facility Center at National Chiao Tung University. The fabrication process is illustrated in Fig. 3.3 and the detail of the parameters in every process step is presented in the following.

Step 1: Wafer cleaning

The RCA clean is the industry standard for removing contaminants from wafers. It should be performed before high temperature processing steps. The procedure has three major steps in sequence:

A. Organic Clean: Removal of insoluble organic contaminants

B. Oxide Strip: Removal of the thin silicon dioxide layer.

C. Ionic Clean: Removal of ionic and heavy metal atomic contaminants.

The SOI wafer is used in this experiment, as shown in Fig. 3.1(a). Detailed parameters and steps are given as below. Every step begins and ends with 5 minute de-ionized water (DI water) rinse.

Step	Process parameters	Function
1	$H_2SO_4 : H_2O_2 = 3 : 1$ (10 min 85 °C)	Organic removal
2	$HF : H_2O = 1 :100$ (room temperature 30 seconds)	Chemical oxide removal
3	$NH_4OH : H_2O_2 : H_2O = 1 : 4 : 20$ (10 min 85 °C)	Particle removal
4	$HCl : H_2O_2 : H_2O = 1 : 1 : 6$ (10 min 85 °C)	Ion removal
5	$HF : H_2O = 1 :100$ (room temperature 30 seconds)	Chemical oxide removal

Step 2: Silicon oxide deposition on the backside

Silicon oxide was deposited by a BR-2000LL plasma enhanced chemical vapor deposition (PECVD) system on the back of the handle layer of the SOI wafer, as shown in Fig. 3.1(b). The silicon oxide is used as the hard mask for the back side ICP etching process due to the superior heat dissipation in ICP etching and convenience on the double side photolithography. The 4.5 μm silicon oxide was needed according to the selectivity of 100:1 between silicon and silicon oxide in the ICP process. Deposition was divided into several 2.2 μm steps to prevent cracking of oxide layer due to residual stress. Detailed parameters are given as below.

Description	Process parameters
SiH_4 flow rate	5 sccm
N_2O flow rate	90 sccm
Process pressure	400 mTorr
Process temperature	350 °C
RF power	11 W
Deposition rate	35 minutes resulting in 2.2 μm (repeat 2 times)

Step 3: Back side photolithography on silicon oxide

The back side photolithography was performed by EV620 aligner on the silicon oxide deposited in the last step, as shown in Fig. 3.1 (c). The photoresist was AZ4620 due to its available thickness in the spin coater. The thickness of AZ4620 was 7 μm according to the selectivity between AZ4620 and oxide in the buried oxide etchant (BOE). Detail parameters are given as below.

Step	Description	Process parameters
1	HMDS coating	150 °C 30 minutes
2	1st spin (spread cycle)	500 rpm 10 seconds
3	2nd spin (spin cycle)	2000 rpm 40 seconds
4	Static settlement	10 minutes
5	Soft bake	90 °C 12 minutes
6	Exposure	20 seconds
7	Development	80 seconds
8	DI water Rinsing	90 seconds
9	Hard bake	120 °C at least 1 hour

Step 4: Wet etching on the back side

This step is shown in Fig. 3.1(d). The silicon oxide below the photoresist was etched by a buffered oxide etchant (NH_4F: HF=6:1) with an etch rate of 1 μm per minute roughly. BOE solution is used due to the relatively low selectivity between

silicon oxide and photoresist in the RIE process. The undercutting effect of wet etching is irrelevant to cause the back side pattern for partial substrate removal. The samples can be immersed into DI water to dilute BOE solvent, which can protect the photoresist mask to avoid the BOE attack and alleviate the peeling off of the photoresist mask problem. Moreover, the photoresist mask also can be hard baked for at least 1 hour before the wet etching.

Step 5: Front side photolithography

The front side photolithography was performed by an EV620 double side aligner to define the photoresist mask, as shown in Fig. 3.1(e). The subsequent ICP etching is the primary process to define the device structure. In order to protect the structure in the device layer, the front side photolithography is performed after the back side process. The photoresist thickness is 5 μm because the minimum selectivity of ICP etching between silicon and AZ4620 photoresist is 40:1. Hard bake should be as long as possible to withstand the ICP etching. Detailed parameters are given as below.

Step	Description	Process parameters
1	HMDS coating	150 °C 30 minutes
2	1st spin (spread cycle)	500 rpm 10 seconds
3	2nd spin (spin cycle)	4000 rpm 40 seconds
4	Static settlement	10 minutes
5	Soft bake	90 °C 7 minutes
6	Exposure	11 seconds
7	Development	60 seconds
8	DI water Rinsing	90 seconds
9	Hard bake	120 °C at least 1 hour

Step 6: Deep reactive ion etching of the front side

The silicon structure in the device layer is defined by ICP etching which is performed by using a STS MESC multiplex ICP reactor with standard Bosch process, as shown in Fig. 3.1(f). By applying the etching and passivation parameters, it can provide a better etching profile. The detail was discussed later. In order to maintain the uniform etch rate and acquire the better heat dissipation, maximum helium leak rate should be limited. The averaged etch rate is roughly 2 μm per minute. Detailed parameters are given as below.

Description	Etch phase parameters	Passivation phase parameters
Time per cycle	11.5 seconds	7.0 seconds
SF_6 flow rate	130 sccm	0 sccm
C_4F_8 flow rate	0 sccm	85 sccm
O_2 flow rate	13 sccm	0 sccm
Coil RF power	600 W	600 W
Platen RF power	11.5 W	0 W
Process pressure	APC position = 81.2 % Base pressure = 0.3 mTorr	
Helium back side cooling	Helium back side pressure = 10 Torr Maximum helium leak up rate = 20 mTorr/min	
Etch rate	0.6-0.7 μm per cycle depending on pattern	

Step 7: Wafer dicing

Wafer dicing must be performed before the back side deep silicon etching. The reason is that the entire wafer becomes very fragile and may disintegrate in the reactor chamber when a large area of the back side silicon is removed. The other problem is that the residual stress in the buried oxide can damage the structures in the front side layer. Therefore, the wafer is diced first by a Disco 2H/6T system. The device layer structures are protected during the dicing process by AZ4620 photoresist. The detailed

parameters of the protection photoresist coating are given as below. The subsequent back side etching will be conducted with the individual chips bonded to a carrier wafer by heat dissipation paste.

Step	Description	Process parameters
1	Removed the photoresist mask	A.C.E or H_2SO_4 to remove
2	1st spin (spread cycle)	500 rpm 10 seconds
3	2nd spin (spin cycle)	1800 rpm 40 seconds
4	Soft bake	20 minutes

Step 8: Back side deep reactive ion etching

The wafer was diced as shown in the previous step. Diced chips were bonded on a handle wafer. In order to prevent the rupture of the handle wafer, silicon oxide or AZ4620 should be deposited on the handle wafer to avoid the plasma attacking during the ICP process before the chip bonding. The process of the back side ICP etching was shown in Fig. 3.1 (g). Heat dissipation issue was encountered due to poor helium cooling capability on the bonded chip. Moreover, the bonded chips in ICP etching process will spoil the selectivity and vertical profiles due to the helium capability degrade. Fortunately, the back side structure is rather insensitive to or even benefiting from non vertical etching profiles. Detail process parameters are identical to the front side ICP process.

Step 9: HF Releasing

The device chip is released by 49 % HF to remove the unwanted buried oxide and the blocking structure on the handle layer. The process is shown in Fig. 3.1 (h). HF vapor also can release the device but has poor selectivity than solution. The release time is about 20 min and the oxide layer is over etched in order to prevent

leakage during metal deposition. Finally, the device is cleaned by rinsing in isopropanol (IPA) and then hot baked after the release is finished. DI water cannot be used to clean to avoid the stiction between the comb fingers in the release process.

Step 10: Silicon nitride deposition

As shown in Fig. 3.1 (i), silicon nitride is treated as the dielectric layer which was deposited by plasma-enhanced chemical vapor deposition (PECVD). HF releasing process is prior to this step due to poor selectivity between the silicon nitride and HF solution. A 2500 Å thick silicon nitride thickness was deposited on the top and bottom sides of the release chip. The sidewall nitride was expected as 500 Å because of poor step coverage in the PECVD process. Detailed parameters are given as below.

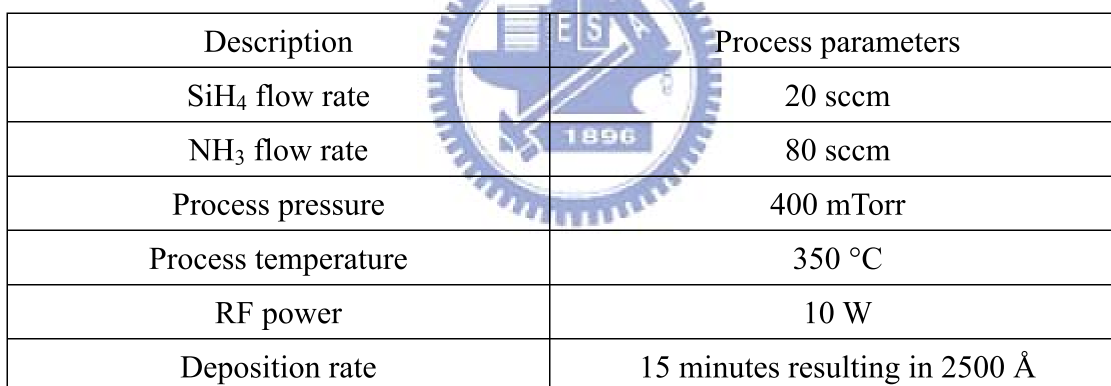

Description	Process parameters
SiH_4 flow rate	20 sccm
NH_3 flow rate	80 sccm
Process pressure	400 mTorr
Process temperature	350 °C
RF power	10 W
Deposition rate	15 minutes resulting in 2500 Å

Step 11: Silicon nitride removal in anchor area

After the silicon nitride was deposited, the top side silicon nitride layer on the anchor area should be removed by a SAMCO RIE-10N RIE in order to provide the electrical contact to the silicon device, as shown in Fig. 3.1 (j). To prevent the leakage between the fingers, the silicon nitride deposited on the top side of the comb finger cannot be removed. With the shadow mask A in Fig. 3.1 (j), the silicon nitride is protected in the RIE process. Detail parameters are given as below.

Description	Process parameters
SF_6 flow rate	30 sccm
CHF_3 flow rate	10 sccm
Helium back side cooling	15 sccm
Process pressure	50 mTorr
RF power	100 W
Etch rate	1000 Å per minute

Step 12: Metal deposition

As shown in Fig. 3.1(k), aluminum is deposited on the contact pads and the lateral contacts in the mechanical switches. Sputtering is used due to the better step coverage on the switch contacts. With the shadow mask B in Fig. 3.1 (k), aluminum is only applied to the contact pad and switch gap areas to prevent the leakage.

Step 13: Wire bonding and external mass attachment

The last two steps are to wire bond the contact pads to a PCB and then attach the external tungsten ball to the center hole for further vibration test, as shown in Fig. 3.1 (l). The chip is attached on the PCB board with silver glue before wire bonding. The ball has a mass of 4 grams and attached by epoxy. The care must be taken in this step or the device may be destroyed.

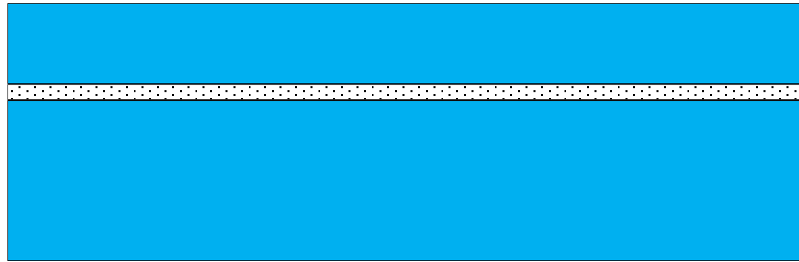

(a) RCA cleaning (Step 1)

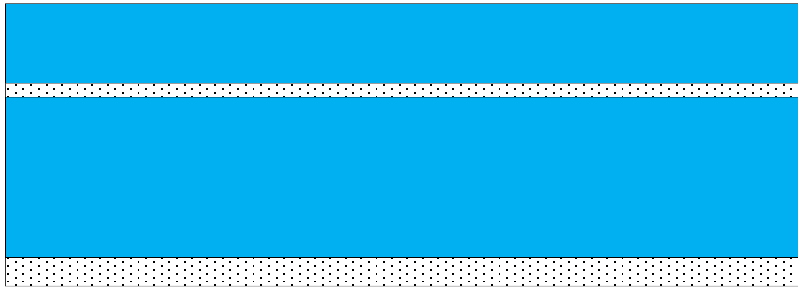

(b) PECVD silicon oxide deposition on the back side (Step 2)

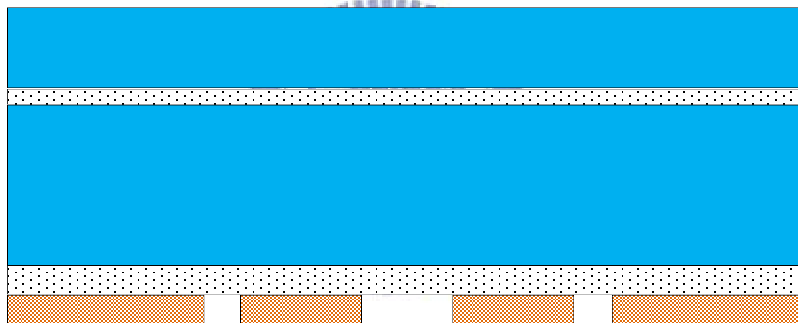

(c) Silicon oxide patterning by photoresist (Step 3)

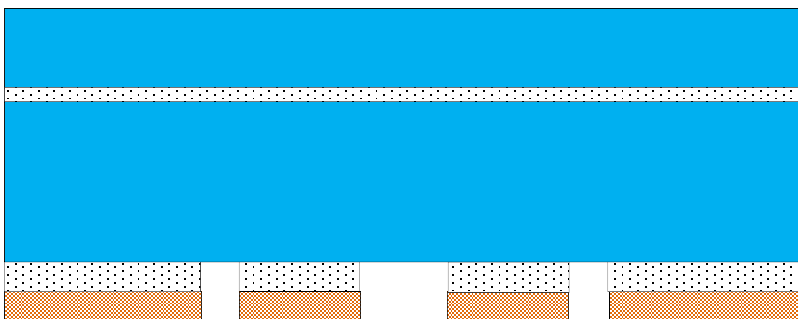

(d) Silicon oxide hard mask etching by BOE (Step 4)

Fig. 3.1 Fabrication process flow of the SOI device

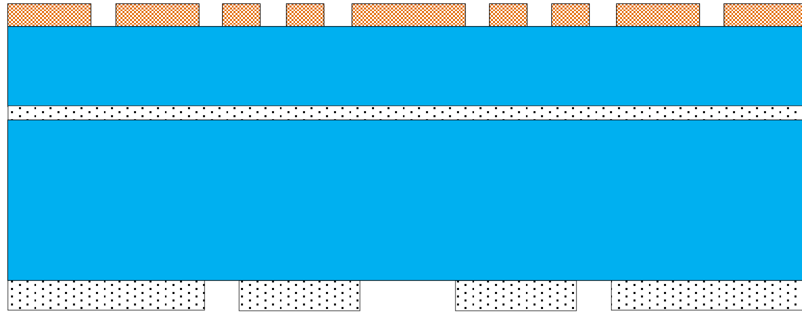

(e) Front side photoresist patterned by double side photolithography (Step 5)

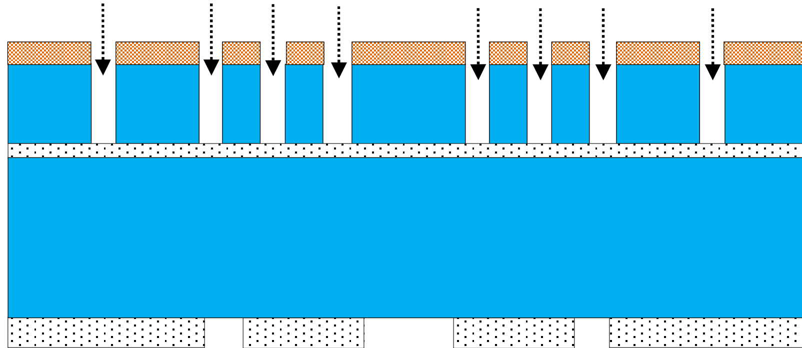

(f) ICP deep silicon etching on the front side (Step 6)

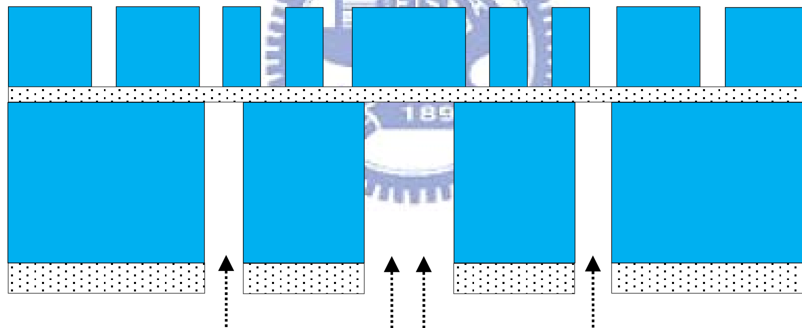

(g) Back side ICP deep silicon etching (Step 8)

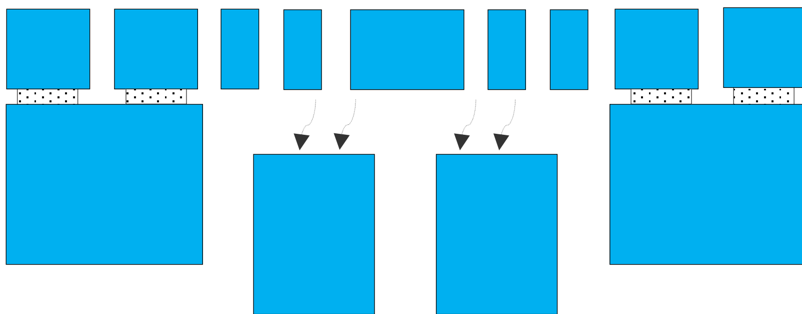

(h) Release in HF solution (Step 9)

Fig. 3.1 Fabrication process flow of the SOI device (continued)

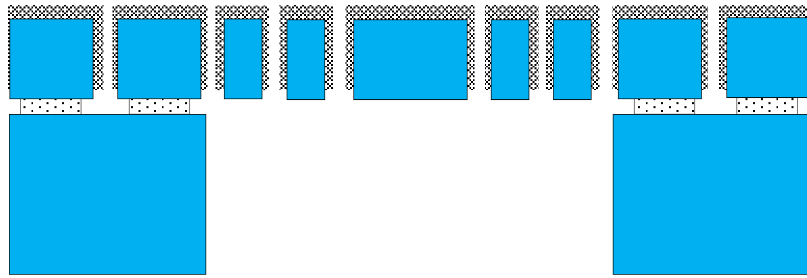

(i) Silicon nitride deposited by PECVD (Step 10)

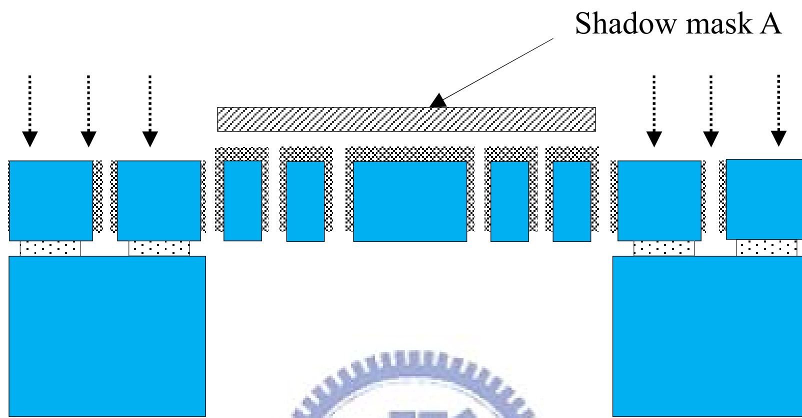

(j) Top side silicon nitride removal by RIE with shadow mask A (Step 11)

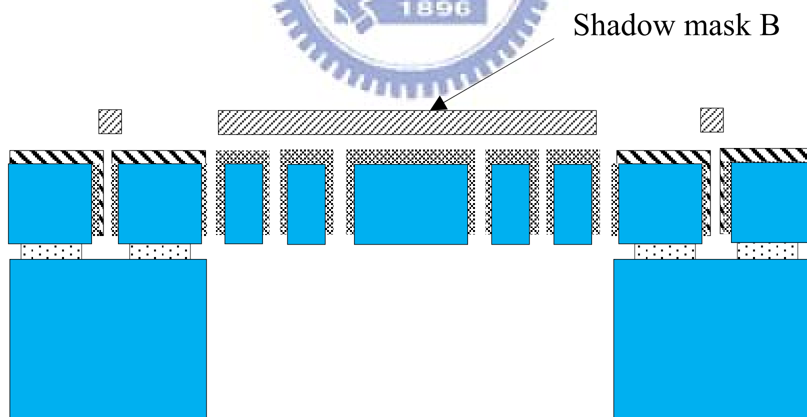

(k) Metal deposition by sputtering with shadow mask B (Step 12)

Fig. 3.1 Fabrication process flow of the SOI device (continued)

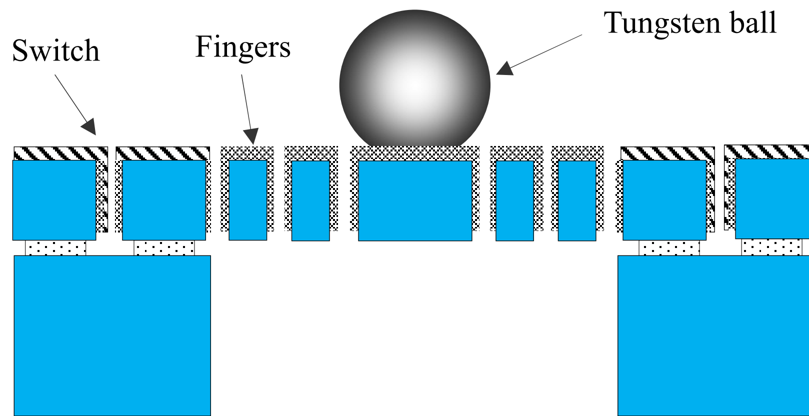

(l) Wire bonding and tungsten ball attachment (Step 13)

Fig. 3.1 Fabrication process flow on the SOI device (continued)

3.2 Processing issues and solution

Several problems and issues were encountered in the fabrication process. Most of issues or problems are related to the ICP etching process. Other issues are leakage issues due to incomplete isolation layer deposition. Solutions are proposed and demonstrated in this section.

3.2.1 Non ideal effects of the ICP process

Non ideal effects exist in the ICP process due to experiment inaccuracy. The effects include notching, loading effect, and grass formation etc. The detail process will be shown in the following.

Notching effect

Deep reactive ion etching through the silicon device layer is an essential step in microstructure fabrication. However, plasma etching the silicon over an insulator layer has a silicon notching problem at the silicon/insulator interface. The

phenomenon was shown in Fig. 3.2 [37]. The positive charge accumulation in the isolation layer causes further deflection of reactant ion and forwarding scattering. The poor profile caused by the notching may result in degraded performances. As this undercutting is aspect ratio dependent, the profiles and the characteristics of the final devices may further vary across the wafer, affecting the repeatability and reliability, especially for the thick device wafer.

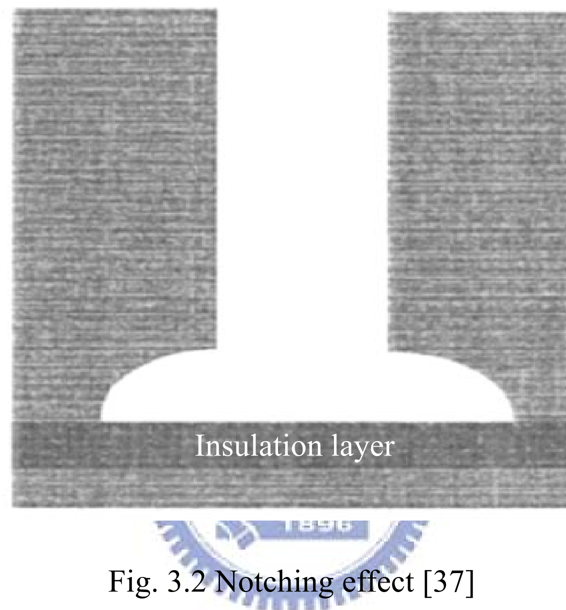

Fig. 3.2 Notching effect [37]

The problem was encountered in our device structure, as shown in Fig. 3.3 (a). The bottom of the comb finger was over etched due to the plasma bombarding on the interface between silicon and oxide layer. Therefore, the deep ion etching was divided into two steps to prevent the silicon over etching. First, the etch rate of the deep silicon etching should be controlled accurately. Thus, the comb fingers should be etched a little thickness to estimate the etch rate and subsequently performed remainder thickness. The better profile of comb fingers was shown in Fig. 3.3 (b)

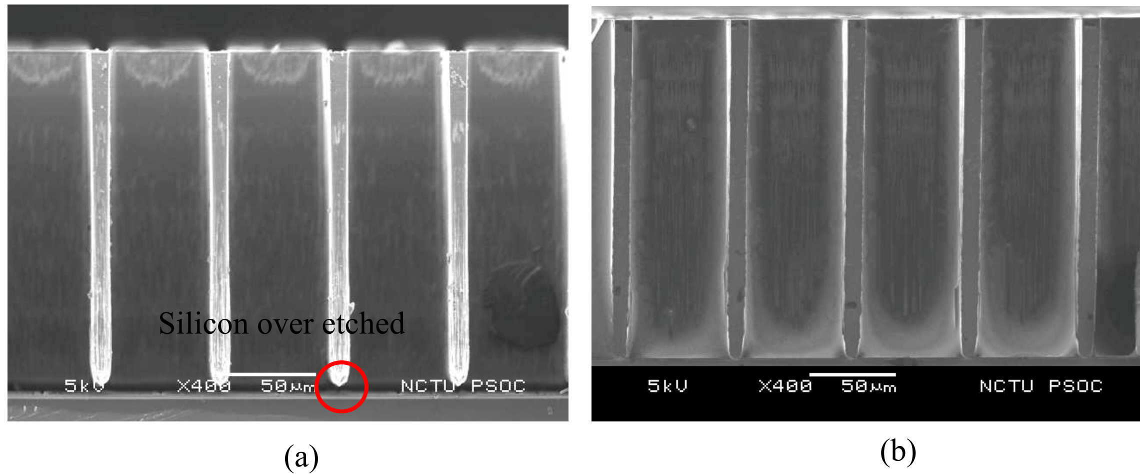

(a) (b)

Fig. 3.3 (a) Notching occurred on the fingers bottom side, (b) improvement result

Loading effect

The loading effect is an important issue for the ICP etching process. This effect indicates that the etch rate will be severely reduced when the number of chip and percentage of the open area is too large [38]. It also happens in our device during the back side ICP etching. As mentioned above, the etch rate in the ICP process is 0.6 μm per cycle with the six chips but is about 0.56 μm with ten chips bonded on the carrier wafer. The open area is proportional to the number of chips bonded on the wafer. More chips on the handle wafer also cause poor heat dissipation and reduce the etch rate of silicon.

Grass formation

The other issue is the grass formation in the ICP process. The basic process of ICP etching can be divided into two major steps. The first step is a sidewall passivation step to achieve a straight sidewall feature with the polymer gas (C_4F_8) and the second step is silicon etching by etching gas (SF_6). The periodic change of gases for etching (SF_6) and passivation (C_4F_8) can lead to very high aspect ratios and very high etch rates.

However, ICP etching has its own specific problems, which include “grass” formation, due to non-uniform etching [39]. To solve this problem, we decrease the C_4F_8 flow time (passivation time) from 10 s to 7 s and SF_6 etching time is not changed. The experiment results are shown in Fig. 3.4. The sidewall of the finger with decreased C_4F_8 gas flow time is changing dramatically. A major problem during etching silicon is the forming of “grass” on the surface. As a result of particulate material inadvertently deposited on the silicon surface, the material can locally mask the silicon during etching. This material can be formed during etching due to redeposition and growing of polymer material from the sidewall passivation step. By decreasing the cycle time of C_4F_8, the grass formation was remarkably decreased

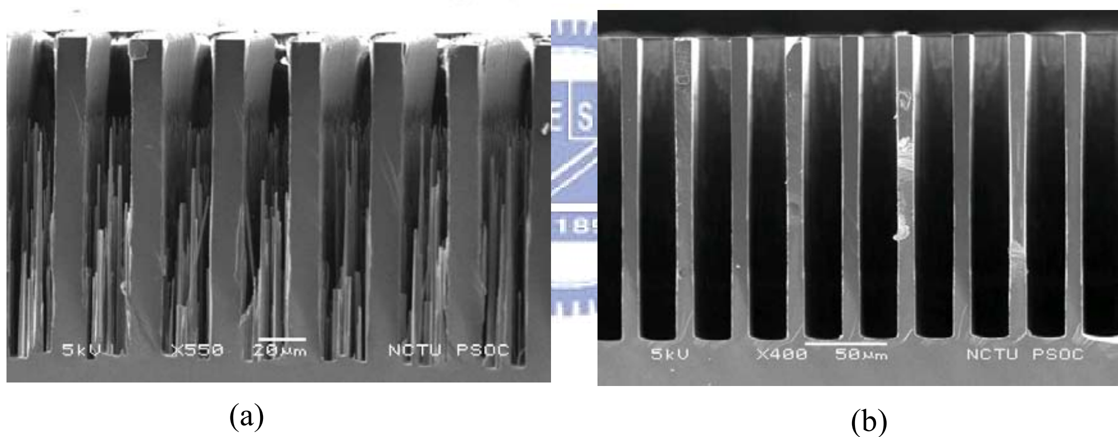

(a) (b)

Fig. 3.4 SEM photo with different C_4F_8 flow time (a) SF_6: C_4F_8 = 11s:10s (b) SF_6: C_4F_8 = 11s:7s

Sidewall flatness

The results of ICP process will influence the silicon nitride deposition and electrical measurement. The experiment results in the ICP etching is shown in Fig. 3.5. The polymer adhered on the sidewall of the finger is produced by the passivation gas in the ICP process.

Therefore, two solutions are proposed in the following. One is to adjust the fabrication parameters, such as the ratio of etching and passivation time or the RF power, to prevent formation of more polymers. But the etch rate of silicon are dependent on these fabrication parameters. The other is cleaning by chemical solution, such as NH_3 solution (NH_4OH: H_2O_2: H_2O = 1: 4: 20). As mentioned in section 3.1, NH_3 solution can remove unwanted particles and ensure the silicon surface not to be etched. But the finger structure fragility was taken into account when the device was immersed in the solution which heated to the temperature of 85°C. Fortunately, the device cleaned by NH_3 solution was all right and the polymer was removed, as shown in Fig. 3.5 (b).

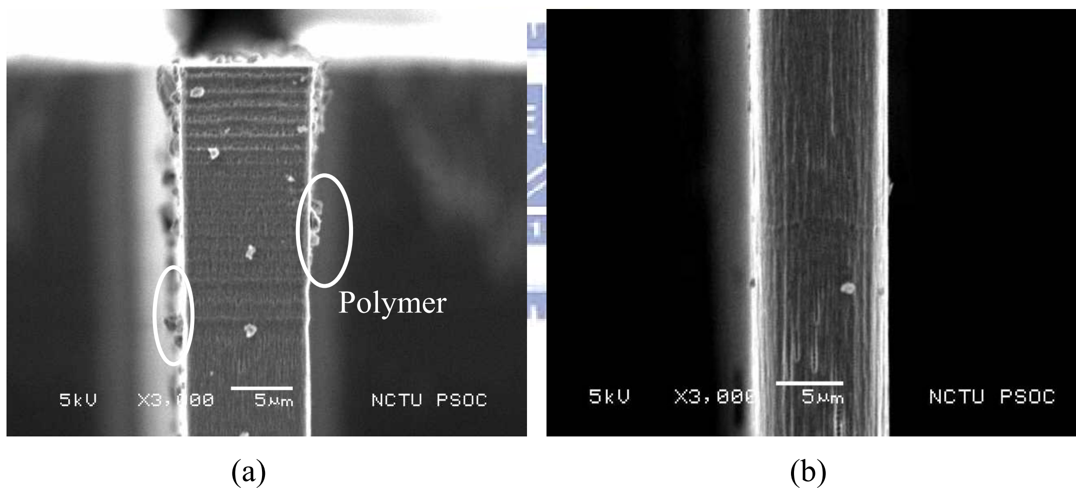

Fig. 3.5 (a) Polymer produced in the ICP etching (b) polymer removal by NH3 solution

Plasma permeate problem

This problem occurred on the back side ICP etching process. As mentioned above, the diced chip had to be bonded on the carrier wafer with the heat dissipation glue. The plasma may permeate through the interface between the front side and the surface of the carrier wafer if the heat dissipation glue did not cover completely the edge of the diced chip. The results are shown in Fig. 3.6.

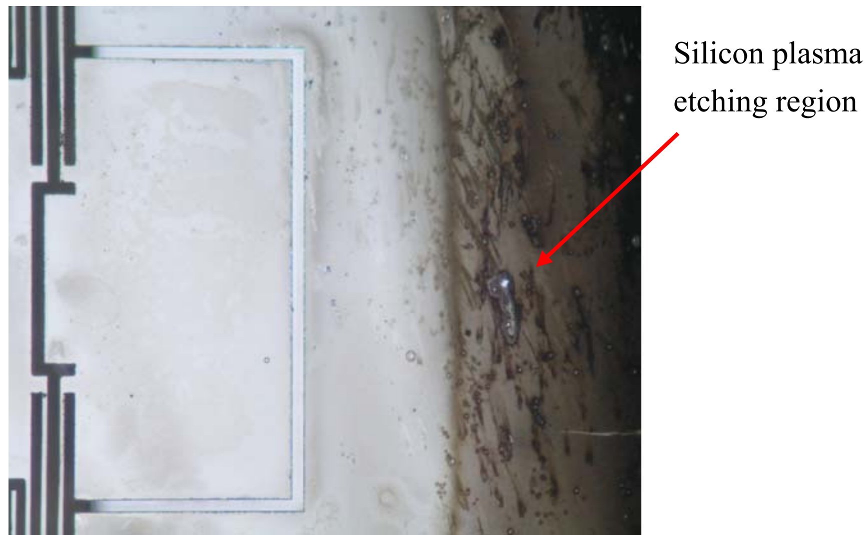

Fig. 3.6 Experiment results in the plasma permeate on the front side

3.2.2 Silicon nitride deposition

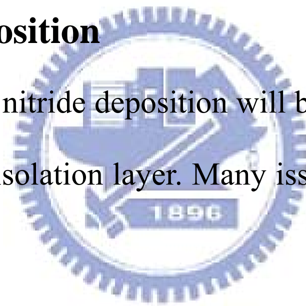

In this section the silicon nitride deposition will be discussed. Silicon nitride also is regarded as the material of isolation layer. Many issues should be considered in the deposition process.

Leakage problem

As mentioned above, silicon nitride removed by HF solution can lead to leakage between the fingers. Thus silicon nitride was deposited by plasma enhance chemical vapor deposition (PECVD) after the HF releasing. PECVD technology has the homogenous film, which is coated with minimum thermal stress. However, the technology suffers from poor step coverage on the sidewalls and the bottom corners, as shown in Fig. 3.7. This result causes leakage if the variable capacitor fingers were touched. In addition, particles were produced to influence the deposition quality in the PECVD process [40]. Therefore, LPCVD nitride deposition will be adopted due to the better step coverage.

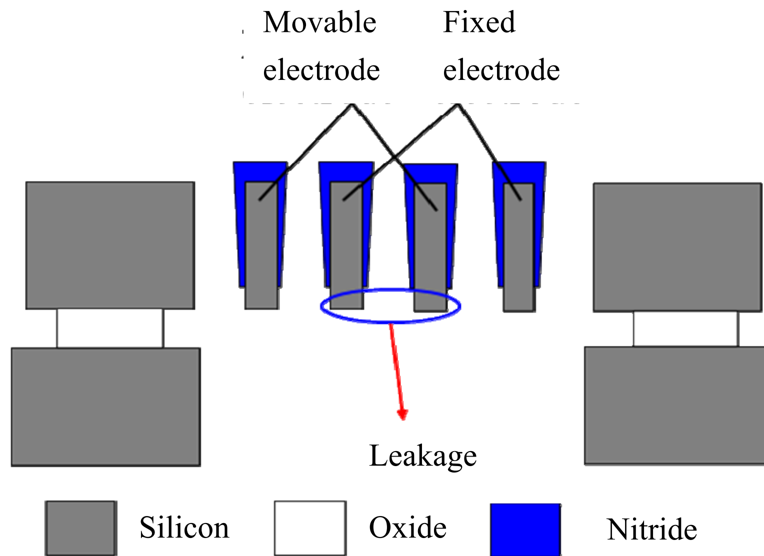

Fig. 3.7 Schematic of poor step coverage

Residue stress for LPCVD nitride layer

Residue stress during the deposition is an important issue. The properties of the LPCVD and PECVD nitride are listed in table 3.1. [41]. The thickness of LPCVD nitride should be considered or else the residue stress was encountered in the thin film deposition process. This issue will leads to the structure deformation or lifetime reduction. According to Table 3.1 and Eq. 3.1 [42], the yield stress of LPCVD nitride is 1000 MPa so that the thickness of LPCVD nitride cannot exceed more than 3000 Å for a 4-inch diameter and substrate thickness of 200 μm SOI wafer.

$$\sigma_{\mathrm{f}} = \frac{E_{\mathrm{s}} t_{\mathrm{s}}^{2}}{3(1-v_{\mathrm{s}}) t_{\mathrm{f}}} \frac{\delta}{\rho} \tag{3.1}$$

σ_{f} : residue stress of nitride on substrate

$E/(1-v_{\mathrm{s}})$: residue stress of substrate

t_{s} : thickness of substrate

t_{f} : thickness of silicon nitride

ρ : radium of substrate

δ : curvature difference before and after deposition

Table 3.1 The thin film property of LPCVD and PECVD nitride [41]

Deposition type	LPCVD	PECVD
Typical temperature(^{o}C)	750~850	250~350
Density (g/cm^3)	2.9 to 3.1	2.4 to 2.8
Resistivity(Ω.cm)	10^{16}	10^{6} to 10^{15}
Dielectric strength (10^6 V/cm)	10	5
Stress (M Pa)	1000 (tens.)	200(comp.) to 500 (tens.)

3.2.3 Metal deposition issues

Aluminum is used for the electrode contact pad. However, electrical leakage existed after metallization due to the metal connection at the bottom of gap between the anchors after aluminum deposition. Therefore, an accurately aligned shadow mask was employed to limit the metal deposition only on the contact pads. The experiment result was shown in Fig. 3.8. The deposition region was separated to avoid leakage. The shadow mask was made of silicon and the open areas are defined by photolithography and ICP etching processes.

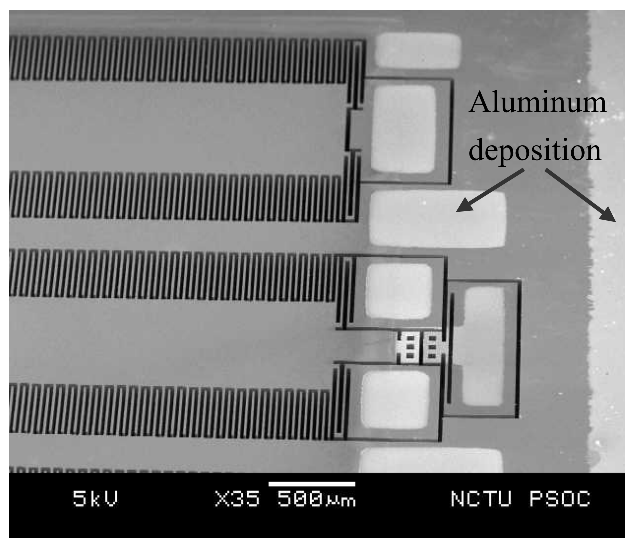

Fig. 3.8 Aluminum deposition by shadow mask

3.3 Fabricated device

The scanning electron microscope (SEM) photograph of the fabricated device with the fingers and center hole is shown in Fig. 3.9. The center of hole is used to put the external ball to adjust the mechanical resonant frequency to achieve the design specification.

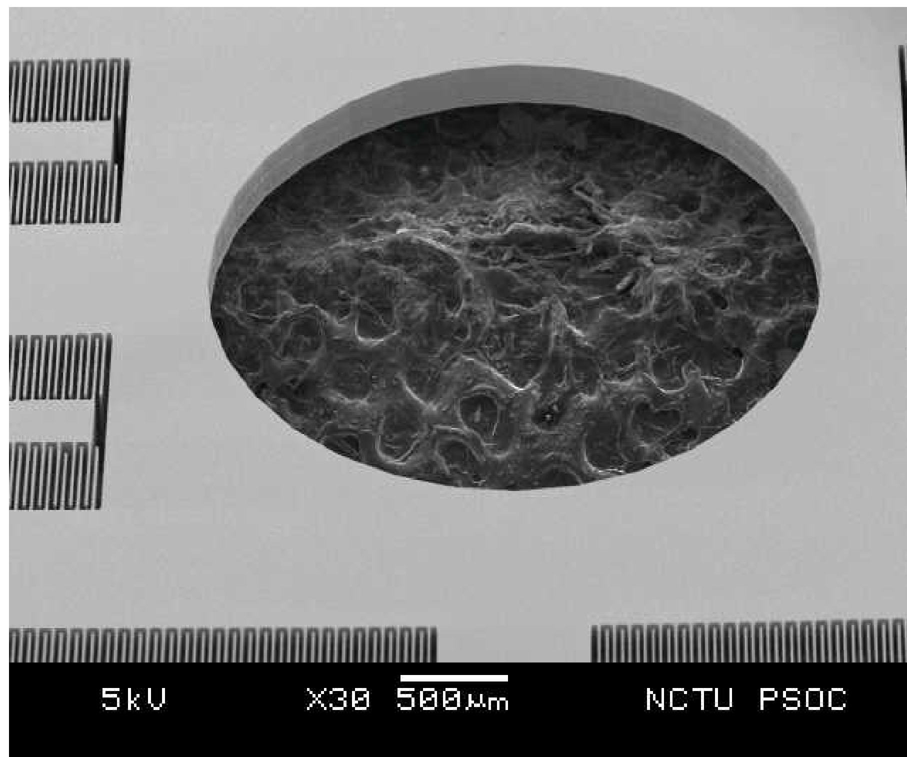

Fig. 3.9 Center hole of the fabricated device

The corner of the device has mechanical switches and serpentine spring, as shown in Fig. 3.10 (a). The close-up view of spring is shown in Fig. 3.10 (b). The fabricated fingers are 200 μm deep, 400 μm long and 10 μm wide. In order to yield ideal finger width of 10 μm, the width should be pre-enlarged to 13 μm to compensate for the feature size shrinkage during ICP process. Fig. 3.11(a) showed the close-up view of fingers. The perpendicularity is about 89±0.99 degree, indicating minimum sidewall barreling, as shown in Fig. 3.11 (b).

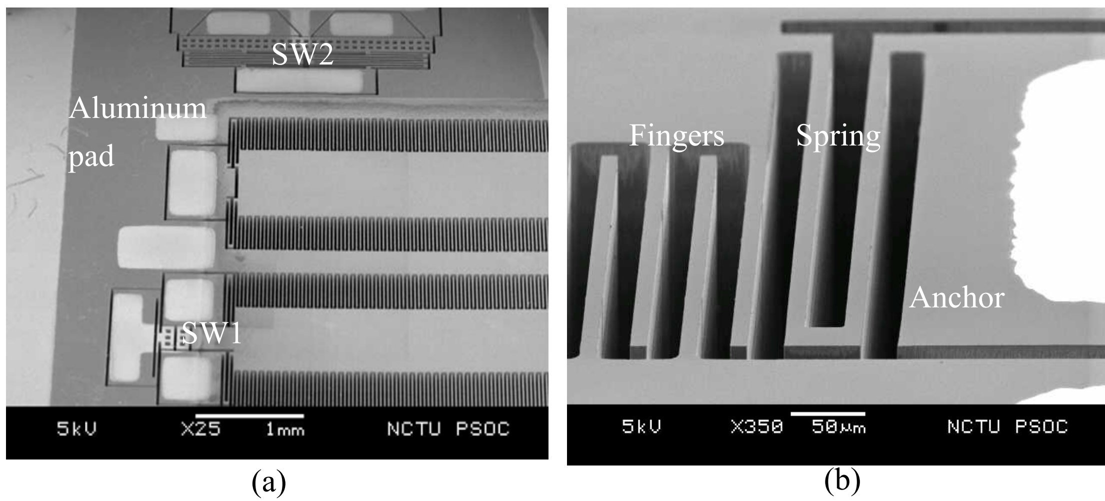

(a) (b)

Fig. 3.10 (a) Corner of device with aluminum deposition (b) Close up view of the serpentine spring

Fig. 3.12 shows the optical microscope view of the device with LPCVD nitride coating on the fingers. Fig. 3.13 shows the overview of whole device. The tungsten ball is attached to the center plate and positioned by the center hole on the device. Aluminum was deposited on the contact pads by sputtering with an accurate shadow mask.

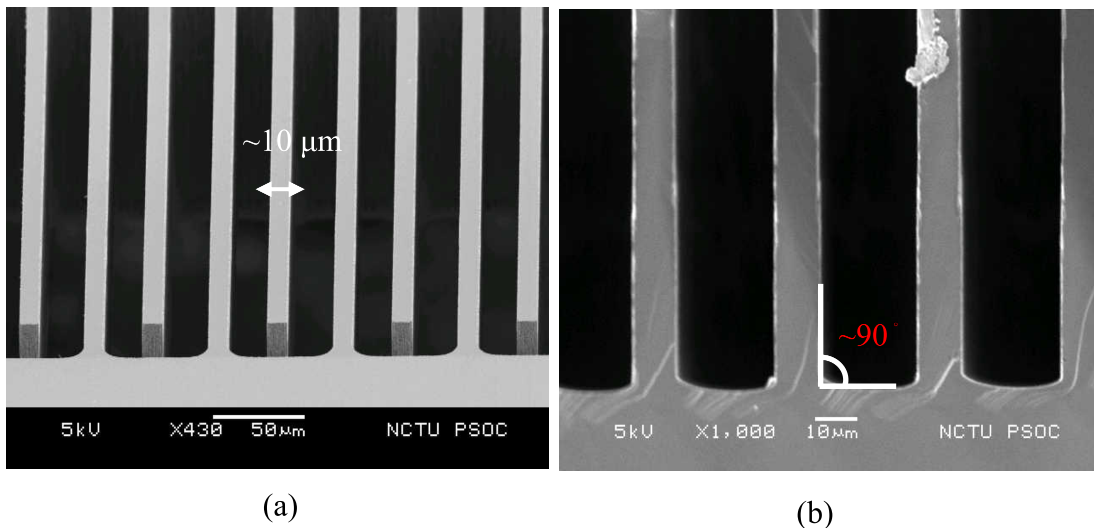

(a) (b)

Fig. 3.11 Close-up view of finger (a) width (b) perpendicularity

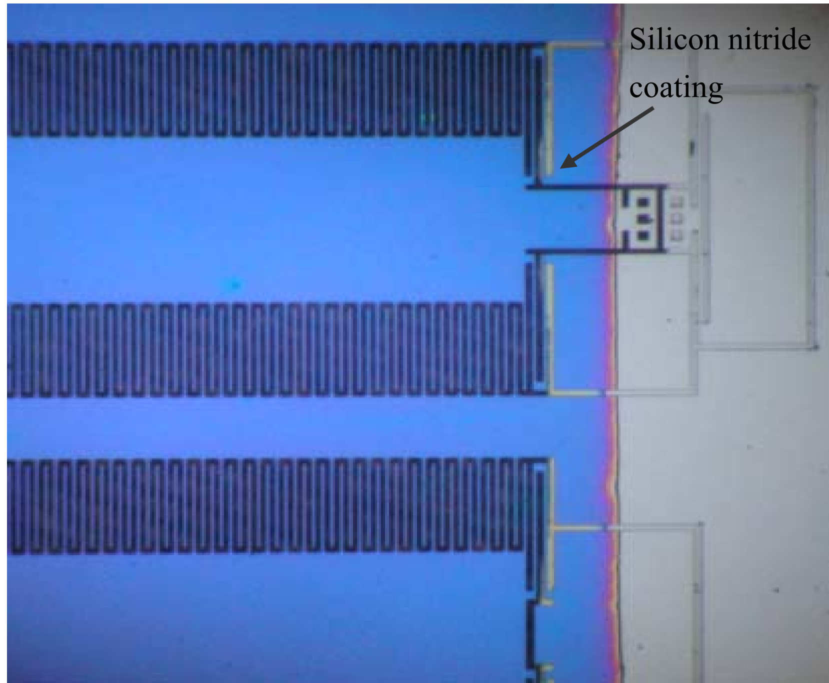

Fig. 3.12 Device with silicon nitride coating

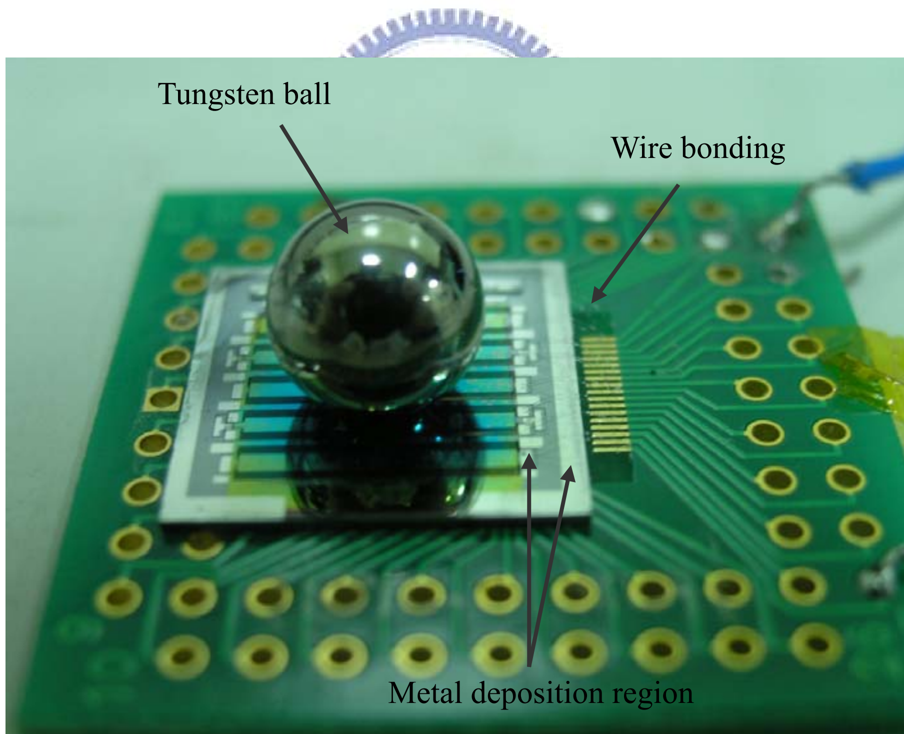

Fig. 3.13 Device with the external mass on the PCB board

3.4 Summary

The high aspect ratio SOI device was fabricated successfully. The fabrication issues were encountered and solved in the fabrication process. The leakage resistance between fingers was overcome by LPCVD silicon nitride deposition. The leakage can be solved by metallization with an accurate shadow mask. Subsequent measurement will be presented in the next chapter.

Chapter 4 Measurement and Results

The measurement of the vibration-to-electric energy converter fabricated by SOI deep silicon etching technology is presented in this chapter. Device displacement and resonance were observed in the mechanical measurement. Electrical measurements include static parasitic capacitance and resistance measurement. AC output power measurement is presented in the dynamic electrical measurement. Finally, mechanical switches were tested in a DC mode circuit.

4.1 Mechanical measurement

The objective of mechanical measurement is to measure the mechanical frequency response of the device around its resonant frequency. Mechanical characteristics of the device are measured with input vibration acceleration. The measurements will focus on the devices with the external tungsten ball attachment.

4.1.1 MEMS Motion Analyzer measurement

The device was first tested on the probe station with an optical microscope. The probes were used to push the movable plates of the devices to check if they were successfully released. Afterwards the devices were used to measure the dynamic response by the MEMS Motion Analyzer (MMA) in the National Chip Implementation Center (CIC). The photograph of the MMA measurement facilities provided by CIC is shown in Fig. 4.1(a). A mini-shaker was put on the platform and used to provide the input vibration, as shown in Fig. 4.1(b). A function generator was connected to the shaker to apply the driving signal. Fig. 4.1(c) shows the vibration amplitude of the mini-shaker with an estimated acceleration of 0.156 m/s^2. The device

was put on the mini-shaker with glue to ensure the stability during vibration. The MMA system utilizes image processing technique and measures the periodic relative motion between the movable and the still structures of the device.

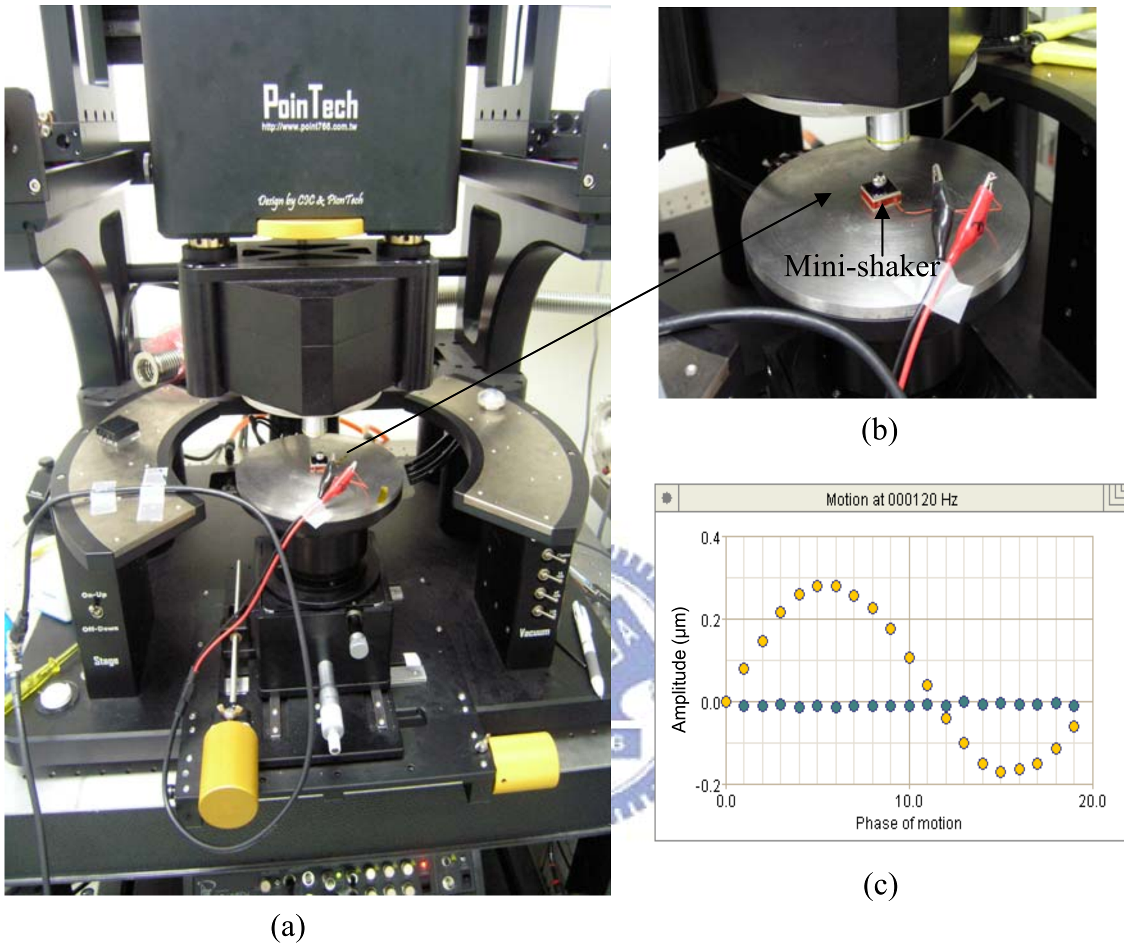

Fig. 4.1 (a) MMA system (b) Close view of the device on the mini-shaker (c) vibration amplitude of mini-shaker

The device with the external ball was measured by the MMA system. The experiment results are shown in Fig. 4.2. From the amplitude response by Fig. 4.2 (a), the resonant frequency is around 120 Hz, which is close to the data by CoventorWare simulation. The phase response is plotted in Fig. 4.2(b), which has a -112° phase shift at resonant. The results is different the -90° theoretical phase shift due to the phase offset around DC.

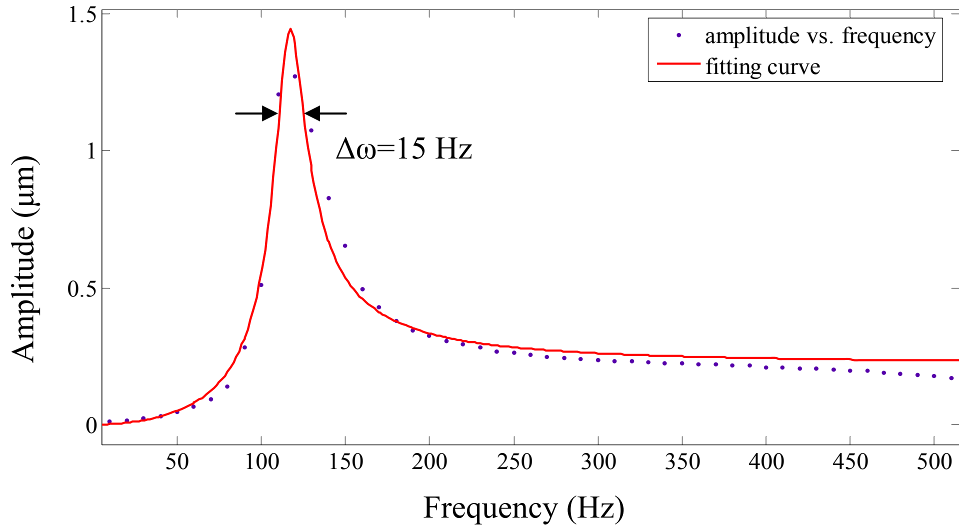

(a)

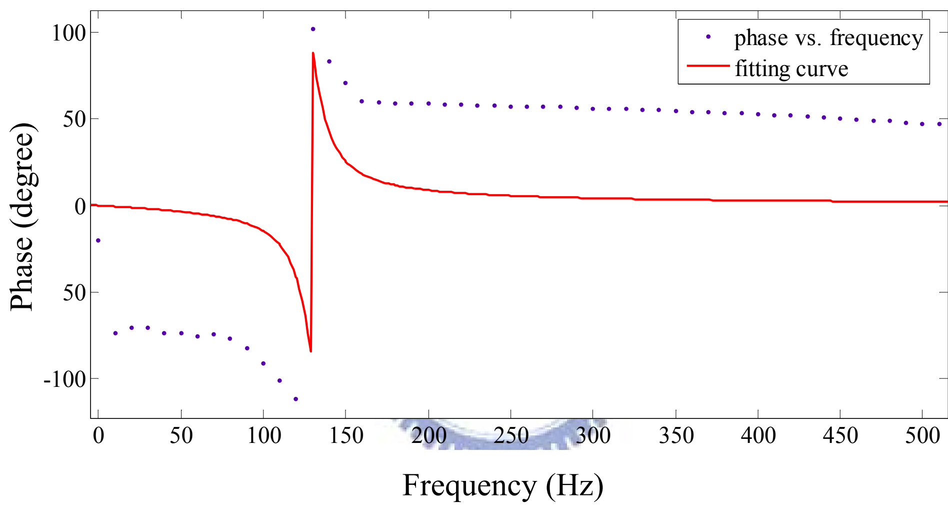

(b)

Fig. 4.2 MMA experiment results with metal ball (a) amplitude response (b) phase response

The amplitude and phase response match a mass-damper-spring system characterized by the equation

$$|Z|=\frac{m\omega^2}{\sqrt{(k\text{-}m\omega^2)^2+b_m{}^2\omega^2}}|Y|, \tag{4.1}$$

$$\phi=-\tan^{-1}\frac{b_m\omega}{k-m\omega^2}, \tag{4.2}$$

where Y as the input displacement amplitude, Z as the output displacement amplitude, and ϕ is the phase difference. The response is zero at DC frequency and constant

when frequency is over the resonant frequency. The amplitude response indicates a 3dB bandwidth of about $\Delta\omega$ = 15 Hz, and the quality factor is 8. The low value does not match the expectation by the equation.

$$Q = \sqrt{\frac{km}{b_m^{\ 2}}} \tag{4.3}$$

From the equation, the device operated in the low-damping environment is considered in order to get high quality factor. So the device packaging is the current solution.

4.1.2 Vibration measurement by our shaker

The mechanical behavior of devices was also measured by our own measurement system, as shown in Fig. 4.3. The amplified sinusoidal signal was used to drive a LABWORK INC. ET-132 shaker. The sinusoidal vibration was measured by a piezoelectric accelerometer connected to an oscilloscope. The resonance of device was observed by an optical microscope and the image of relative displacement was captured by a digital camera.

Our measurement results are shown in Fig. 4.4. Fig. 4.4(a) shows the static mode. The frequency can be operated from 100 Hz to 150 Hz to find the resonant frequency. By the optical microscope and digital camera, the resonant frequency was 116 Hz, which agreed approximately with the MMA experiment results. For the vibration accelerometer of 2.2 m/s^2, the device has a large displacement of 20.2 μm due to the large inertial force caused by the external mass, as shown in Fig. 4.4 (b). The value of acceleration also agrees with the vibration characteristic from the Fig. 2.1. The input acceleration measured by the accelerometer module is shown in Fig. 4.4 (c) with the sensor sensitivity of $100mV/ms^{-2}$. Thus, the input vibration amplitude is about 2.2 m/s^2.

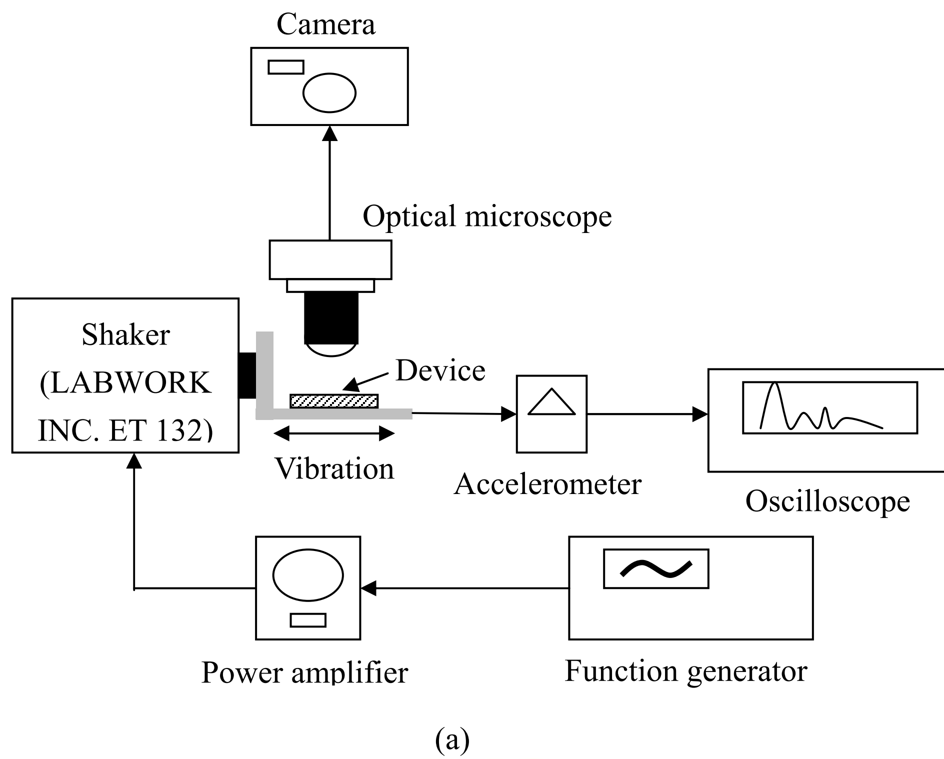

(a)

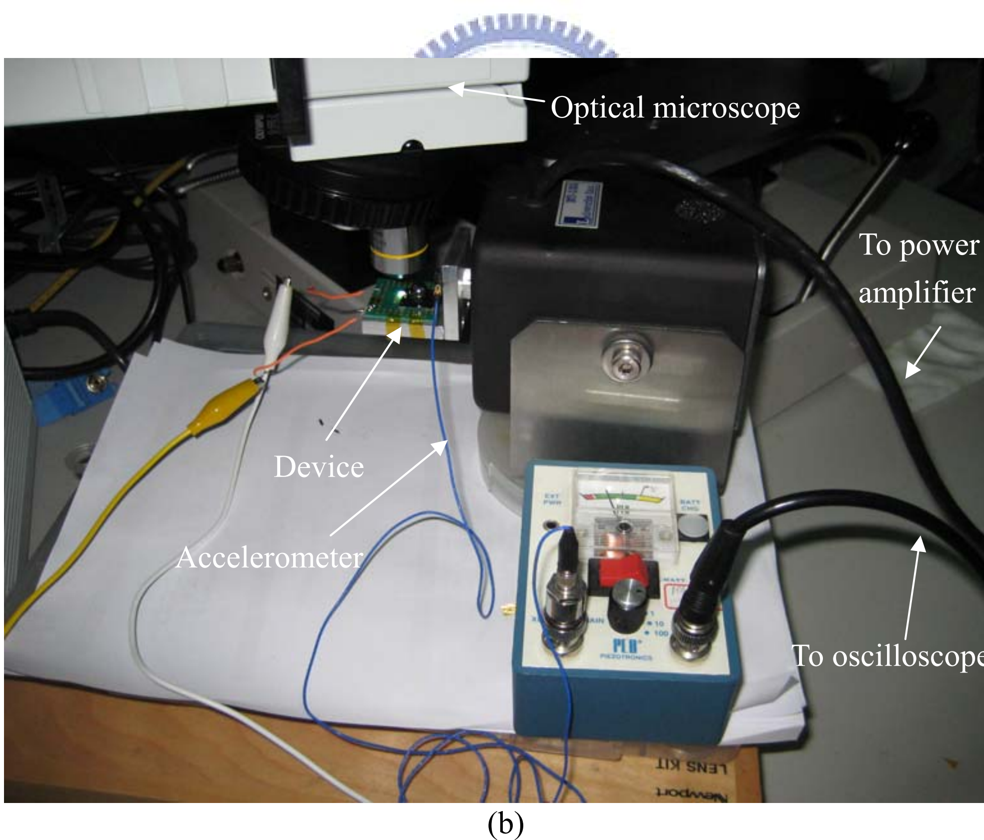

(b)

Fig. 4.3 (a) Measurement schematic (b) our mechanical measurement setup

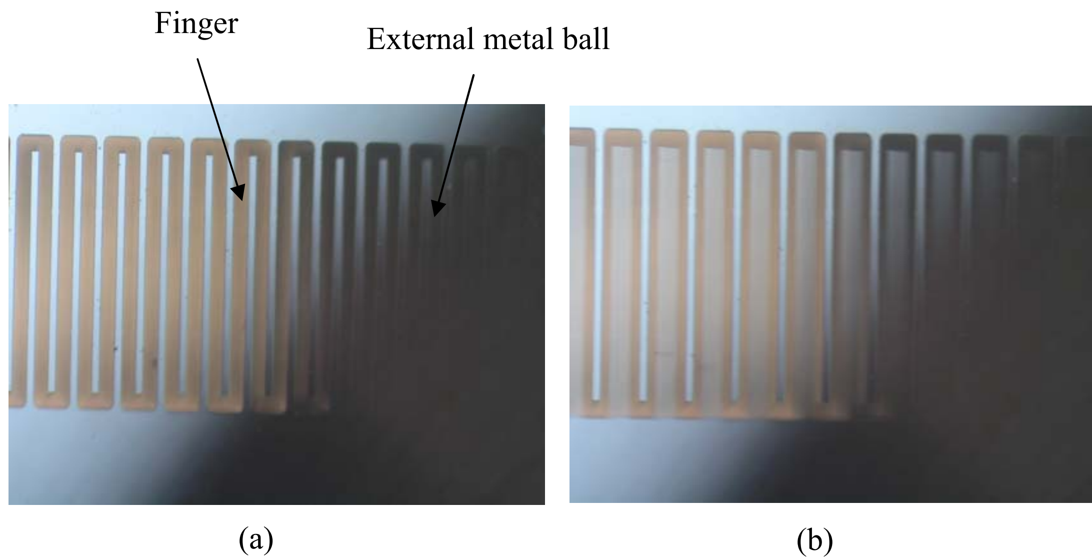

(a) (b)

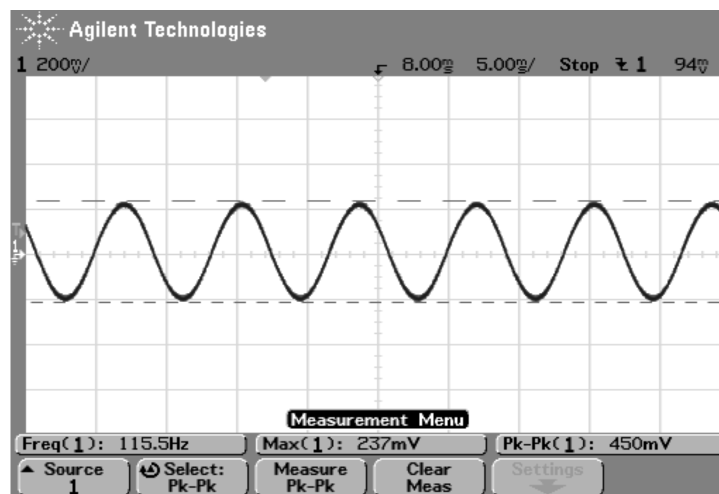

(c)

Fig. 4.4 (a) Static device (b) device operates at resonant frequency of 116 Hz (c) resonance acceleration waveform.

4.2 Static electrical measurement

In static electrical measurement, the variable capacitance and leakage effects were measured. In order to prevent the leakage resistance, the better insulation layer deposition, such as LPCVD nitride, was employed. The measurement results were compared with the PECVD nitride coating.

4.2.1 Measurement for PECVD nitride deposition

In this section the device was coated by the PECVD silicon nitride layer. In order to ensure good isolation of the device, a measurement circuit was setup to measure the leakage resistance, as shown in Fig. 4.5. The DC current through the device is zero if no leakage resistance R_p exists, resulting in a zero voltage drop across R_L. The input bias current of the CA314 CMOS operational amplifier is below 10 pA, and the output voltage offset caused by the buffer can be neglected. Using this measurement circuit with V_L = 9 V and R_L = 10 MΩ, the output voltage was 7.8 V, indicating a leakage resistance of about 1.53 MΩ. The leakage resistance was also observed by the LCR meter. The experiment results agreed with the measurement from Fig. 4.5. Due to the bad leakage resistance, the good insulation layer deposition will be employed and discussed in the next section.

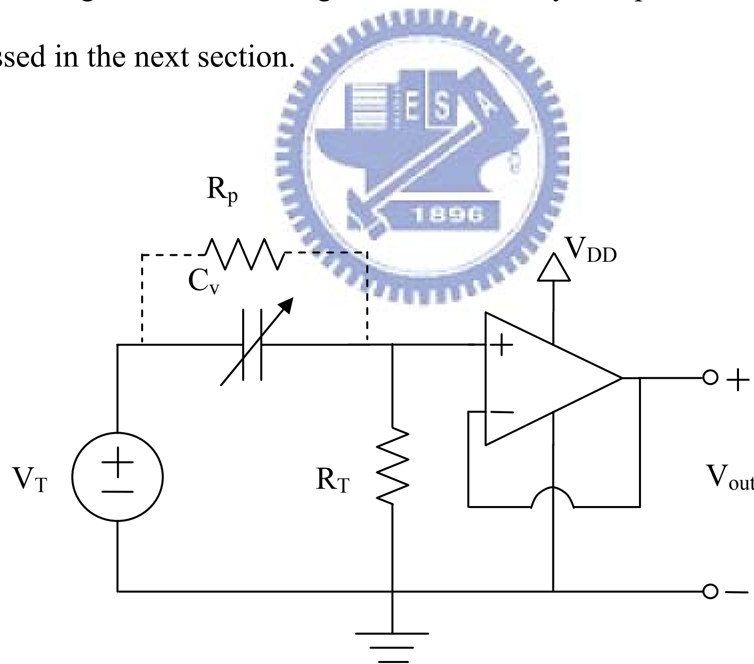

Fig. 4.5 Leakage resistance measurement circuit

Another circuit was constructed to measure the RC discharge time constant versus finger displacement, as shown in Fig. 4.6. In this case, SW_r is a relay controlled by a 5 V input V_{tri}. The relay SW_r is initially opened and subsequently the

relay SW_r is closed at the pulse wave of the control voltage V_{tri}. The variable capacitor is charged to $V_{in,}$ and then the relay is opened so that charge on C_v is discharged through R_L. The pulse wave of V_{tri} is produced by a function generator to trigger the switch.

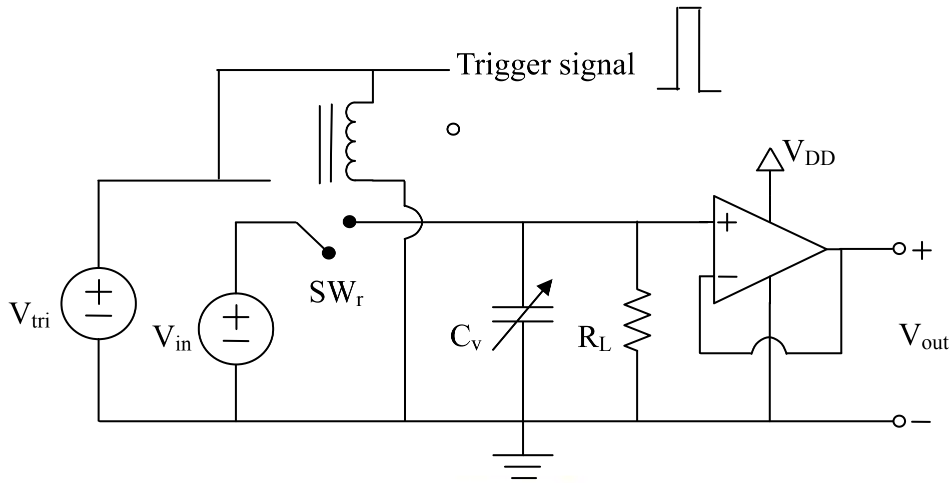

Fig. 4.6 Variable capacitor measurement circuit

With a R_L of 10 MΩ and a V_{in} of 9 V, the RC discharge time constant versus finger gap displacement is measured. Fig. 4.7 shows the RC discharge for different positions of the variable capacitor. The variable capacitor is moved by a microprobe and the static displacement is measured from the image captured by the optical microscope. The RC discharge time constant was calculated from the time span of 100% to 37% voltage drop.

The discharge resistance is equal to the parallel connection of R_T and the leakage resistance. The capacitance can then be calculated from the time constant. The calculated value of variable capacitor (C_{actual}) can be compared with the theoretical value (C_{ideal}), which is plotted in Fig. 4.8. The calculated value of the minimum variable capacitor is 91.5 pF (theoretical value of 60 pF), indicating the parasitic capacitance of 30 pF in the device.

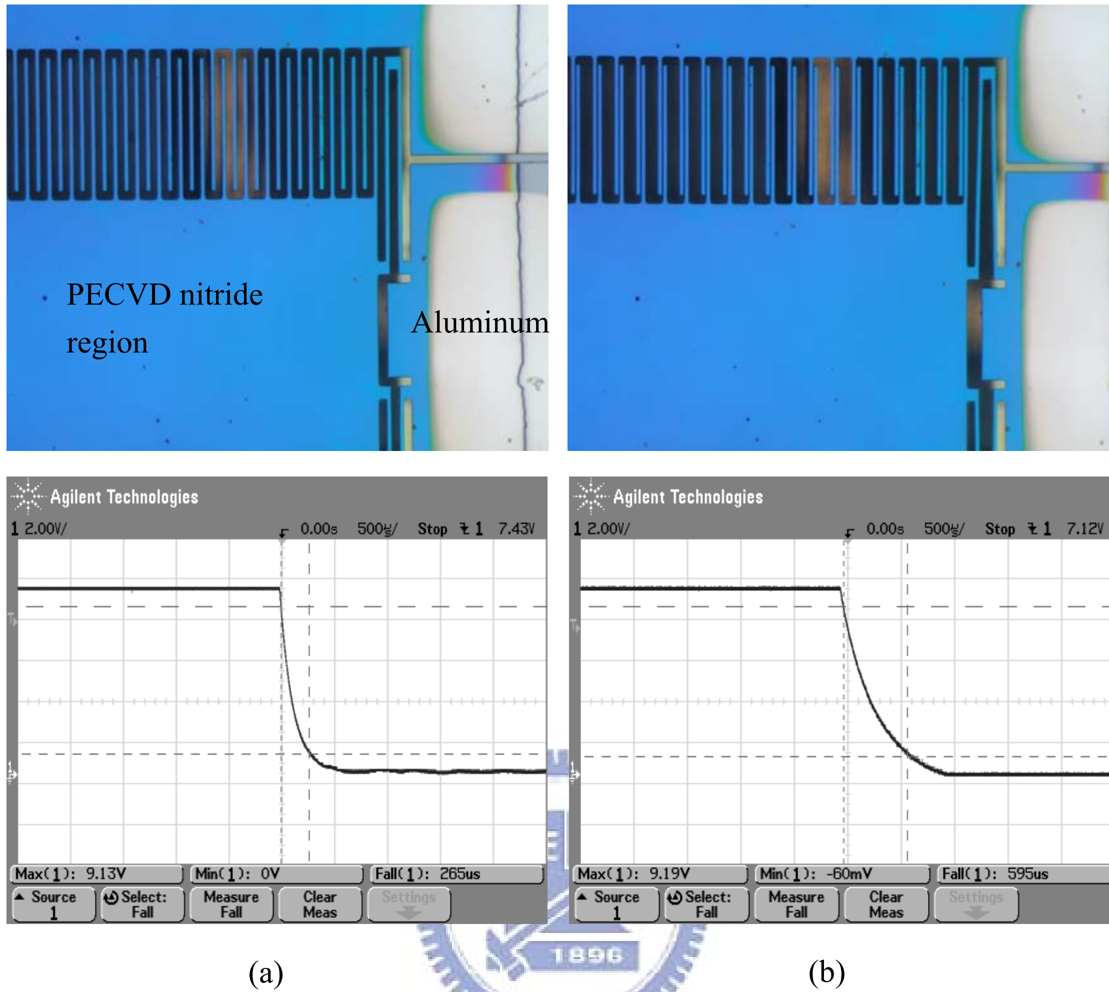

Fig. 4.7 RC discharge time constant measurement for PECVD deposition (a) Zero displacement, time constant τ=95 μs (b) maximum displacement of 25 μm, time constant τ=287 μs

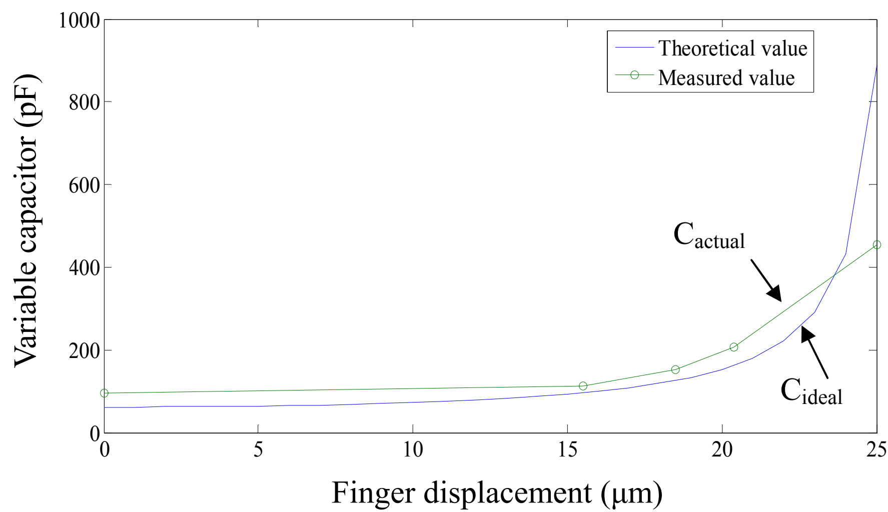

Fig. 4.8 Measured variable capacitor versus displacement

Moreover, the maximum capacitance of 455 pF is lower than theoretical value C_{ideal} of 905 pF. Therefore, the oblique sidewall issues were considered. A non-parallel capacitance structure was defined by the non-ideal ICP etching [43]. The schematic of non-parallel capacitance is shown in Fig. 4.9. h is thickness of fingers, θ is the oblique angle of the fingers sidewall, and d_1 and d_2 are gap between the fingers. The non-parallel capacitor C_{actual} is expressed as follow [43]

$$C_{\text{actual}} = \frac{\varepsilon L_f}{2\theta} \ln\left(\frac{(d_1 + 2h\theta)(d_2 + 2h\theta)}{d_1 d_2}\right) \tag{4.4}$$

The ratio between the actual and the ideal capacitance (θ=0) is

$$r = \frac{C_{\text{actual}}}{C_{\text{ideal}}} = \frac{d_1 d_2}{2h\theta(d_1 + d_2)} \ln\left(\frac{(d_1 + 2h\theta)(d_2 + 2h\theta)}{d_1 d_2}\right) \tag{4.5}$$

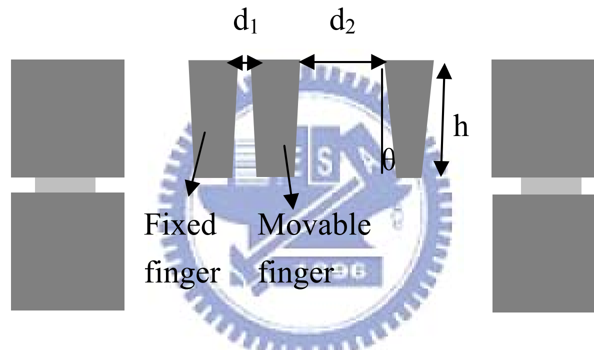

Fig. 4.9 Cross-section of non-parallel capacitor

The relationship between the oblique angle and ratio is plotted in Fig. 4.10. The ideal maximum capacitance of 905 pF is shown in Fig. 4.8. Our measurement result of the maximum capacitance implies an oblique angle of 0.2 degree. The results can be confirmed by the SEM photo, as shown in Fig. 4.11(a), which shows the oblique finger sidewalls. Furthermore, the unflat surface of sidewall also determines the non-ideal gap between the fingers and thus produces the non-ideal maximum capacitance, as shown in Fig. 4.11(b). The issues are mentioned in the chapter 3. To improve this issue, a suitable recipe of ICP will be adopted.

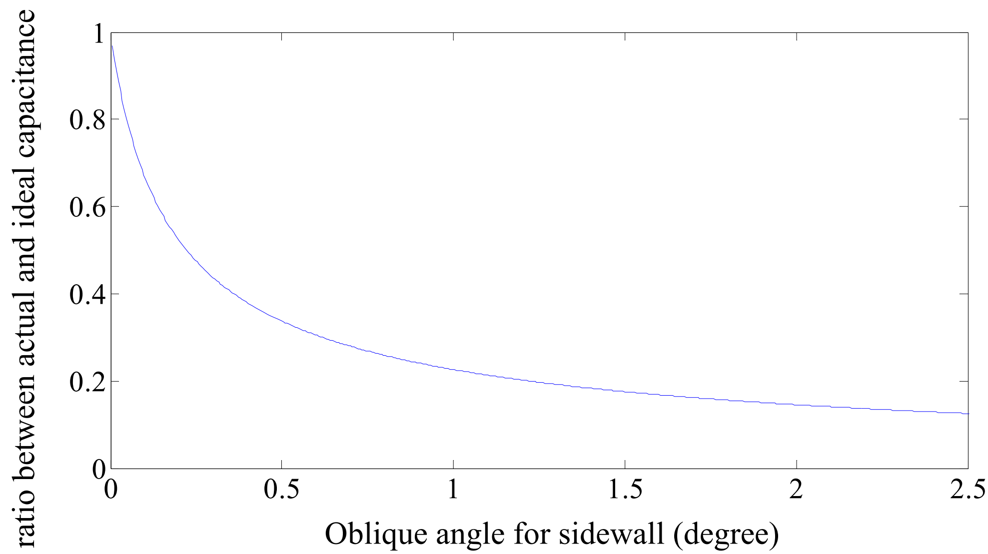

Fig. 4.10 C_{actual}/C_{ideal} versus oblique angle

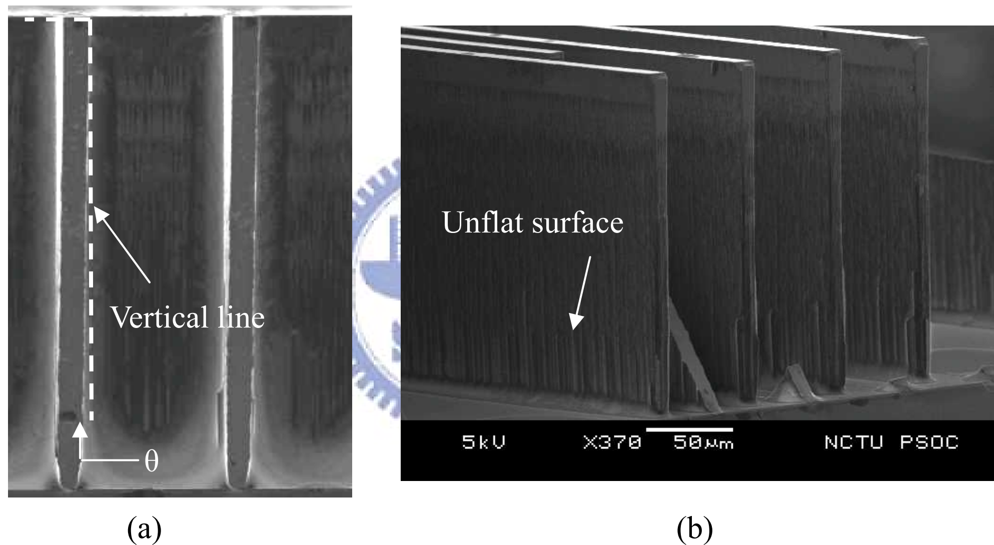

(a) (b)

Fig. 4.11 SEM photo (a) Close up of non-parallel capacitance (b) unflat surface of finger sidewall

4.2.2 Measurement for LPCVD nitride deposition

As mentioned in previous section, the PECVD poor step coverage has the leakage resistance issues. Therefore, LPCVD nitride coating was adopted due to the better step coverage and high isolation. Low-stress silicon nitride was coated successfully at the temperature of 850°C in the furnace system. The device was also measured by the circuits shown in Fig. 4.5 and Fig. 4.6. From the leakage resistance measurement circuit, it has the low output voltage of 0.8 V, indicating a leakage

resistance of about 102 MΩ. The experiment results verified the parasitic resistance improvement by utilizing LPCVD nitride coating. The discharge time constant measurement is shown in Fig. 4.12 with V_{in} = 9 V and R_L = 10 MΩ. The discharge time constant increases with increasing displacement. The LCR meter shows that the variable capacitance ranges from 106 pF to about 455 pF, which approximately agreed with the calculated value.

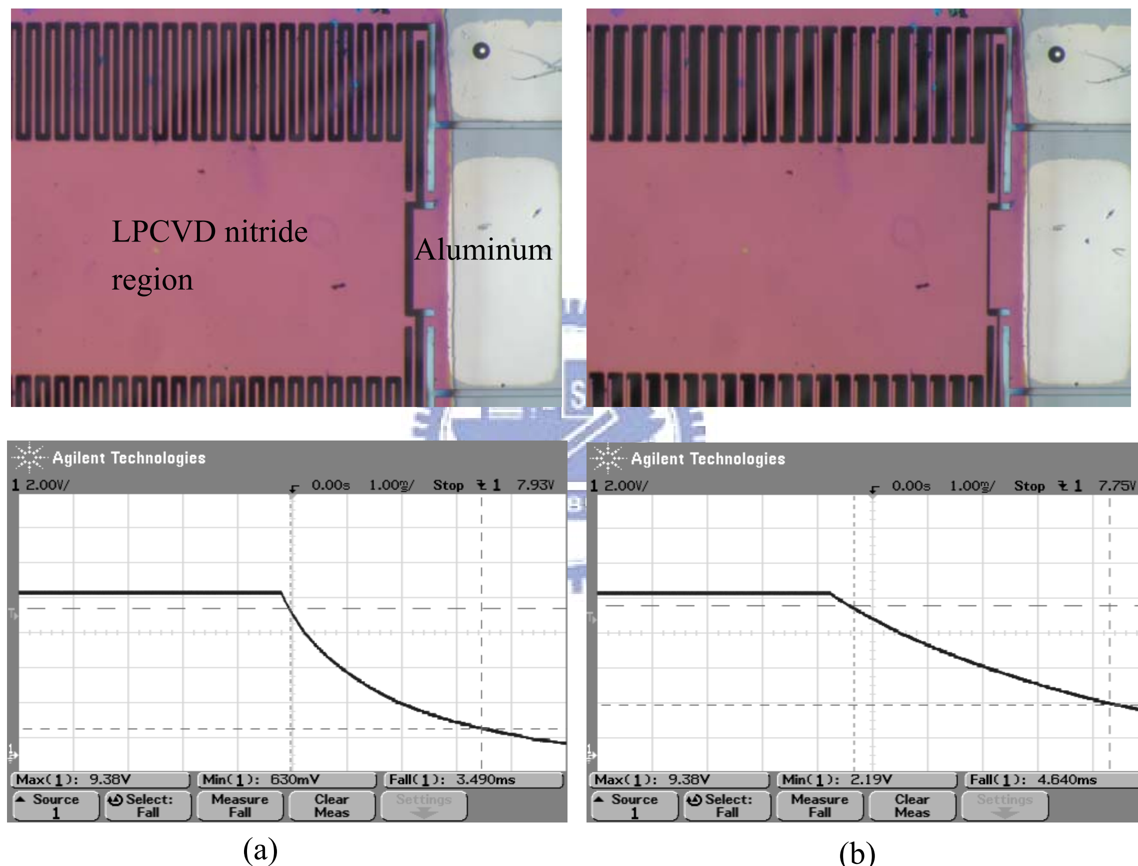

(a) (b)

Fig. 4.12 RC discharge time constant measurement for LPCVD deposition (a) zero displacement, time constant τ = 1.13 ms (b) maximum displacement of 25 μm, time constant τ = 4.36 ms

The discharge time constant of LPCVD nitride coating can be compared with the PECVD nitride deposition, as shown in Fig. 4.13. By the LPCVD nitride deposition, the discharge time constant was increased, indicating the leakage resistance improvement. Furthermore, the accurate shadow mask plays an essential role to

prevent the short circuit during the metal deposition process. The test of will the mechanical switch circuit will be discussed in the next section.

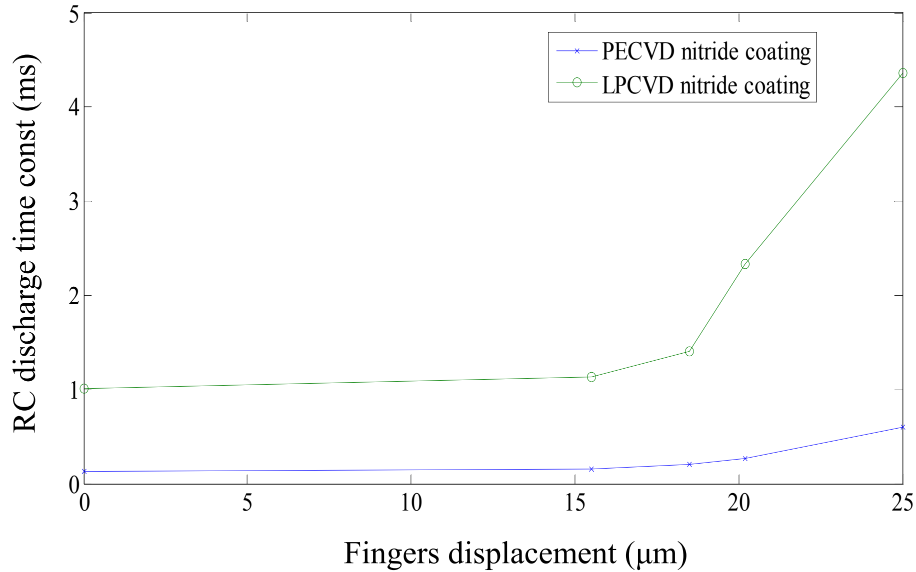

Fig. 4.13 Discharge time constant for PECVD and LPCVD nitride deposition

4.3 Dynamic electrical measurement

The electrical measurement of the device with input vibration is discussed in this section. AC mode circuit was constructed to measure the AC output power, which utilizes the DC voltage source to charge the variable capacitor. With the change of the charge on the capacitor, the AC current was produced. The DC mode circuit has two charge-discharge timing control switches utilize mechanical switch. If the switches timing control are precise, the DC output power can be measured. Thus, the mechanical switches are tested before the DC power measurement.

4.3.1 AC mode power measurement

The AC mode circuit was used for power measurement of the device, as shown in Fig. 4.14. AC current can be generated with the change of C_v and results in an AC power to the load resistance R_L. The small capacitor C_T used to block the DC path in

the device. Therefore, it has no net power dissipation for the input voltage in this circuit, which implies a longer lifetime source. In addition, the mode can serve as an alternative energy conversion mechanism when the vibration amplitude is lower than the targeted value.

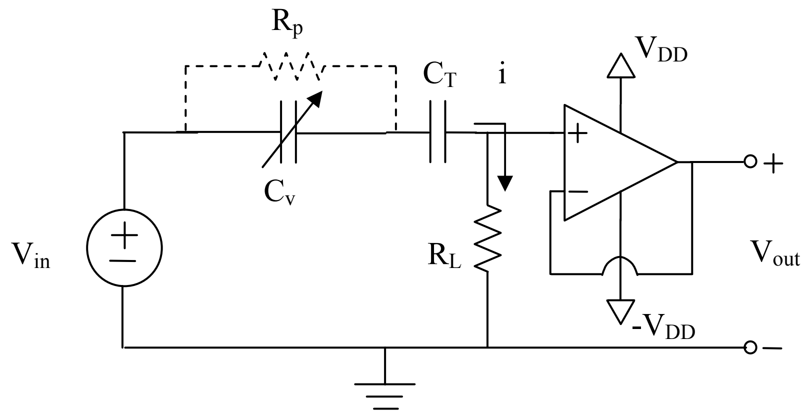

Fig. 4.14 AC mode power measurement circuit

With the external mass attachment of the device, the resonant frequency of device is 116 Hz. But the frequency was distributed by low frequency noise from the instrument. Thus the first mode harmonic frequency around 182 Hz was adopted. The vibration acceleration amplitude is maintained at about 2.2 m/s^2 at the frequency of 182 Hz. The device has a relative displacement of about 12.5 μm. Therefore, the change of variable capacitor is from 106 pF to 195 pF shown in Fig. 4.8. Various load resistances R_L were tested and experiment results were shown in Fig. 4.15. There is a -110° phase shift between the input vibration acceleration and the output voltage at frequency of 182 Hz. The results do not agree with the theoretical value of 15.5° in Eq. 4.2. The AC output power can be expressed as

$$P_{\text{out}} = \frac{V_{\text{out}}^{2}}{R_{\text{L}}} \tag{4.6}$$

Thus the maximum power for the device with mass attached is 17.5 nW at the optimal load resistance of 3.33 MΩ, as shown in Fig. 4.16. The output power was much smaller than the theoretical value. Thus the theoretical value will be discussed as

follow.

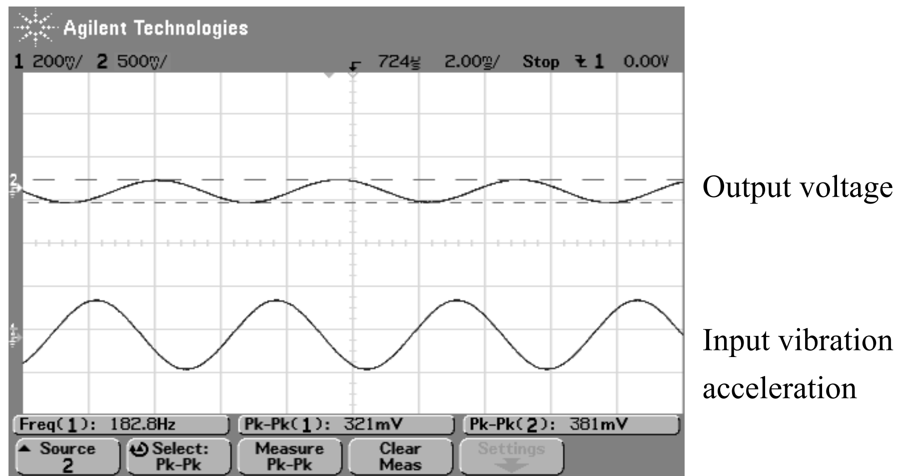

(a)

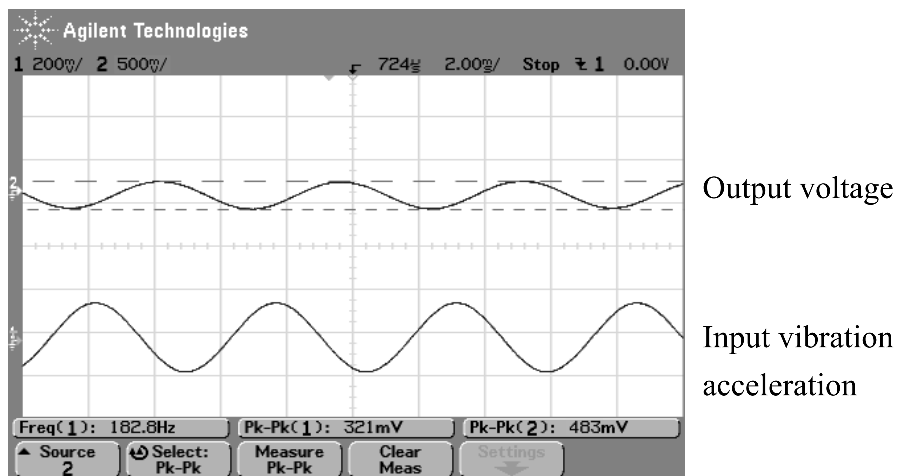

(b)

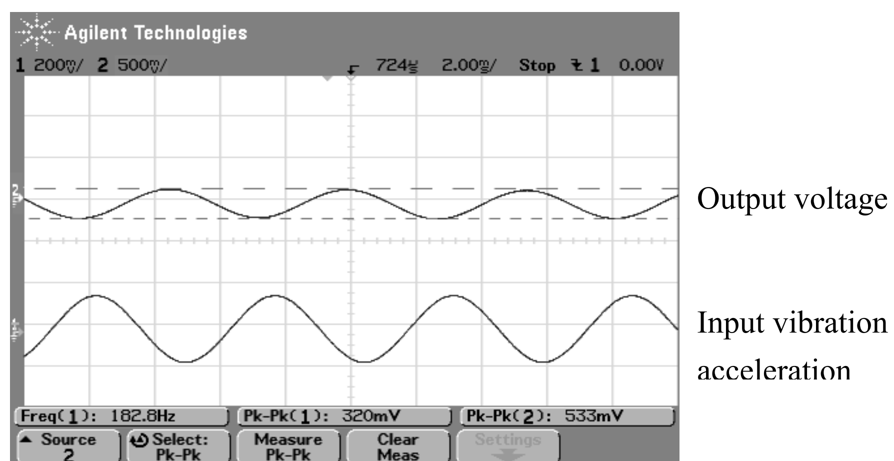

(c)

Fig. 4.15 AC power measurement with mass attached for various load resistances (a) 2.5 MΩ (b) 3.33 MΩ (c) 10 MΩ

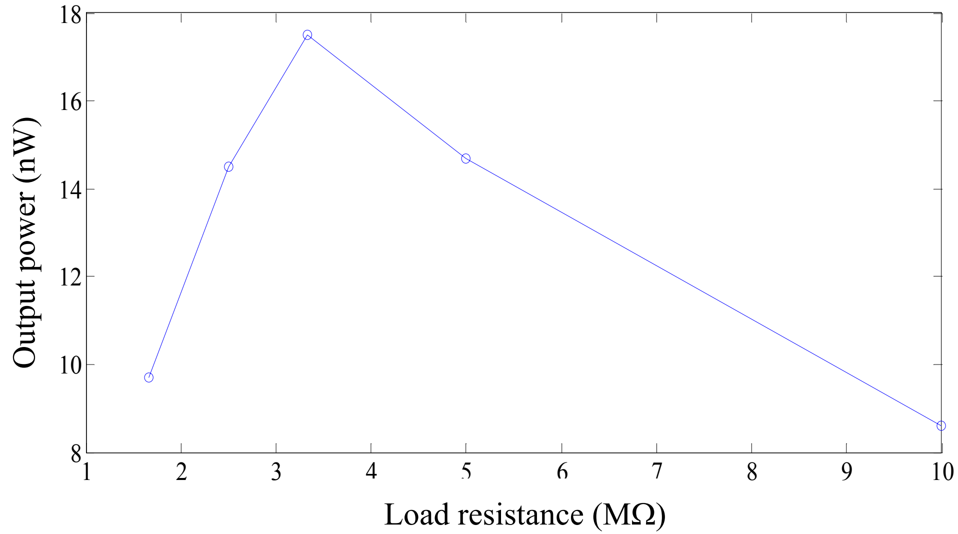

Fig. 4.16 AC power measurement with various load resistance

The theoretical AC output power can calculated from the circuit in Fig. 4.14. The AC current can be calculated as follow

$$i = \frac{dq}{dt} = \frac{d(C_v V_c)}{dt} = (V_{in} - iR_L)\frac{dC_v}{dt} - R_L C_v \frac{di}{dt} \tag{4.7}$$

The nonlinear equation was solved by Simulink simulation. The variable capacitance C_v changed by the external vibration source at the frequency of 182 Hz. The external vibration source causes the fingers relative displacement z (Fig. 2.8), which is related to C_v from the Eq. 2.15. For the optimal resistance of 3.33 MΩ, the amplitude of AC current is 0.48 μA at frequency of 364 Hz, as shown in Fig. 4.18. However, the frequency of the measured output voltage is identical to the input vibration in Fig. 4.17. This indicates that the output power was not be generated by the variable capacitor. A possible source is the metal traces on the PCB board which induces the parasitic variable capacitor C_b between the movable finger and metal membrane, as shown in Fig. 4.18. The overlap area between the movable fingers and metal membrane cause a small variation of capacitance which induces an AC current at frequency of 182 Hz. In order to solve this issue, a modified AC circuit is in progress.

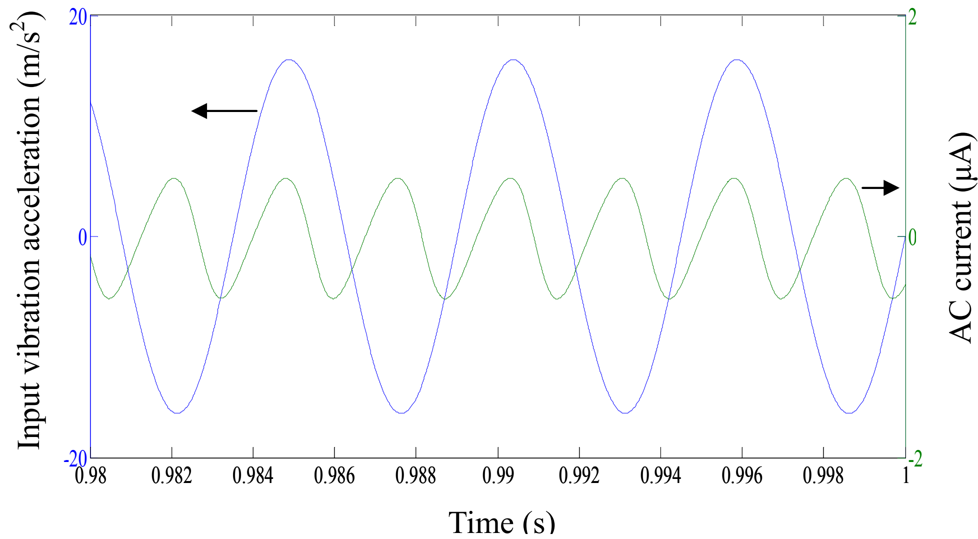

Fig. 4.17 Simulation results for AC model circuit

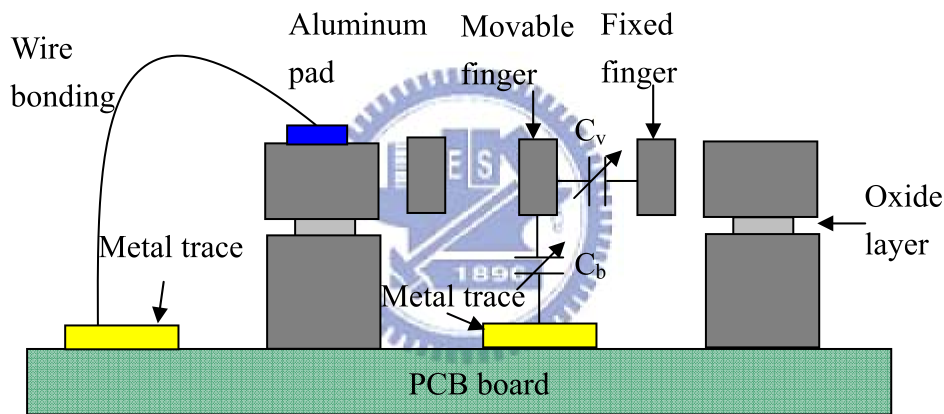

Fig. 4.18 Schematic of parasitic variable capacitor C_b generation

4.3.2 DC mode power measurement

Our mechanical switches are designed to work in the DC mode circuit, as shown in Fig. 4.19. First of all, SW1 should be turned on in the charging process. Thus, a microprobe was use to push the movable plate to reach the SW1 touch position, as shown in Fig. 4.20. The aluminum wire was bonded to the PCB. With a voltage supply of 3.6 V, the voltage of the variable capacitor was measured by an oscilloscope, as shown in Fig. 4.21. It shows that the switch was turned on and charging was finished.

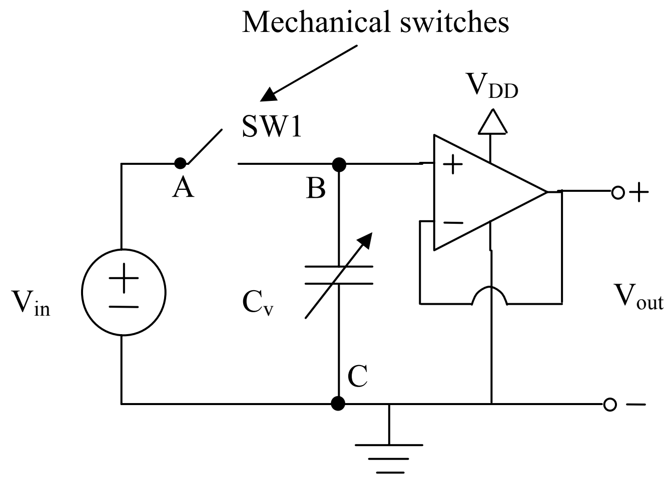

Fig. 4.19 DC model with mechanical switches

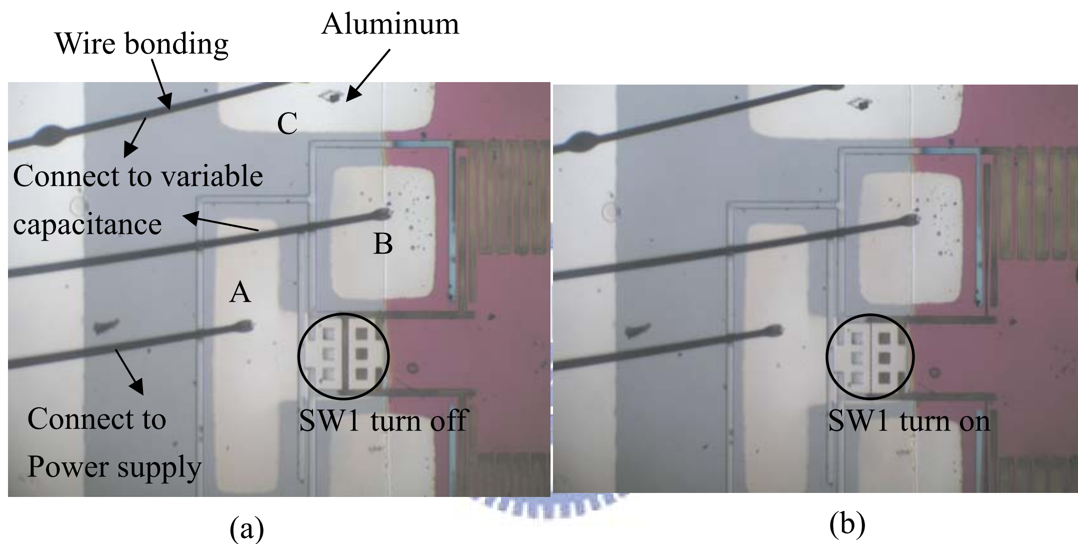

Fig. 4.20 Mechanical switch SW1 is (a) turning off (b) turning on

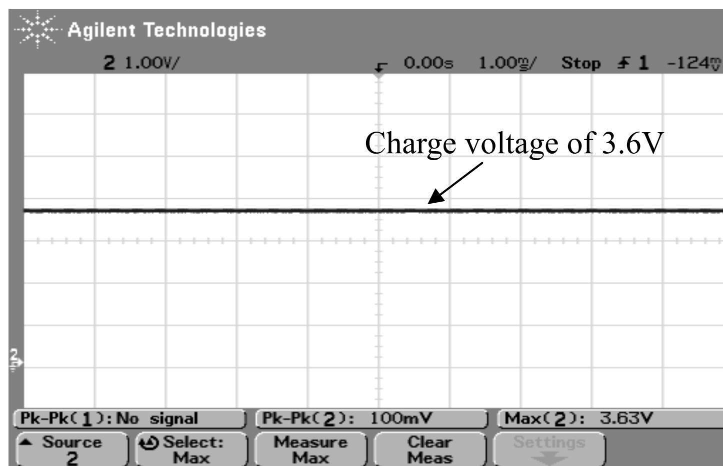

Fig. 4.21 Charge Voltage

According to Eq. 2.27, the voltage of the variable capacitor increases with the decreased capacitance. SW1 are turned on when the maximum relative displacement of fingers are reached. Thus the magnitude of vibration should be large enough for the fingers to touch. The device without the mass attached was operated at the resonant frequency of 1740 Hz and the vibration acceleration of 26.7 m/s^2. The voltage on the variable capacitor was measured in Fig. 4.22. It shows the voltage of 3.6 V during the charging process. The maximum voltage V_{max} of variable capacitor is 11.64 V which was smaller than the theoretical values of 52 V from Eq. 2.27, indicating the change of variable capacitance is small. Besides, the frequency of output voltage on the variable capacitor is twice of the input vibration acceleration shown in Fig. 4.23, which does not agree with our measurement results. It indicated that the one side of the mechanical switches was only touched. Thus, it does not perform the DC output power measurement.

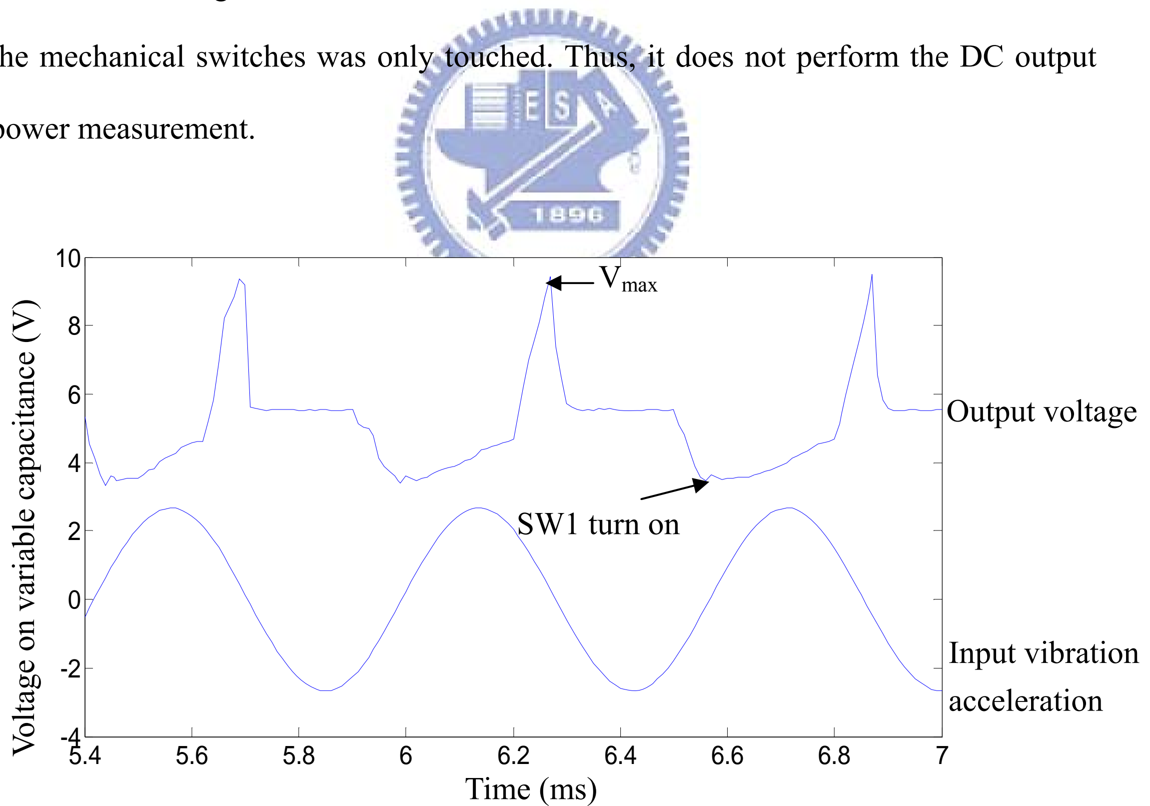

Fig. 4.22 Voltage on the variable capacitor

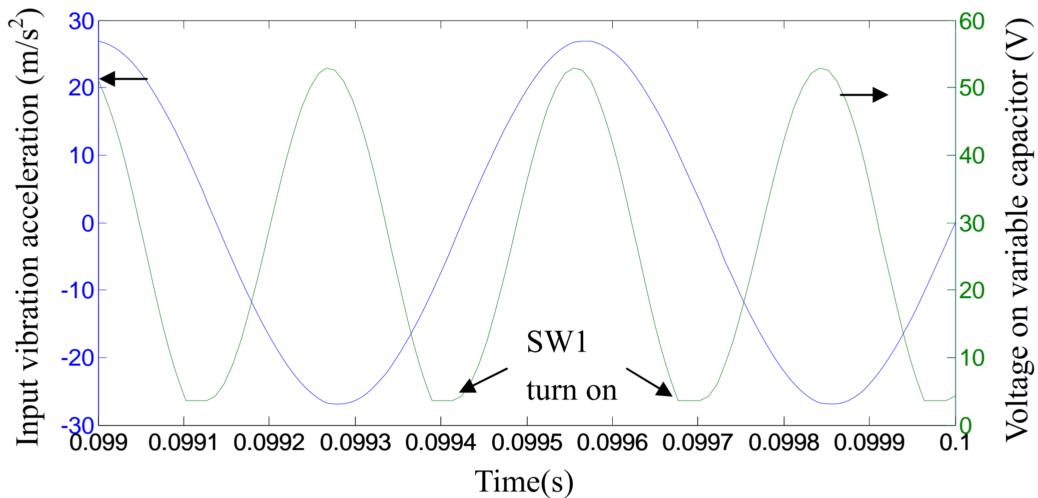

Fig. 4.23 Simulation results for the circuit from Fig. 4.19

4.4 Summary

The experiment results of mechanical and electrical measurement were presented. Mechanical characteristics of the energy converter were analyzed by the MMA system. The resonant frequencies were also measured by a LABWORK INC. ET-132 shaker and optical microscope. Fig. 4.13 shows an increase of time constant due to leakage resistance improvement. As a result of non-parallel capacitor effect, the change of variable capacitor does not reach the theoretical value. AC output power measurement with mass attached was conducted. Finally, mechanical contact switches (SW1) test was finished. The maximum voltage is not the expectation value when the fingers reach the maximum displacement. So the DC power measurement was failure.

Chapter 5 Summary and Future work

5.1 Summary

The design and analysis of an electrostatic micropower generator without external mass attachment was accomplished. The optimal design parameters were found from the theoretical analysis and calculation. The modal simulation of the device was performed. The results agreed with the theoretical design value. With the 1 cm^2 chip area constraint, the device without external mass attachment can generated an output power of 0.51 μW at output voltage of 5 V by using an external voltage source of 0.3 V.

In the fabrication process, the modified device structure was proposed. The modified device was fabricated in an SOI wafer. LPCVD nitride deposition was adopted to prevent the leakage issue for the device. An accurate shadow mask was used to pattern separate electrical pad in order to avoid the electrical connection.

The mechanical characteristics of the device were observed by using the vibration of the shaker. The resonant frequency with the external mass attachment was about 120 Hz with quality factor of 8. The experiment result agreed with the device design value but the quality factor does not meet our expectation. Parasitic resistance was improved and verified by using discharge time constant measurement. AC mode circuit with external mass was performed. With the frequency of 182 Hz, the output power was 17.5 nW at the optimal load resistance of 3.3 MΩ. The frequency of induced AC current was identical the vibration acceleration. It indicates that the measured power was not be generated from the variable capacitor between fingers. Finally, mechanical switches on the device were already tested.

5.2 Future work

In our operation circuit, the variable capacitor was charged initially by using an external DC voltage source such as a battery. But the lifetime and volume of the battery limited the application of this converter. Therefore, the converted energy transferred to the input power source will be considered. The external voltage source is replaced with the flyback circuitry, as shown in Fig. 5.1 [24].

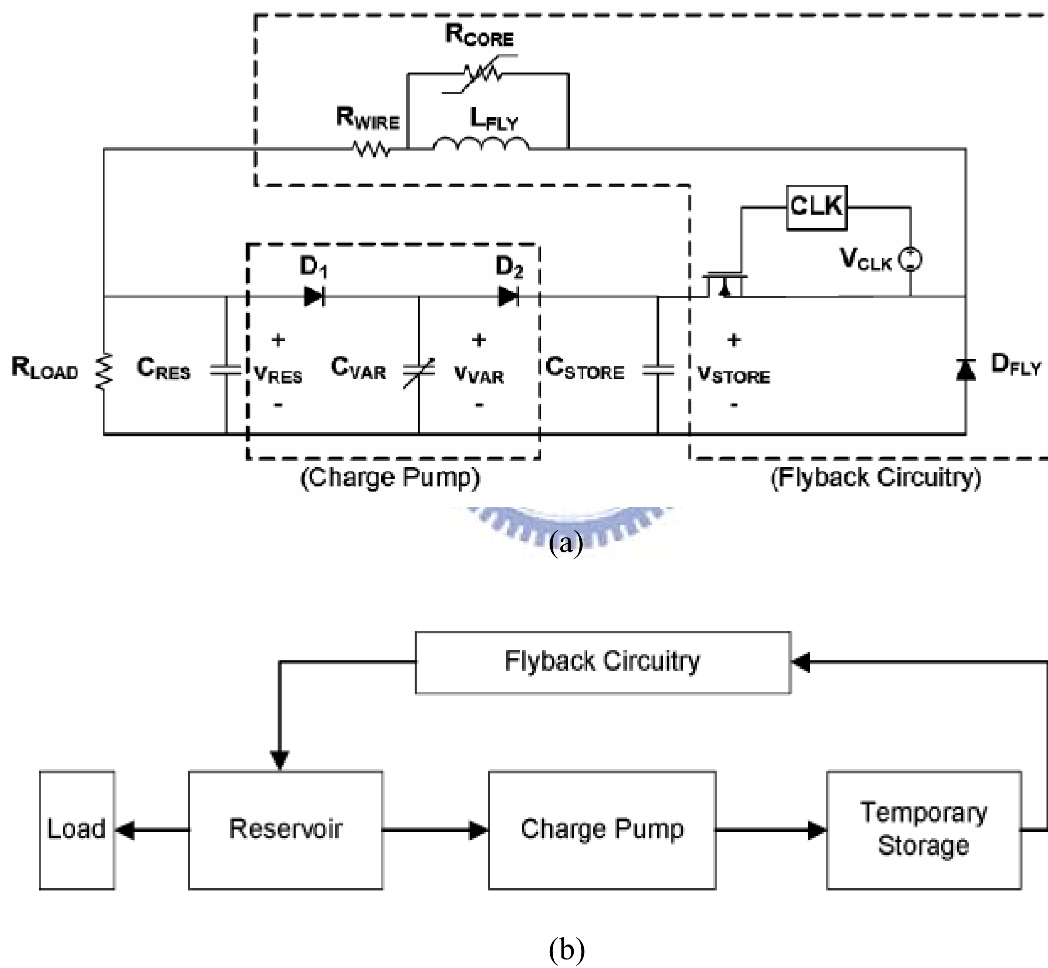

Fig. 5.1 Energy harvester with (a) flyback circuitry (b) operation block diagram [24]

The circuit employs a charge pump in the forward path and inductive energy flyback to return net energy to a reservoir. The flyback circuitry has the advantage of

producing the steady DC output power without any external voltage source during the vibration. In addition, it has no complex fabrication such as electrets material [25].

Theoretical analysis for energy scavenging technology is an essential objective in our effort. Energy scavenging from the vibration can be converted into the electrical power through different methods such as electrostatic, electromagnetic, and piezoelectric. But it has difficulty in discussing difference each other due to the different characteristic between these methods. Thus, the common theoretical description or comparison foundation will be proposed. And then the optimal parameters are found out for device design or characteristic comparison standard.

References

[1] "Battery Power Trade-offs, Low Voltage or Higher Capacity," EE Times, 2002.

[2] B. Linden and T. Reddy, *Handbook of Batteries*: New York: McGraw-Hill, 2002.

[3] J. N. Harb, R. M. LaFollette, R. H. Selfridge, and L. L. Howell, "Microbatteries for self-sustained hybrid micropower supplies," *Journal of Power Sources,* vol. 104, pp. 46-51, 2002.

[4] A. Heinzel, C. Hebling, M. Muller, M. Zedda, and C. Muller, "Fuel cells for low power applications," *Journal of Power Sources,* vol. 105, pp. 250-255, 2002.

[5] M. Buchmann, "Ultracapacitors from Nanoparticles," 2003.

[6] L. G. Frechette, C. Lee, S. Arslan, and Y. C. Liu, "Design of a Microfabricated Rankine Cycle Steam Turbine for Power Generation," *Proceedings of IMECE '03, ASME International Mechanical Engineering Congress & Exposition,* vol. 16-21, p. 42082, 2003.

[7] H. Li, A. Lal, J. Blanchard, and D. Henderson, "Self-reciprocating radioisotope-powered cantilever," *Journal of Applied Physics,* vol. 92, pp. 1122-1127, 2002.

[8] R. Amirtharajah and A. P. Chandrakasan, "Self-powered signal processing using vibration-based power generation," *Solid-State Circuits, IEEE Journal of,* vol. 33, pp. 687-695, 1998.

[9] S. Roundy., P. Wright., and J. Rabaey., *Energy Scavenging for Wireless Sensor Networks with Special Focus on Vibrations*: Kliwer Academic Press, 2003.

[10] S. O. Kasap, *Optoelectronics and Photonics: Principles amd Practices*, 2001.

[11] S. Lee, "Development of High-efficiency Silicon Solar Cells for Commercialization," *Journal of Korean Physical Society,* vol. 39, pp. 369-373,

2001.

[12] T. W. Silk and A. J. Schofield, "Thermoelectric Effects in Anisotropic Systems: Measurement and Applications," *Condensed Matter - Materials Science,* pp. 1-27, 2008.

[13] G. Savelli., M. P. J. Bablet., C. Salvi., and J. M. Fournier., "Energy conversion using new thermoelectric generator," *DTIP of MEMS & MOEMS,* 2006.

[14] S. Roundy, D. Steingart, L. Frechette, P. Wright, and J. Rabaey, "Power Sources for Wireless Sensor Networks," in *Wireless Sensor Networks*, 2004, pp. 1-17.

[15] T. Starner, "Human-powered Wearable Computing," *IBM Systems Journal,* vol. 35, pp. 618-629, 1996.

[16] N. Shenck and J. Paradiso, "Energy Scavenging with Shoe-mounted Piezoelectrics," *IEEE Micro,* vol. 21, pp. 30-42, 2001.

[17] J. Rabaey, M. Ammer, J. Silva, D. P. Jr, and S. Roundy, "PicoRadio Supports Ad Hoc Ultra-low Power Wireless Networking," *IEEE Computer,* vol. 33, pp. 42-48, 2000.

[18] H. Jonathan, "Starting to explore wind power," *Physics Education,* vol. 43, p. 572, 2008.

[19] S. Roundy, E. S. Leland, J. Baker, E. Carleton, E. Reilly, E. Lai, B. Otis, J. M. Rabaey, P. K. Wright, and V. Sundararajan, "Improving power output for vibration-based energy scavengers," *Pervasive Computing, IEEE,* vol. 4, pp. 28-36, 2005.

[20] G. K. Ottman, H. F. Hofmann, A. C. Bhatt, and G. A. Lesieutre, "Adaptive piezoelectric energy harvesting circuit for wireless remote power supply," *Power Electronics, IEEE Transactions on,* vol. 17, pp. 669-676, 2002.

[21] M. Ferrari, V. Ferrari, D. Marioli, and A. Taroni, "Modeling, Fabrication and Performance Measurements of a Piezoelectric Energy Converter for Power Harvesting in Autonomous Microsystems," *Instrumentation and Measurement,*

IEEE Transactions on, vol. 55, pp. 2096-2101, 2006.

[22] E. Torres and G. Rincón-Mora, "Long-Lasting, Self-Sustaining, and Energy-Harvesting System-in-Package (SIP) Wireless Micro-Sensor Solution," *Proceedings of International Conference on Energy, Environment and Disasters (INCEED 2005),* pp. 1-33, 2005.

[23] X. Cao, W. Chiang, Y. King, and Y. K. Lee, "Electromagnetic Energy Harvesting Circuit with Feedforward and Feedback DC-DC PWM Boost Converter for Vibration Power Generator System," *Power Electronics, IEEE Transactions on,* vol. 22, pp. 679-685, 2007.

[24] T. Sterken, K. Baert, R. Puers, G. Borghs, and R. Mertens, "A new power MEMS component with variable capacitance," *in Proc. Pan Pacific Microelectronics Symp,* pp. 27-34, 2003.

[25] B. C. Yen and J. H. Lang, "A variable-capacitance vibration-to-electric energy harvester," *Circuits and Systems I: Regular Papers, IEEE Transactions on,* vol. 53, pp. 288-295, 2006.

[26] S. Meninger, J. O. Mur-Miranda, R. Amirtharajah, A. Chandrakasan, and J. H. Lang, "Vibration-to-electric energy conversion," *Very Large Scale Integration (VLSI) Systems, IEEE Transactions on,* vol. 9, pp. 64-76, 2001.

[27] F.G. Tseng and Y. Chiu, "Capacitive vibration-to-electricity energy with integrated mechanical switches," *Power MEMS 2007,* pp. 121-124, 2007.

[28] S. Roundy, P. Wright, and K. Pister, "Micro-Electrostatic Vibration-to-Electricity Converters," *Proceedings of IMECE ASME International Mechanical Engineering Congress& Exposition,* pp. 17-22, 2002.

[29] Y. Chiu, C. T. Kuo, and Y. S. Chu, "MEMS design and fabrication of an electrostatic vibration-to-electricity energy converter," *Microsystem Technologies,* vol. 13, pp. 1663-1669, 2007.

[30] F. Peano and T. Tambosso, "Design and optimization of a MEMS electret-based capacitive energy scavenger," *Microelectromechanical Systems,*

Journal of, vol. 14, pp. 429-435, 2005.

[31] P. D. Mitcheson, T. C. Green, E. M. Yeatman, and A. S. Holmes, "Architectures for vibration-driven micropower generators," *Microelectromechanical Systems, Journal of,* vol. 13, pp. 429-440, 2004.

[32] J. Starr, "Squeeze-film Damping In Solid-state Accelerometers," *IEEE Solid-State Sensor and Actuator Workshop. Digest of Technical Papers,* pp. 44-47, 1990.

[33] R. Legtenberg, A. W. Groeneveld, and M. Elwenspoek, "Comb-drive Actuators for Large Displacements," *Journal of Micromechanics & Microengineering,* vol. 6, pp. 320-329, 1996.

[34] M. Judy, "Micromechanisms Using Sidewall Beams." vol. PhD USA: University of California, Berkeley, 1994.

[35] M. Miyazaki, H. Tanaka, G. Ono, T. Nagano, N. Ohkubo, T. Kawahara, and K. Yano, "Electric-energy generation using variable-capacitive resonator for power-free LSI: efficiency analysis and fundamental experiment," in *Low Power Electronics and Design, 2003. ISLPED '03. Proceedings of the 2003 International Symposium on*, 2003, pp. 193-198.

[36] J. B. Bates, N. J. Dudney, B. Neudecker, A. Ueda, and C. D. Evans, "Thin-film lithium and lithium-ion batteries," *Solid State Ionics,* vol. 135, pp. 33-45, 2000.

[37] J. Li, Q. X. Zhang, A. Q. Liu, W. L. Goh, and J. Ahn, "Technique for preventing stiction and notching effect on silicon-on-insulator microstructure," *Journal of Vacuum Science & Technology B: Microelectronics and Nanometer Structures,* vol. 21, pp. 2530-2539, 2003.

[38] J. Karttunen, S. Franssila, and J. Kiihamaki, "Loading Effects in Deep Silicon Etching," *Proceedings of SPIE 2000 International Society of Optical Engineering,* vol. 4174, pp. 90-97, 2000.

[39] P. S. Nam, L. M. Ferreira, T. Y. Lee, and K. N. Tu, "Study of grass formation in GaAs backside via etching using inductively coupled plasma system,"

Journal of Vacuum Science & Technology B: Microelectronics and Nanometer Structures, vol. 18, pp. 2780-2784, 2000.

[40] M. Orfert and K. Richter, "Plasma enhanced chemical vapor deposition of SiN-films for passivation of three-dimensional substrates," *Surface and Coatings Technology,* vol. 116-119, pp. 622-628, 1999.

[41] G. T. A. Kovacs, *Micromachined Transducers Sourcebook*: McGraw-Hill Companies, 2000.

[42] M. C. Jo, S. K. Park, and S. J. Park, "A study on resistance of PECVD silicon nitride thin film to thermal stress-induced cracking," *Applied Surface Science,* vol. 140, pp. 12-18, 1999.

[43] F. E. H. Tay, X. Jun, Y. C. Liang, V. J. Logeeswaran, and Y. Yufeng, "The effects of non-parallel plates in a differential capacitive microaccelerometer " *Journal of Micromechanics and Microengineering* vol. 4, pp. 283-293, 1999.